

Covalent Carbon Nanodot-Azobenzene Hybrid Photoswitches: The Role of *Meta/Para* Connectivity and sp^3 Spacer in Photophysical Properties

Paul P. Debes,^{a,b,†} Dominic Schatz,^{a,c,†} Yagmur Aydogan-Sun,^d Juan Pablo Martínez,^e Michal Langer,^f Janis Hessling,^g Jaime Gallego,^{a,b} Enzo Menna,^h Bernd M. Smarsly,^{a,b} Monika Schönhoff,^g Silvio Osella,^e Josef Wachtveitl,^d Hermann A. Wegner,^{*,a,c} Teresa Gatti^{*,a,b,i}

^a Center for Materials Research, Justus Liebig University, Heinrich-Buff-Ring 16, 35392, Giessen (Germany).

^b Institute of Physical Chemistry, Justus Liebig University, Heinrich-Buff-Ring 17, 35392, Giessen (Germany).

^c Institute of Organic Chemistry, Justus Liebig University, Heinrich-Buff-Ring 17, 35392, Giessen (Germany). E-mail: Hermann.A.Wegner@org.chemie.uni-giessen.de

^d Institute of Physical and Theoretical Chemistry, Goethe University, Max von Laue-Strasse 7, 60438, Frankfurt (Germany).

^e Chemical and Biological Systems Simulation Lab, Centre of New Technologies, University of Warsaw, 2c Banacha Street, 02-097, Warszawa (Poland).

^f IT4Innovations, VSB – Technical University of Ostrava, 17.listopadu 2172/15, 70800, Ostrava-Poruba (Czech Republic)

^g Institute of Physical Chemistry, University of Münster, Corrensstrasse 28/30, 48149, Münster (Germany).

^h Department of Chemical Sciences, University of Padova and INSTM UdR Padova, via Marzolo 1, 35131, Padova (Italy)

ⁱ Department of Applied Science and Technology, Politecnico di Torino, C.so Duca degli Abruzzi 24, 10129, Torino (Italy). E-mail: teresa.gatti@polito.it

† These authors contributed equally.

Table of Contents

Experimental	3
Materials and Methods	3
CND Synthesis.....	5
Azobenzene Synthesis	5
Amide Coupling of CNDs with Azobenzene Derivatives	8
Computational Details	8
Diffusion Measurement	11
Atomic Force Microscopy	18
Thermogravimetric Analysis	22
Photoluminescence Quantum Yield	23
Absorption Coefficients and Degree of Azo Functionalization	28
Computational Analysis	31
Model of the CND	31
The Truncated Model of the CND.....	34
CNDs Functionalized with Azobenzene.....	37
Isomer <i>Cis</i> of Azobenzene and Corresponding CND hybrids.....	41
Isomer <i>Trans</i> of Azobenzene and Corresponding CND hybrids.....	44
<i>Meta</i> -Glycine-Azobenzene and Corresponding CND hybrids.....	48
Excitation-emission maps.....	53
Excitation Spectra.....	54
Time-Correlated Single Photon Counting (TCSPC)	55
Determination of Transfer Rates and Emission Quenching Efficiencies	56
Photo-Switching	59
Fatigue Resistance	60
Kinetic Measurements	63
NMR Spectra.....	71
CND.....	71
3-(Phenylazo)benzoic acid (<i>m</i> -Azo)	72

4-(Phenylazo)benzoic acid (<i>p</i> -Azo)	73
<i>N</i> -[3-(phenylazo)benzoyl]glycine methyl ester	74
<i>N</i> -[3-(phenylazo)benzoyl]glycine (<i>m</i> -Gly-Azo)	76
CND- <i>m</i> -Azo	78
CND- <i>p</i> -Azo	79
CND- <i>m</i> -Gly-Azo	80
References	81

Experimental

Materials and Methods

Citric acid (CA, $\geq 99.5\%$), 3-([(ethyylimino)methylidene]amino)-*N,N*-dimethylpropan-1-amine hydrochloride (EDC, $\geq 99\%$), and ethylenediamine (EDA, $\geq 99.5\%$) were purchased from Carl-Roth. *N*-hydroxysuccinimide (NHS, $\geq 99\%$) were purchased from Sigma-Aldrich. Deuterated dimethyl sulfoxide (DMSO- d_6 , 99.8%) was purchased from Deutero. Anhydrous *N,N*-dimethylformamide (DMF, 99.8%, AcroSeal) was purchased from Thermo Scientific. Dimethylsulfoxide (DMSO, 99.5%) was purchased from Gruessing. Solvents for UV-Vis and PL spectroscopy was purchased from Merck (Uvasol® quality). Ultrapure water was obtained with the Milli-Q Direct Water Purification System. Unless otherwise stated, the reagents were used without further purification. The MW-assisted reactions were performed in a Silvia homeline set-up. The purification of CNDs was performed with Spectra/Por Biotech-Grade Cellulose Ester (CE) dialysis tubing with a molecular weight cut-off (MWCO) of 500 Da–1000 Da. Sephadex® G-10 and LH-20 gel filtration media were used for size-exclusion chromatography. NMR-spectra were recorded with a Bruker Avance II 400 MHz, and Bruker Avance III 400 MHz HD. Diffusion measurements were performed using an AVANCE III HD 400 MHz NMR spectrometer equipped with a gradient probe head (Bruker “Diff50”) with a selective ^1H insert, providing a magnetic field

gradient strength of up to 28 T m^{-1} . The samples were measured at $25 \text{ }^{\circ}\text{C}$. To calibrate the temperature a PT 100 thermocouple inserted in an NMR tube, filled with oil, was used. DOSY spectra were acquired by a stimulated echo sequence, as detailed in SI. UV-Vis measurements were carried out with a SPECORD® 200 PLUS spectrophotometer equipped with two automatic eight-fold cell changers and a Peltier element thermostat system ($0.1 \text{ }^{\circ}\text{C}$ accuracy) by Analytik Jena. The system was operated with the ASpect UV software by Analytik Jena. Fluorescence measurements were conducted with a Jasco FP-8300 Fluorescence Spectrometer. The sample solutions were measured in QS High Precision Cells made of Quartz Suprasil® with a light path of 10 mm by Hellma Analytics. Experiments were carried out in concentrations of 1-14 mg L^{-1} . Stock solutions (1 mg mL^{-1}) were prepared from freshly purified samples, and then diluted prior to every UV/Vis and PL experiment. The absorption spectra of the respective azo were obtained using $5 \text{ } \mu\text{mol L}^{-1}$ solutions in DMSO at $25 \text{ }^{\circ}\text{C}$. **CND + *m*-Azo** (mix): $5 \text{ mg L}^{-1} + 0.83 \text{ } \mu\text{mol L}^{-1}$; **CND + *p*-Azo** (mix) and **CND + *m*-Gly-Azo** (mix): $5 \text{ mg L}^{-1} + 1.79 \text{ } \mu\text{mol L}^{-1}$ in DMSO at $25 \text{ }^{\circ}\text{C}$. Irradiation of UV/Vis samples was conducted in an in-house built box using LEDs by Lumitronix or Nichia purchased from leds.de, or by mounted LEDs from Thorlabs. AFM was performed with the AIST-NT SmartSPM 1000 under ambient conditions in AC mode. Thermogravimetric measurements were carried out on a TGA Q5000IR (TA instruments, New Castle, DE, USA). The analyses were performed using a $100 \text{ } \mu\text{L}$ Platinum-HT TAG pan. In order to remove adsorbed moisture, each sample was subjected to a sequence of isotherms under N_2 (at $60 \text{ }^{\circ}\text{C}$ for 10 minutes, then at $80 \text{ }^{\circ}\text{C}$ for 3 minutes and then at $100 \text{ }^{\circ}\text{C}$ for 2 minutes), immediately before the measurement ramp ($10 \text{ }^{\circ}\text{C min}^{-1}$ from $100 \text{ }^{\circ}\text{C}$ to $900 \text{ }^{\circ}\text{C}$) under N_2 atmosphere.

CND Synthesis

For the sake of clarity, the details of the already reported and slightly modified method reported by Pham et al.¹ are given here. CA (1.44 g, 7.50 mmol, 1.00 eq) was dissolved in 5 mL Milli-Q water and was stirred until the substrate was completely dissolved. EDA (0.50 mL, 7.5 mmol, 1.0 eq) was added and the mixture was stirred for 20 min. The reaction mixture was heated in a domestic MW oven for 5 min at 400 W (50% power). The obtained brown resin was dispersed in 10 mL Milli-Q water and the brown dispersion was filtered over a 0.2 μ m PTFE syringe filter. The filtered dispersion of the CNDs were filled up to a volume of 10 mL and dialyzed in a 0.5 kDa – 1 kDa dialysis membrane against Milli-Q water for 48 h, with water changed every 2 h during the day. The obtained brown dispersion was lyophilized and an orange/ brown solid was obtained. ¹H-NMR of the CND species showed broad signals to ensure the presence of CNDs (**Figure S50**).²

Azobenzene Synthesis

3-(Phenylazo)benzoic acid (*m*-Azo):

3-Aminobenzoic acid (2.77 g, 20.0 mmol, 1.00 eq) and nitrosobenzene (2.79 g, 26.0 mmol, 1.30 eq) were stirred in degassed AcOH (40 mL) at rt overnight. The formed suspension was added to water (600 mL), the solid was filtered off and thoroughly washed with water. After drying, the crude compound was recrystallized from toluene (approx. 50 mL) to yield the product as an orange/golden solid.

Yield: 2.17 g, 48%.

¹H-NMR (400 MHz, DMSO-d₆) δ = 13.33 (s, 1H), 8.38 (t, J = 1.8 Hz, 1H), 8.19 – 8.09 (m, 2H), 7.94 (dd, J = 7.8, 1.9 Hz, 2H), 7.74 (t, J = 7.8 Hz, 1H), 7.67 – 7.57 (m, 3H) ppm.

Analytical data corresponded to the literature.³

4-(Phenylazo)benzoic acid (*p*-Azo):

4-Aminobenzoic acid (277 mg, 2.00 mmol, 1.00 eq) and nitrosobenzene (279 mg, 2.60 mmol, 1.30 eq) were stirred in degassed AcOH (5 mL) at rt overnight. The solvent was removed under reduced pressure and the product was purified by column chromatography (80 g SiO₂, Cyclohexane:EtOAc = 10:1 → 4:1) to yield the product as an orange, crystalline solid.

Yield: 110 mg, 24%.

¹H-NMR (400 MHz, DMSO-d₆) δ = 13.25 (s, 1H), 8.15 (d, *J* = 8.3 Hz, 2H), 8.04 – 7.86 (m, 4H), 7.63 (dd, *J* = 5.2, 2.1 Hz, 3H) ppm.

Analytical data corresponded to the literature.³

Glycine methyl ester:

Glycine (1.88 g, 25.0 mmol, 1.00 eq) was suspended in MeOH (250 mL). The suspension was cooled to 0 °C and SOCl₂ (3.00 mL, 41.1 mmol, 1.00 eq) was added dropwise. The suspension was stirred at rt overnight. Then, the clear solution was concentrated into dryness under reduced pressure to yield the product as a white, crystalline solid. It was used as yielded for next steps.

3-(Phenylazo)benzoyl chloride:

3-(Phenylazo)benzoic acid (226 mg, 1.00 mmol, 1.00 eq) was suspended in CH₂Cl₂ (dry, 4 mL) with one drop DMF (dry). Oxalyl chloride (103 mL, 1.20 mmol, 1.20 eq) was added dropwise. Immediately formation of gas was observed and the orange suspension turned to a red solution. Stirring continued at rt for 2 h. Solvent was removed under reduced pressure and dried thoroughly under high vacuum to yield the product as a dark red solid. It was used as yielded for next steps.

***N*-[3-(Phenylazo)benzoyl]glycine methyl ester:**

3-(Phenylazo)benzoyl chloride (245 mg, 1.00 mmol, 1.00 eq) and glycine methyl ester (126 mg, 1.00 mmol, 1.00 eq) were suspended in CH₂Cl₂ (dry, 3 mL). DIPEA (400 μ L, 2.32 mmol, 2.32 eq)

was added dropwise and the reaction mixture was stirred at rt overnight. SiO₂ (2 g) was added and the solvent was removed under reduced pressure. Crude product was purified by column chromatography (30 g SiO₂, cyclohexane:EtOAc 2:1) to yield the product as an orange, crystalline solid.

Yield: 211 mg, 71%.

¹H-NMR (400 MHz, DMSO-d₆) δ = 9.22 (t, J = 5.8 Hz, 1H), 8.38 (t, J = 1.8 Hz, 1H), 8.11 – 8.04 (m, 2H), 7.96 – 7.91 (m, 2H), 7.74 (t, J = 7.8 Hz, 1 H), 7.68 – 7.57 (m, 3H), 4.06 (d, J = 5.9 Hz, 2H), 3.68 (s, 3H) ppm.

¹³C-NMR (101 MHz, DMSO-d₆): 170.3, 165.9, 151.9, 134.9, 131.9, 130.1, 129.8, 129.6, 125.7, 122.7, 121.0, 51.2, 41.3 ppm.

HRMS (ESI) m/z : [MNa]⁺ calculated: 320.1005, found: 320.1005

***N*-[3-(phenylazo)benzoyl]glycine (*m*-Gly-Azo):**

N-[3-(Phenylazo)benzoyl]glycine methyl ester (211 mg, 710 μ mol, 1.00 eq.) and LiOH (51 mg, 2.13 mmol, 3.00 eq) were stirred in THF (4 mL) and H₂O (16 mL) at rt overnight. The mixture was acidified with 1 M HCl and shortly placed on the rotavap to evaporate some of the THF. The reaction mixture was extracted with CH₂Cl₂ (5x 20 mL). Organic phases were combined and silica (2 g) was added and thoroughly dried under reduced pressure. Crude product was purified by a short silica plug (15 g SiO₂, cyclohexane:EtOAc 1:1) to yield the product as an orange solid.

Yield: 110 mg, 55%.

¹H-NMR (400 MHz, DMSO-d₆) δ = 12.7 (b, 1H), 9.10 (t, J = 5.9 Hz, 1H), 8.38 (t, J = 1.8 Hz, 1H), 8.11 – 8.03 (m, 2H), 7.99 – 7.89 (m, 2H), 7.73 (t, J = 7.8 Hz, 1H), 7.67 – 7.57 (m, 3H), 3.97 (d, J = 5.8 Hz, 2H) ppm.

^{13}C -NMR (101 MHz, DMSO- d_6): 171.2, 165.8, 151.9, 135.2, 131.9, 130.1, 129.7, 129.6, 125.6, 122.7, 121.0, 41.3 ppm.

HRMS (ESI) m/z : [M-H] calculated: 280.0884, found: 282.0884

Amide Coupling of CNDs with Azobenzene Derivatives

Azobenzene (1 eq) was dissolved in 90 mL mmol^{-1} anhydrous DMF. EDC (2 eq) and NHS (2 eq) were added, and the mixture was stirred for 15 min at rt. CNDs (112 mg mmol^{-1}) were added and the reaction mixture was stirred overnight at rt. The solvent was removed under reduced pressure. The obtained crude was packed on a Sephadex G-10 gel column with DMSO as eluent. The obtained brown dispersion was lyophilized and an orange/brown solid was obtained.

Computational Details

A model of the **CND** was initially derived from molecular dynamics simulations (**Figure S20**). In the molecular dynamics (MD) simulations, the ad-hoc model of polymeric CD was first designed by the condensation of citric acid (CA) and ethylenediamine (EDA) molecules, and all the formed chains were capped with a prototypical molecular fluorophore IPCA. The initially stretched polymer (**Figure S17a**) This model was set up with parameters from the Generalized Amber Force Field (GAFF).⁴ RESP partial charges were determined using the Antechamber tool⁵ from the Amber software package⁶ by fitting of the electrostatic potential computed at the HF/6-31G* level in a gaseous state. After this parametrization, the CD was added to the center of a cubic simulation box measuring $8.0 \times 8.0 \times 8.0 \text{ nm}^3$ and solvated with 16804 TIP3P⁷ explicit water molecules. After an initial minimization, a two-step equilibration process was employed. The first step involved heating the system from 10 K to 300 K over 1 ns using a V-rescale⁸ thermostat with

a 0.1 ps time constant. This was followed by a 2 ns equilibration of pressure using the isotropic Berendsen⁹ barostat, keeping the pressure at 1 bar and maintaining the temperature at 300 K with a pressure relaxation time constant of 2 ps. Subsequently, the MD simulations was conducted for 100 ns in the NPT ensemble with a 2 fs time step. The bonds with hydrogens were constrained using the LINCS¹⁰ algorithm. Temperature control was maintained at 300 K via the V-rescale thermostat with a 0.1 ps time constant, while pressure was regulated at 1 bar using the isotropic Parrinello–Rahman barostat¹¹ with a 2 ps relaxation time. Electrostatic interactions were managed using the particle-mesh Ewald (PME)¹² method, applying a real-space cut-off of 1 nm, which was also used for van der Waals interactions. Periodic boundary conditions were applied in all directions. These MD simulations were executed in Gromacs 5.0.¹³

The resulting geometry of the **CND** and subsequent chemical modifications were optimized at the GFN2-xTB level of theory (as implemented in the xtb ver. 6.4.1 software).^{14,15} The analytical linearized Poisson-Boltzmann (ALPB) model was utilized to incorporate solvent effects due to DMSO. For all optimized structures, UV-Vis absorption spectra were calculated via ONIOM (Our own N-layered Integrated molecular Orbital and molecular Mechanics)^{16,17} including time-dependent density-functional-theory (TDDFT) under the linear response formalism. For the high layer (TDDFT level), the long-range hybrid functional ω B97X-D^{18–21} was utilized to calculate 30 singlet-to-singlet transitions. The electronic configuration of the molecular systems was described by the gaussian 6-31G(d) basis set.²² The polarizable continuum model (PCM)^{23–25} was used to account for the effect of DMSO in the electronic transitions. The medium layer was simulated by means of the semi empirical PM6²⁶ method in the ground state. In this context, the reaction field corresponding to DMSO was computed separately in each sub-calculation, using the cavity of the real system in all instances.^{27,28} All ONIOM TDDFT:PM6 calculations were completed using the

quantum-chemistry code Gaussian 16.²⁹ Finally, for the isolated azo compounds, geometry optimizations were confirmed as local minima via analytical-frequency calculations and UV-Vis spectra were calculated at the (TD) (PCM:DMSO)-wB97X-D/6-31G(d) level of theory.

Diffusion Measurement

For ^1H NMR analyses the samples were dissolved in DMSO- d_6 and sealed in NMR tubes with Parafilm. The respective concentrations of the samples were (i) $10 \text{ mg}\cdot\text{mL}^{-1}$ **CND**, (ii) $1 \text{ mg}\cdot\text{mL}^{-1}$ ***m*-Azo**, (iii) $10 \text{ mg}\cdot\text{mL}^{-1}$ of **CND** and $1 \text{ mg}\cdot\text{mL}^{-1}$ of ***m*-Azo** for the physical mixture, and (iv) $11 \text{ mg}\cdot\text{mL}^{-1}$ for the hybrids.

The diffusion measurements were carried out using the stimulated echo experiment with a variation of the gradient pulse strength g . The gradient pulse duration δ was 1 ms and the observation time $\Delta=20$ ms. The resulting echo decays were evaluated by the Stejskal-Tanner equation³²:

$$\frac{I}{I_0} = \exp\left(-\gamma^2 \delta^2 g^2 \left(\Delta - \frac{\delta}{3}\right) \cdot D\right) \quad (1)$$

in which γ denotes the gyromagnetic ratio of the ^1H nucleus.

Due to the polydispersity of the CNDs, a single self-diffusion coefficient cannot describe the echo decay sufficiently. To perform an analysis of the echo decays we therefore followed a method described by Lenocho et al.³³, considering a distribution of diffusion coefficients $P(D)$ with a resulting echo decay of the form:

$$\frac{I}{I_0} = \int_{-\infty}^{\infty} P^*(D) \exp\left(-\gamma^2 \delta^2 g^2 \left(\Delta - \frac{\delta}{3}\right) \cdot D\right) d\ln(D) \quad (2)$$

Here, $P^*(D)$ is a modified distribution with $P^*(D) = D \cdot P(D)$. A commonly used function for $P(D)$ in the case of polymer diffusion³², but also applicable here, is the log-normal distribution:

$$P(D) = \frac{1}{\sqrt{2\pi}\sigma_D D} \exp\left(-\frac{[\ln D - \ln \langle D \rangle]^2}{2\sigma_D^2}\right) \quad (3)$$

In combination with Equation (2), $\langle D \rangle$ corresponds to the value at the maximum of the distribution. Using the Stokes-Einstein Equation (4) the diameter of the respective diffusing

species was estimated from $\langle D \rangle$. The temperature T during the measurement was 298.4 K, and the viscosity of DMSO-d₆³⁴ at 298 K of 2.195 mPa·s was used for the viscosity η .

$$r = \frac{k_B T}{6\pi\eta\langle D \rangle} \quad (4)$$

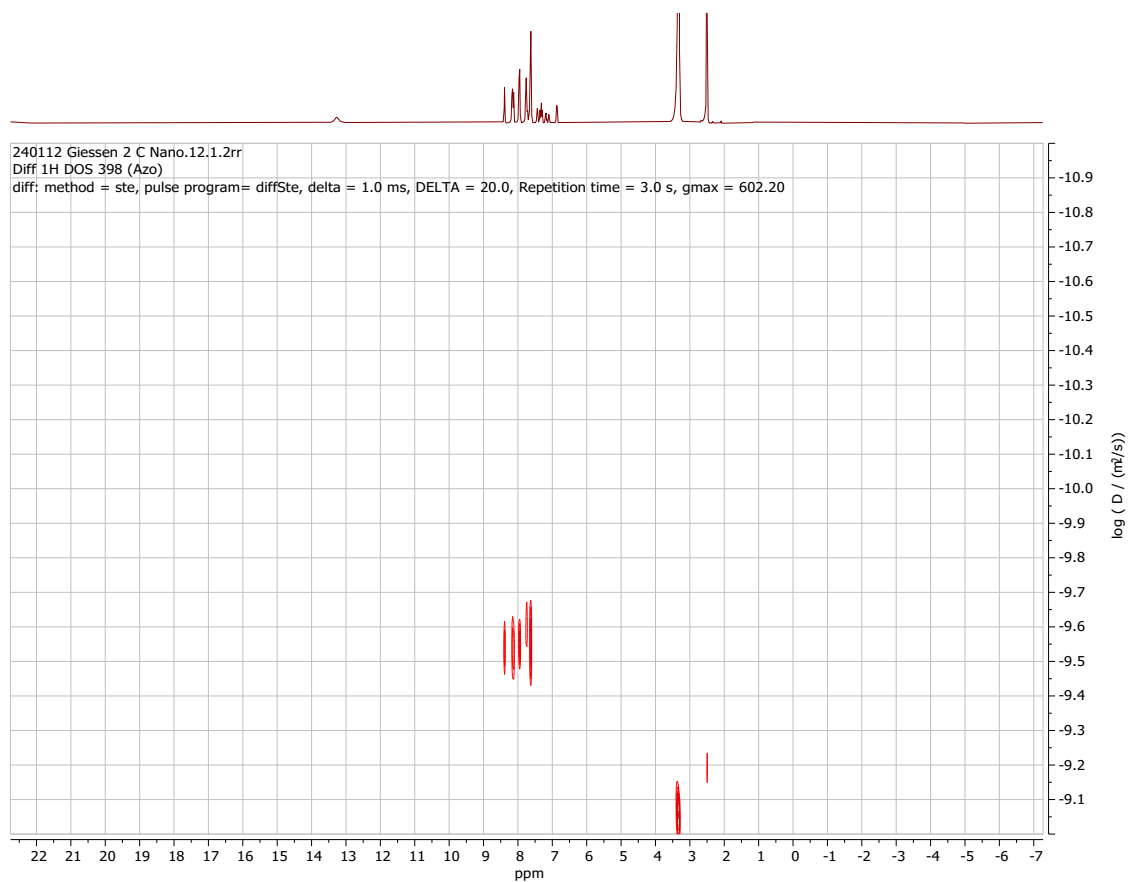


Figure S1. 2D DOSY NMR spectra of *m*-Azo measured in DMSO-d₆.



Figure S2. 2D DOSY NMR spectra of **CND** measured in DMSO-d₆.

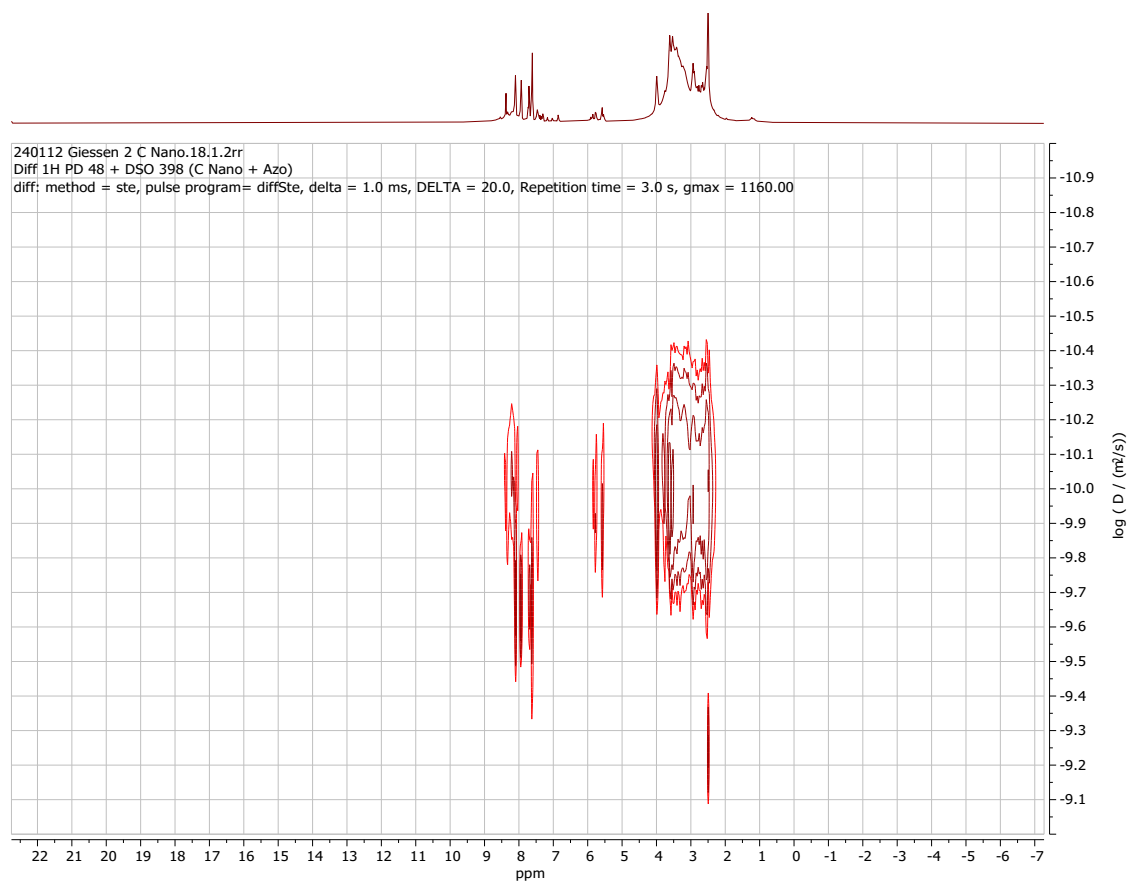


Figure S3. 2D DOSY NMR spectra of a physical mixture of **CND** (10 mg) and ***m*-Azo** (1 mg) measured in DMSO-*d*₆.

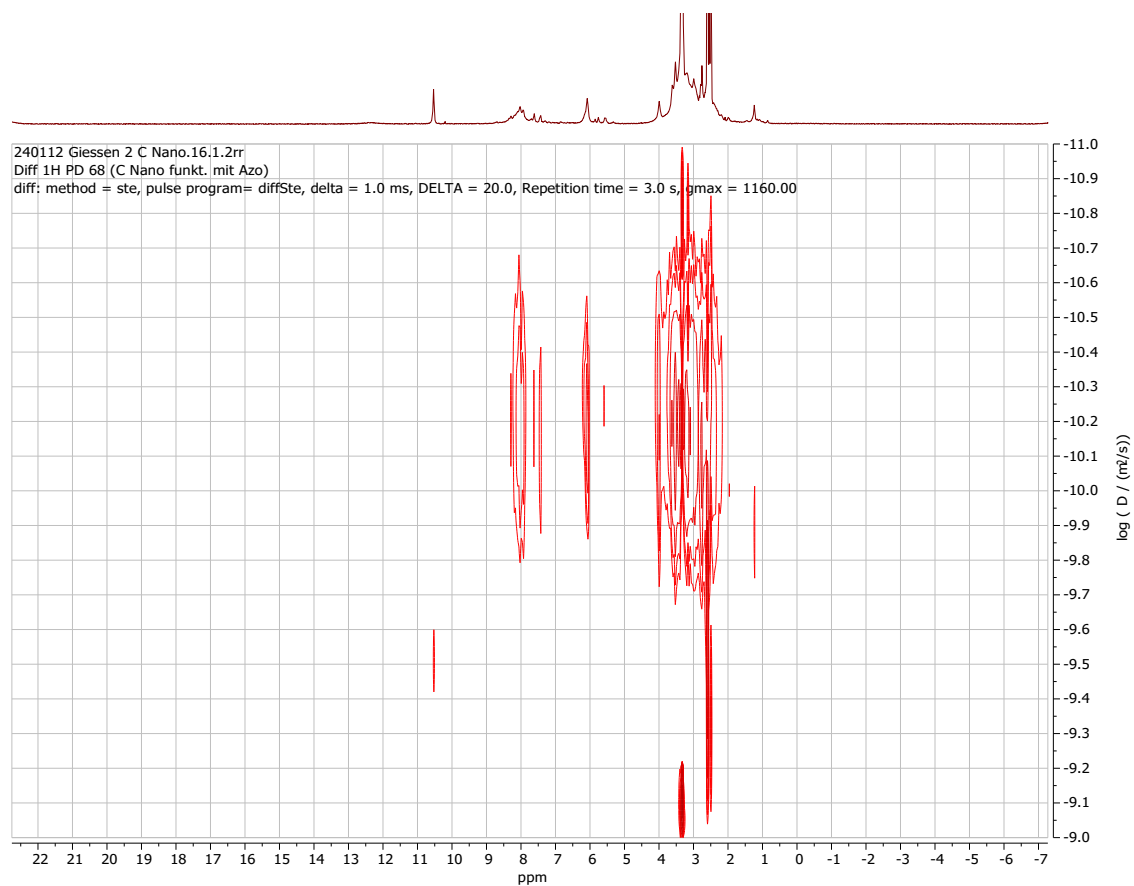


Figure S4. 2D DOSY NMR spectra of **CND-*m*-Azo** CNDs measured in DMSO-d₆.

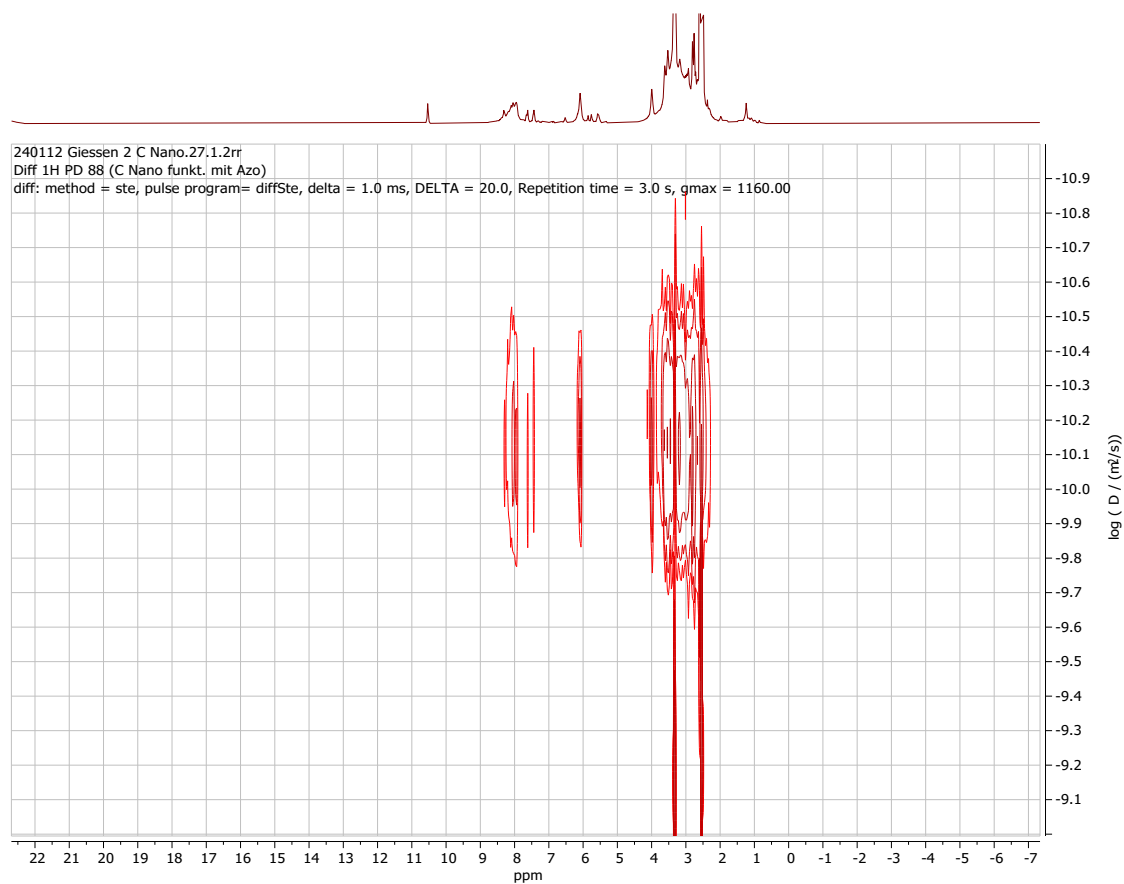


Figure S5. 2D DOSY NMR spectra of **CND-*p*-Azo** CNDs measured in DMSO-d₆.

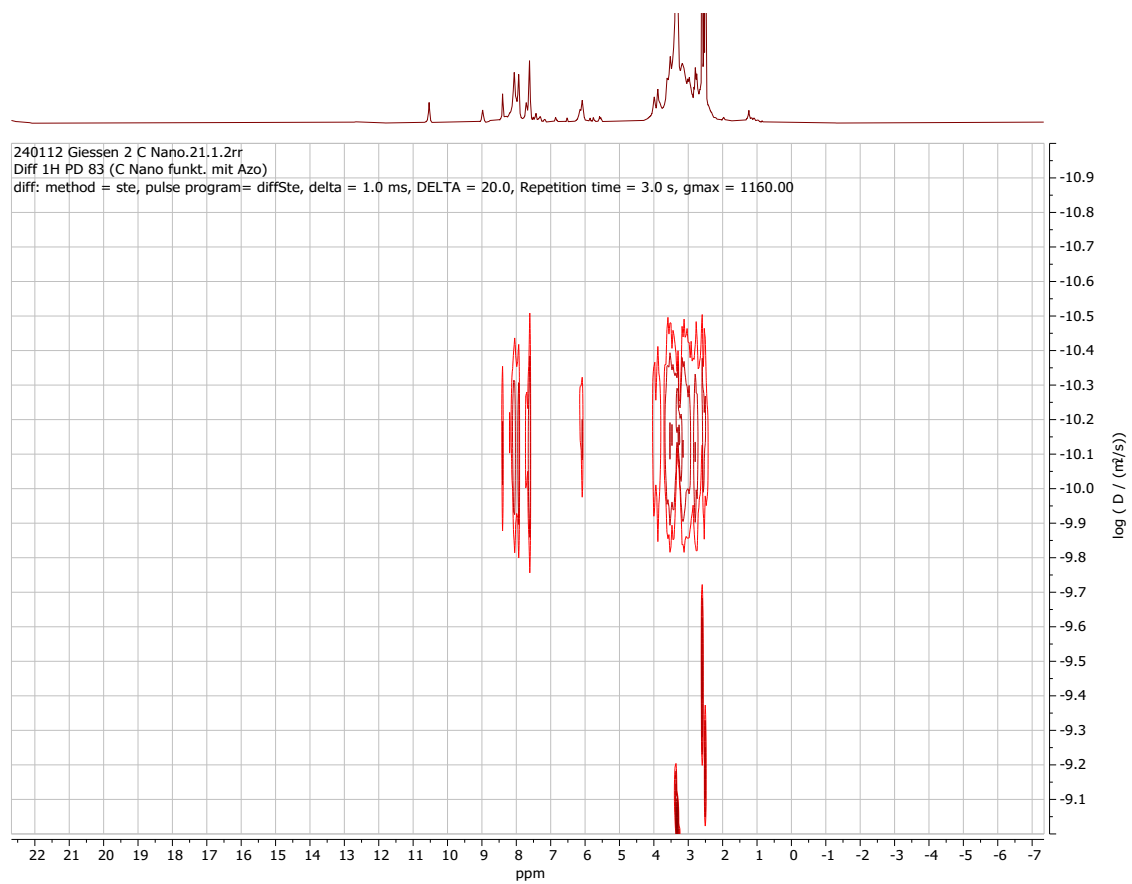


Figure S6. 2D DOSY NMR spectra of **CND-*m*-Gly-Azo** CNDs measured in DMSO-d₆.

Atomic Force Microscopy

0.02 mg·mL⁻¹ dispersions of CND and CND-azo hybrids in DMSO were drop casted on freshly cleaved V1 grade Mica discs (10 mm diameter, 0.15–0.21 mm thickness). After keeping the prepared samples overnight under reduced pressure, they were measured in AFM tapping mode with a SSS-FMR probe (75 kHz, 2.8 N·m⁻¹). The obtained images were analyzed with Gwyddion 2.62³⁰ and the size of ~70 nanoparticles was measured for a size histogram.

AFM directly images the surface of particles, capturing their actual physical size, shape, and surface structure. However, when particle agglomerates are present and appear as single larger particles in AFM measurements, there can be a discrepancy in the measured size.³¹ This aggregation can potentially be observed in **Figure S11C-D**, as CNDs are known to have a tendency to aggregate. However, it can be said that AFM is limited locally to a few micrometers, and thus the concentrations can vary locally, which can certainly influence the formation of agglomerates on the mica surface.

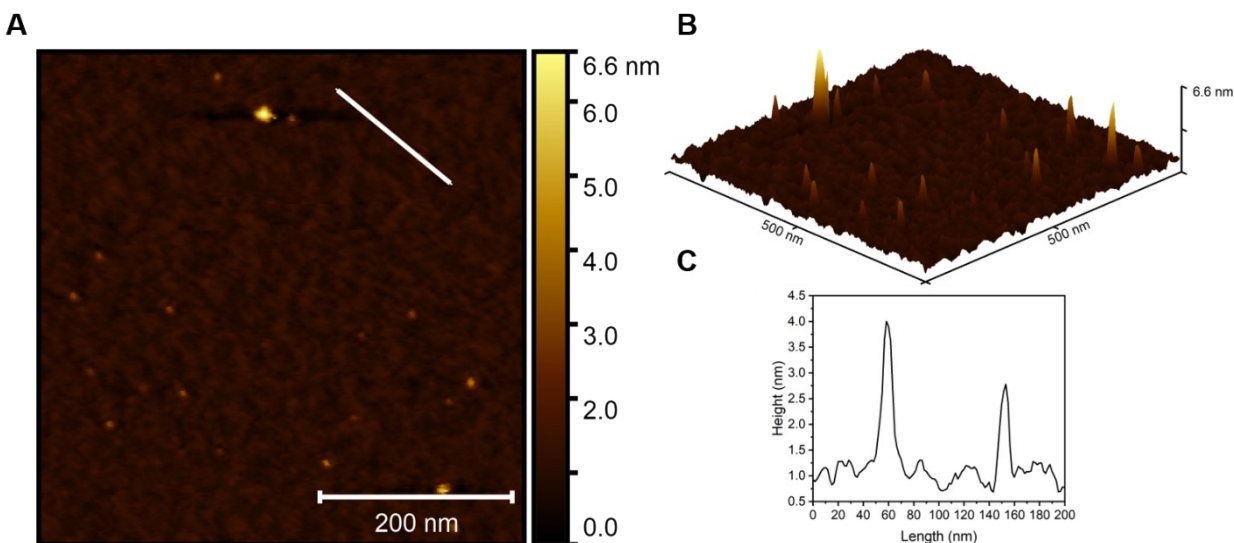


Figure S7. (A) 2D AFM image (500×500 nm) of CND. (B) 3D AFM image (500×500 nm) of CND and height profile along the white line in the 2D image.

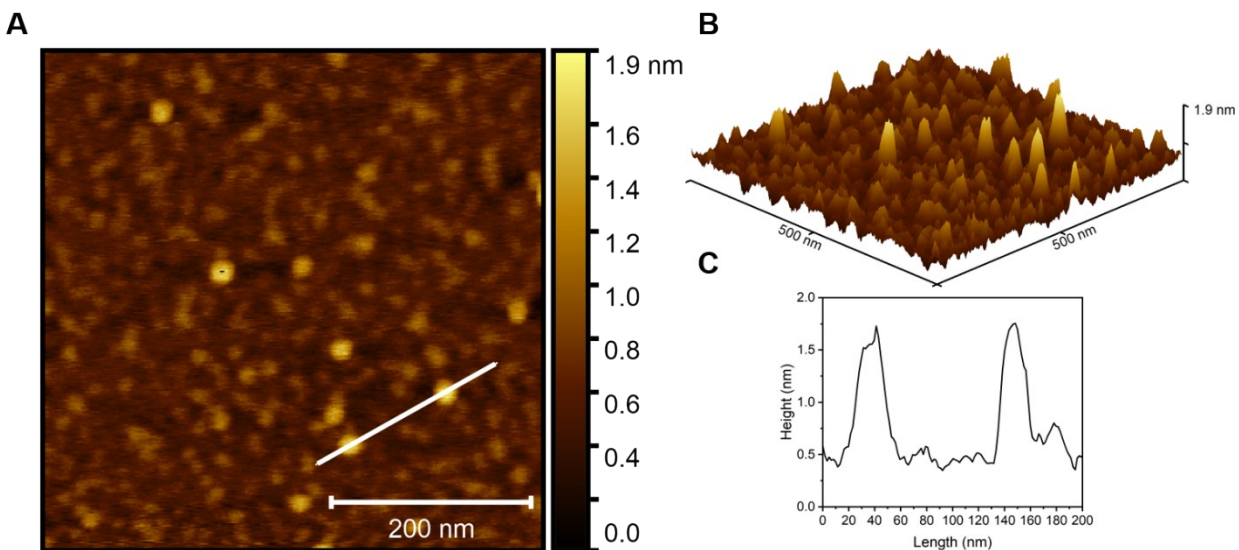


Figure S8. (A) 2D AFM image (500×500 nm) of **CND-*m*-Azo** CNDs. (B) 3D AFM image (500×500 nm) of **CND-*m*-Azo** CNDs. (C) Height profile along the white line in the 2D image.

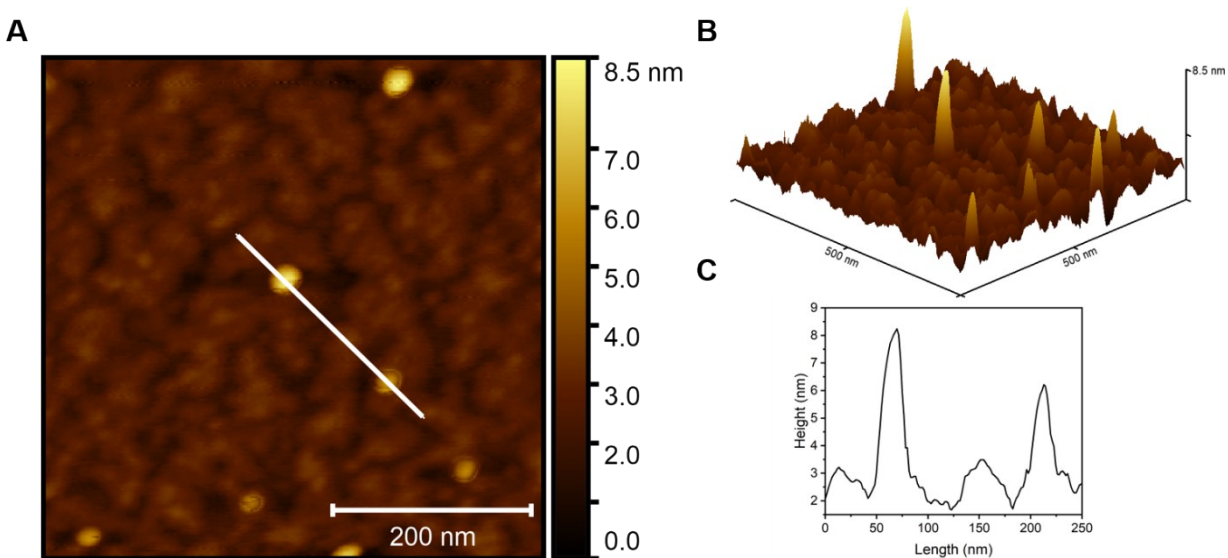


Figure S9. (A) 2D AFM image (500×500 nm) of **CND-*p*-Azo** CNDs. (B) 3D AFM image (500×500 nm) of **CND-*p*-Azo** CNDs. (C) Height profile along the white line in the 2D image.

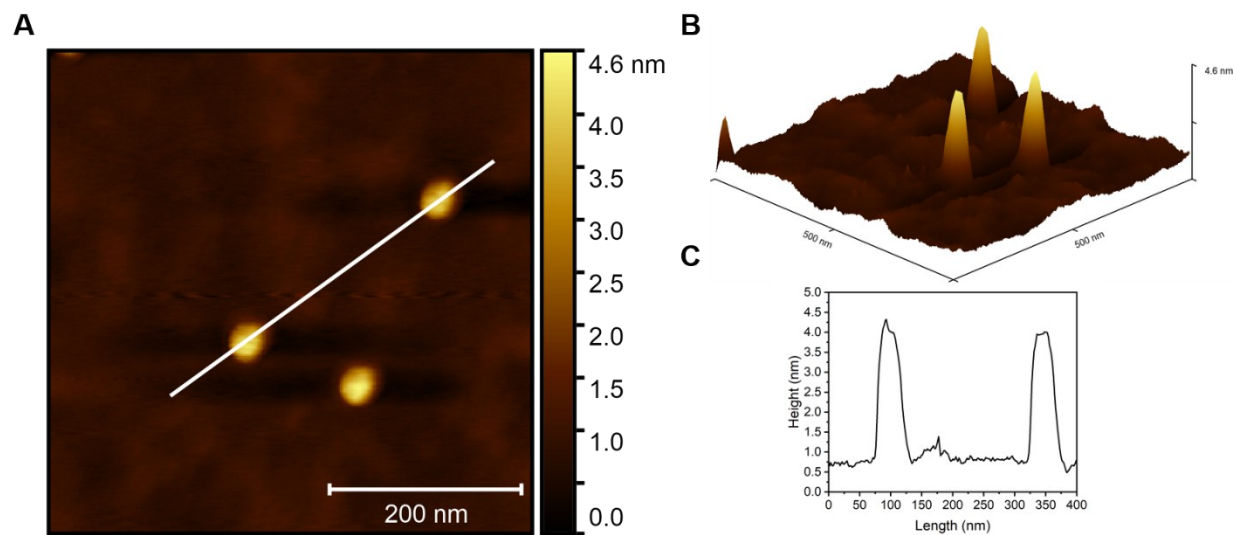


Figure S10. (A) 2D AFM image (500×500 nm) of CND-*m*-Gly-Azo CNDs. (B) 3D AFM image (500×500 nm) of CND-*m*-Gly-Azo CNDs. (C) Height profile along the white line in the 2D image.

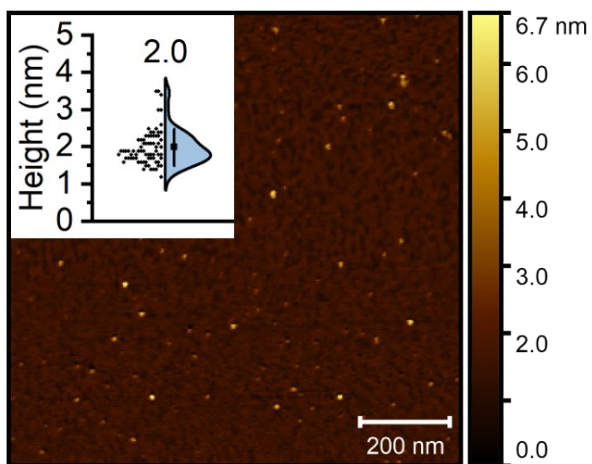
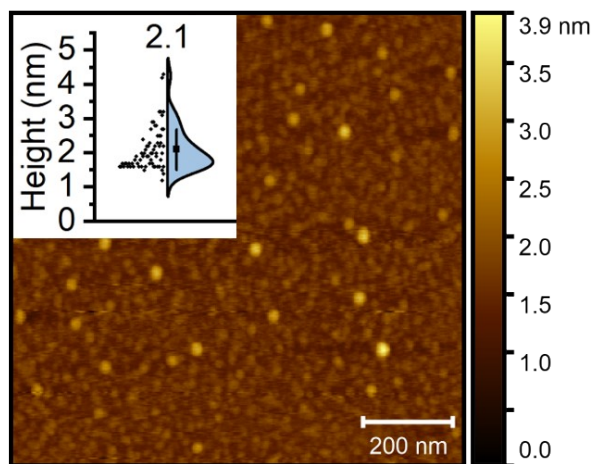
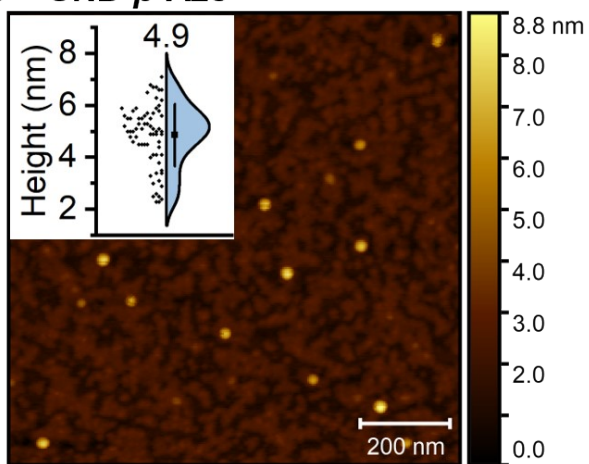
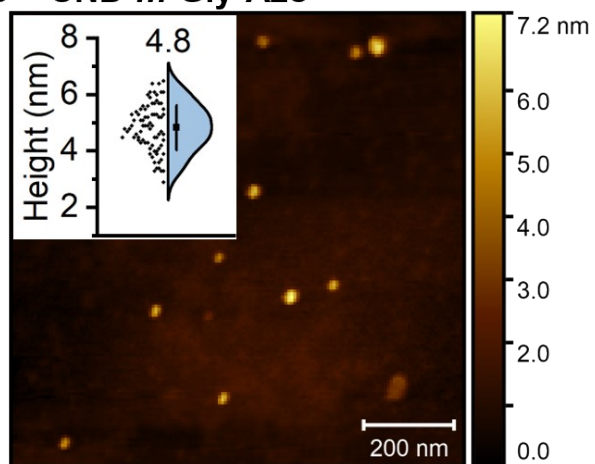
A – CND**B – CND-*m*-Azo****C – CND-*p*-Azo****D – CND-*m*-Gly-Azo**

Figure S11. $1\ \mu\text{m} \times 1\ \mu\text{m}$ AFM images of (A) CND, (B) CND-*m*-Azo (C) CND-*p*-Azo, and (D) CND-*m*-Gly-Azo on a mica substrate. The insets in each figure show the height distribution for each sample, with the mean height and the standard deviation obtained from ~ 70 CNDs.

Thermogravimetric Analysis

Thermogravimetric analysis (TGA) reveals a greater weight loss between 100 °C and 300 °C for the **CND-*p*-Azo** and the **CND-*m*-Gly-Azo** in comparison to the **CND-*m*-Azo** (see **Figure S12**). As previously shown for azo compounds, they decompose within a comparable temperature range³⁵ as the pristine **CND**. The TGA curves of the hybrids thus exhibit a greater mass loss than the pure **CND**, indicating functionalization. However, the simultaneous pyrolysis of the two components and the substantial alteration of the **CND** morphology precludes the possibility of making a precise statement regarding the degree of functionalization by TGA.

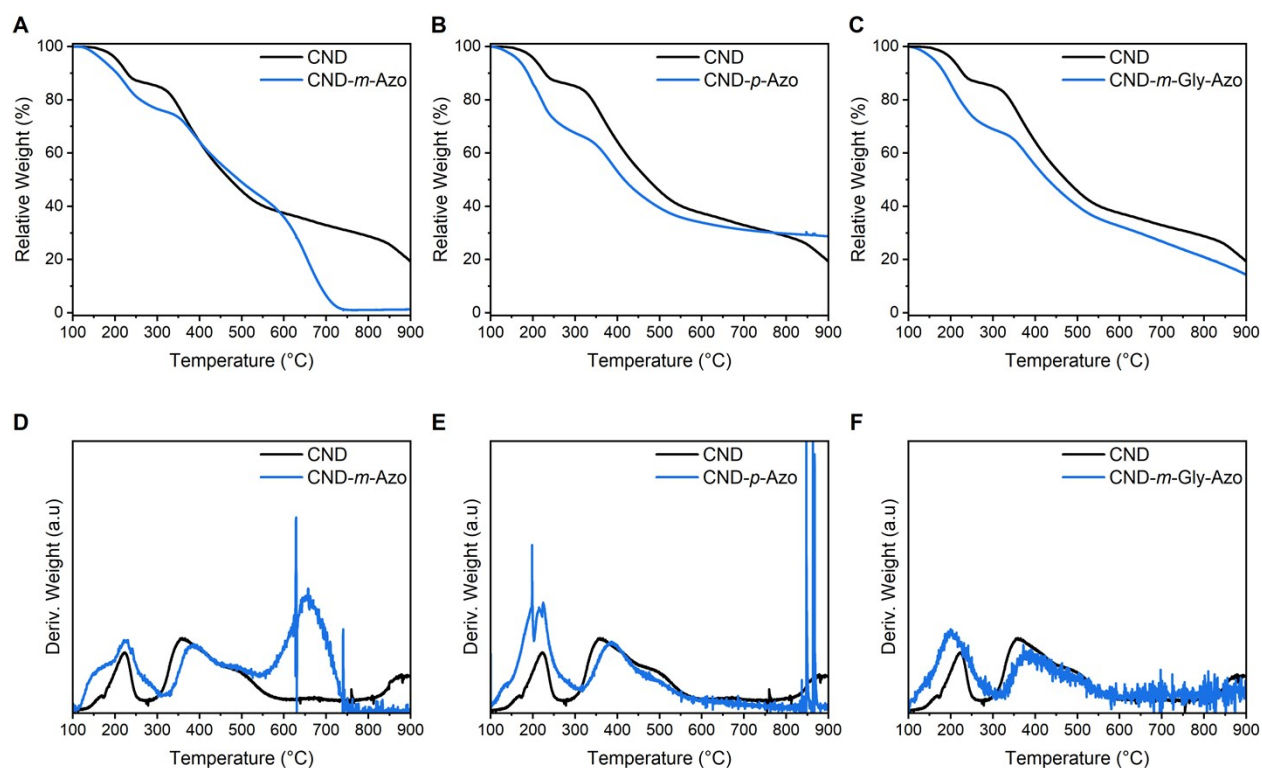


Figure S12. TGA analysis of the CNDs measured in nitrogen (A) **CND** in comparison to **CND-*m*-Azo** (The loss of weight that begins at 600 °C is most likely due to a residual amount of oxygen contamination.) (B) **CND** in comparison to **CND-*p*-Azo** (C) **CND** in comparison to **CND-*m*-Gly-Azo** (D) Derived weight loss of **CND-*m*-Azo** in comparison to **CND**. (E) Derived weight loss of

CND-*p*-Azo in comparison to **CND**. (F) Derived weight loss of **CND-*m*-Gly-Azo** in comparison to **CND**. In all cases, the first significant weight loss was observed between 100 °C and 300 °C. Furthermore, all functionalized CNDs showed higher weight loss in this range. Decomposition started at around 350 °C.

Photoluminescence Quantum Yield

The relative PL quantum yield method with quinine sulfate (QS) as a reference compound was used.³⁶ For five different concentrations of each sample and the reference sample, the UV-Vis absorbance and PL were measured. The maximum values of each absorbance measurement with the respective integrated PL intensity are plotted against each other. From the obtained slopes and the following equation one can calculate the PL quantum yield.

$$\Phi_S = \frac{m_S}{m_R} \cdot \frac{n_S^2}{n_R^2} \cdot \Phi_R \cdot 100$$

Φ_S = quantum yield of the sample [%]

Φ_R = quantum yield of the reference compound (QS = 0.51)

m_S = slope from plotted absorbance against integrated intensity of the sample

m_R = slope from plotted absorbance against integrated intensity of the reference compound

n_S = 1.4785 refractive index of sample solvent (DMSO)

n_R = 1.33415 refractive index of reference solvent (0.1 M H₂SO₄)

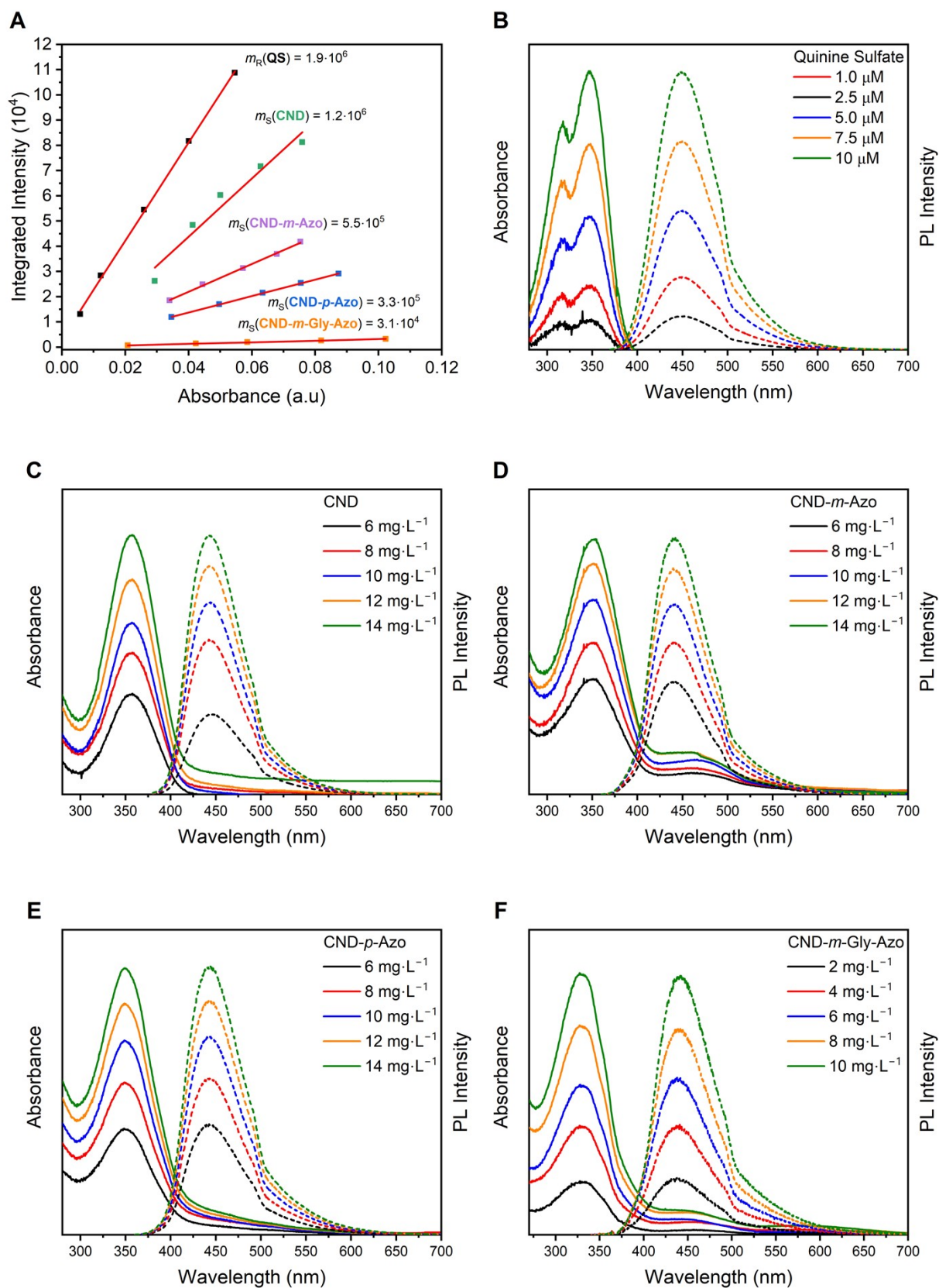


Figure S13. (A) Absorbance maxima plotted against the integrated PL intensity of the five different concentrations and the respective slopes derived from a linear fit. (B) UV-Vis absorbance (solid lines) and PL intensity (dashed lines, $\lambda_{\text{Exc}} = 350 \text{ nm}$) of five different concentrated quinine sulfate (QS) solutions. (C) UV-Vis absorbance (solid lines) and PL intensity (dashed lines, $\lambda_{\text{Exc}} = 360 \text{ nm}$) of five different concentrated **CND** dispersions. (D) UV-Vis absorbance (solid lines) and PL intensity (dashed lines, $\lambda_{\text{Exc}} = 350 \text{ nm}$) of five different concentrated **CND-*m*-Azo** dispersions. (E) UV-Vis absorbance (solid lines) and PL intensity (dashed lines, $\lambda_{\text{Exc}} = 350 \text{ nm}$) of five different concentrated **CND-*p*-Azo** dispersions. (F) UV-Vis absorbance (solid lines) and PL intensity (dashed lines, $\lambda_{\text{Exc}} = 330 \text{ nm}$) of five different concentrated **CND-*m*-Gly-Azo** dispersions.

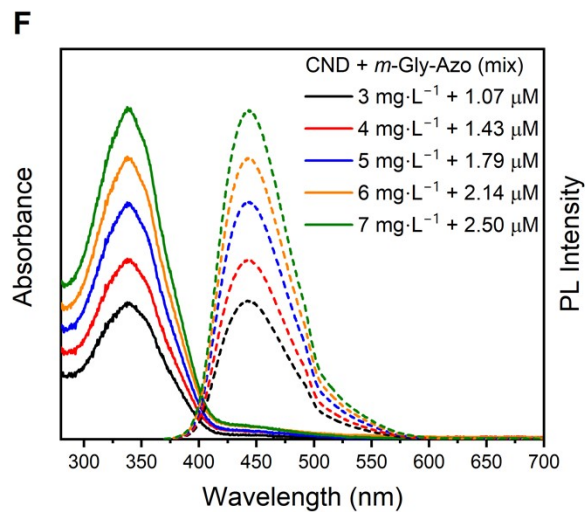
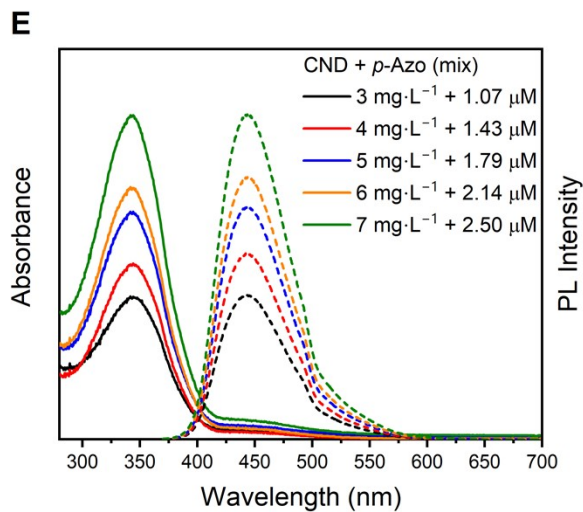
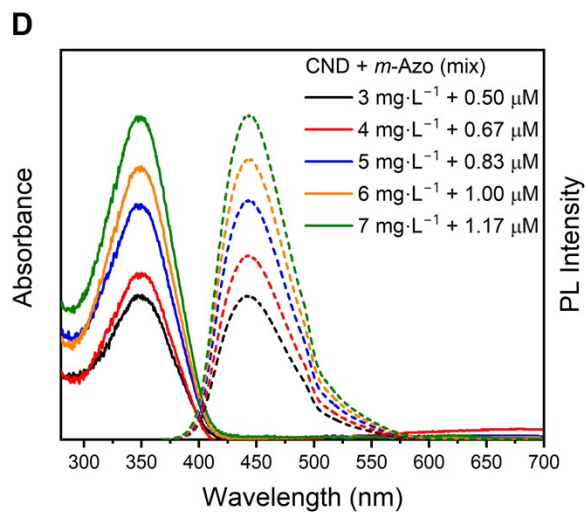
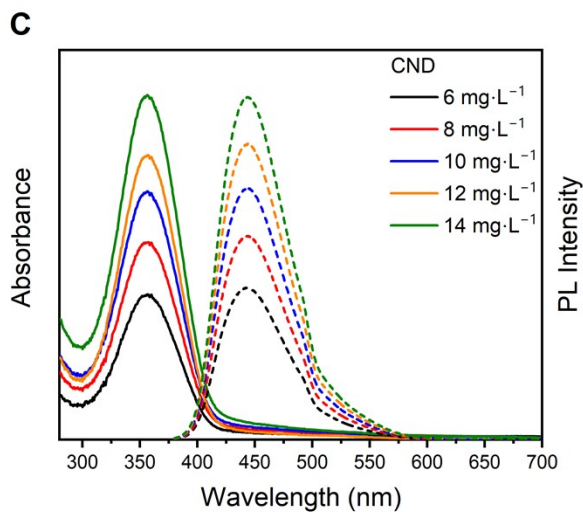
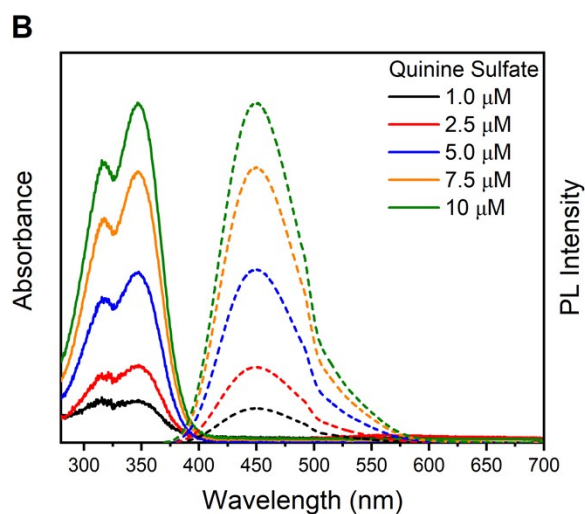
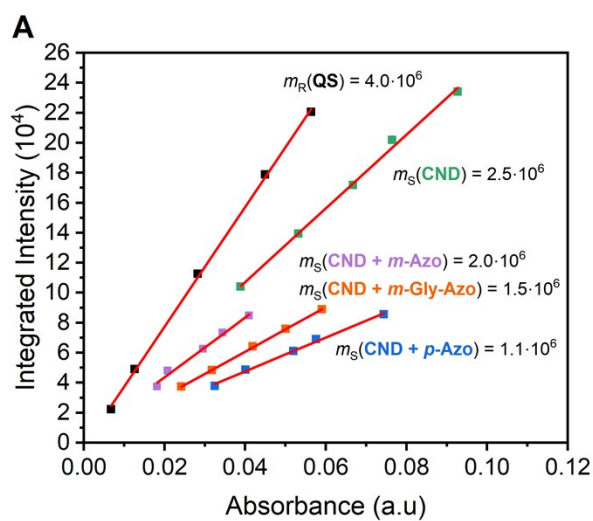


Figure S14. (A) Absorbance maxima plotted against the integrated PL intensity of the five different concentrations and the respective slopes derived from a linear fit. The CNDs and QS are reported twice because of a lamp change in the fluorescence device. (B) UV-Vis absorbance (solid lines) and PL intensity (dashed lines, $\lambda_{\text{Exc}} = 350$ nm) of five different concentrated QS solutions. (C) UV-Vis absorbance (solid lines) and PL intensity (dashed lines, $\lambda_{\text{Exc}} = 360$ nm) of five different concentrated **CND** dispersions. (D) UV-Vis absorbance (solid lines) and PL intensity (dashed lines, $\lambda_{\text{Exc}} = 350$ nm) of five different concentrated **CND + *m*-Azo** physically mixed dispersions. (E) UV-Vis absorbance (solid lines) and PL intensity (dashed lines, $\lambda_{\text{Exc}} = 350$ nm) of five different concentrated **CND + *p*-Azo** physically mixed dispersions. (F) UV-Vis absorbance (solid lines) and PL intensity (dashed lines, $\lambda_{\text{Exc}} = 350$ nm) of five different concentrated **CND + *m*-Gly-Azo** physically mixed dispersions.

Absorption Coefficients and Degree of Azo Functionalization

The UV-Vis absorbance of each azobenzene sample was measured at five different concentrations. The maximum values of each absorbance measurement for the respective concentration were plotted against the concentration. From the obtained slopes and the Law of Lambert-Beer in the following equation, it is possible to determine the absorption coefficient directly.³⁷ In the next step, the respective absorption spectra of the hybrids were deconvoluted with the help of two Lorentzian-shaped functions. The wavelength and the full width at half maximum (FWHM) of the respective pristine azo and the CND were fixed for the Lorentzian functions. The maximum absorbance value for the obtained deconvolution of the azo compartment was used for the calculation of the concentration of azo in the respective hybrid with the depicted equation and the previously determined absorption coefficients. The percentage of azo was calculated in accordance with the concentration of the hybrid utilized for deconvolution.

$$A = \varepsilon_{\lambda} \cdot c \cdot l$$

$$A = \text{absorbance [a.u]}$$

$$\varepsilon_{\lambda} = \text{absorption coefficient at the respective wavelength [L}\cdot\text{g}^{-1}\cdot\text{cm}^{-1}\text{]}$$

$$c = \text{concentration [mg}\cdot\text{L}^{-1}\text{]}$$

$$l = \text{layer thickness of the irradiated body (1 cm)}$$

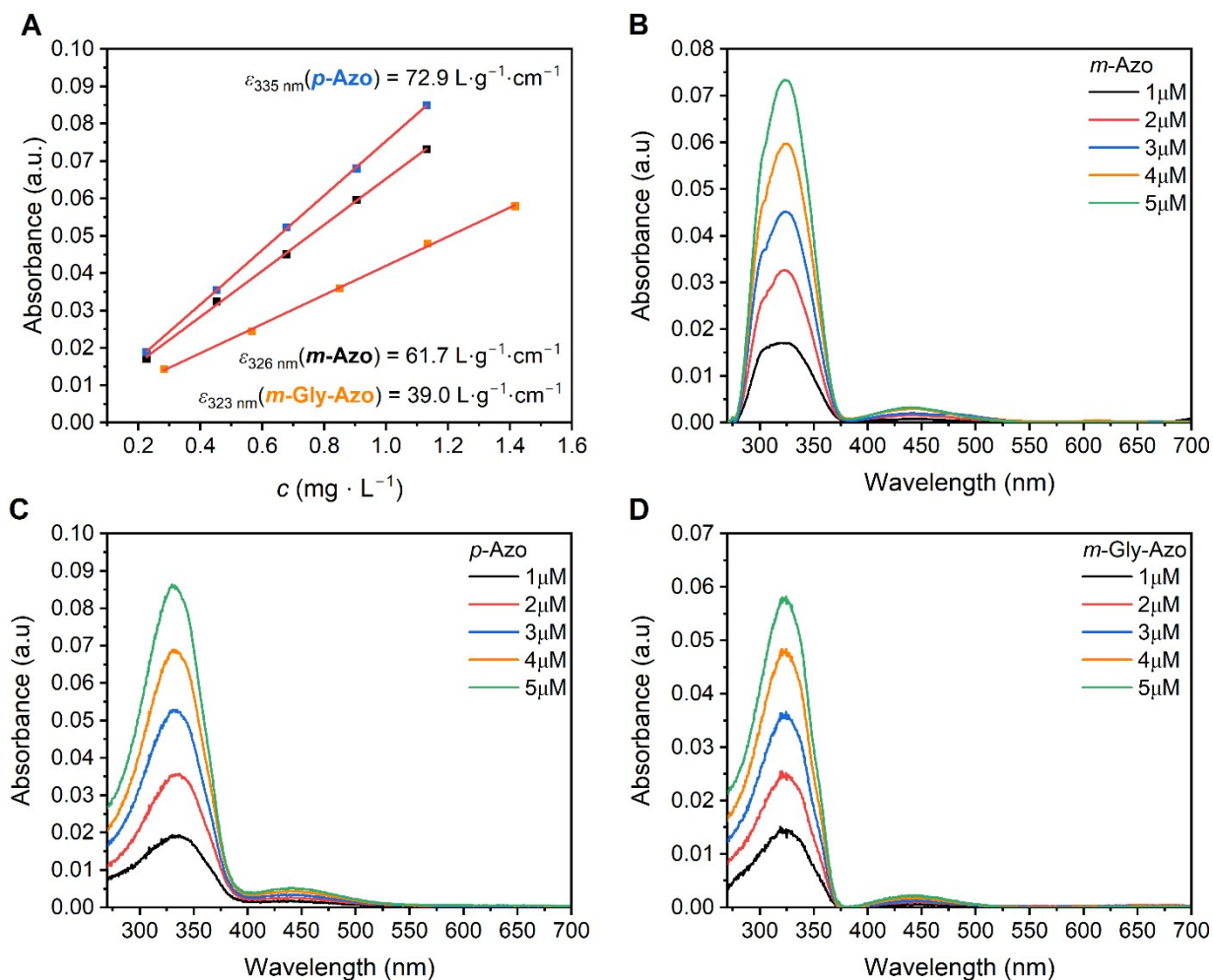


Figure S15. (A) Absorbance maxima of each azobenzene sample at five different concentrations plotted against the concentrations, and the respective slopes (absorption coefficients) derived from a linear fit. (B) UV-Vis absorbance of five different concentrated *m*-Azo solutions ($\lambda_{\text{max}} = 326 \text{ nm}$). (C) UV-Vis absorbance of five different concentrated *p*-Azo solutions ($\lambda_{\text{max}} = 335 \text{ nm}$). (D) UV-Vis absorbance of five different concentrated *m*-Gly-Azo solutions ($\lambda_{\text{max}} = 323 \text{ nm}$).

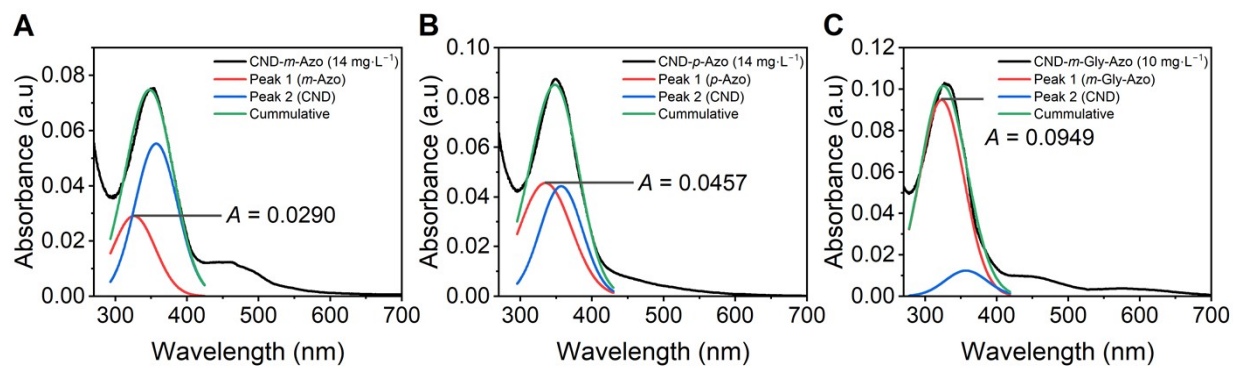


Figure S16. (A) Deconvoluted absorbance spectra of **CND-*m*-Azo** ($14 \text{ mg}\cdot\text{L}^{-1}$ in DMSO) with two Lorentzian-shaped functions. For Peak 1 (***m*-Azo**), the FWHM was fixed at 59 nm, while the position was fixed at 326 nm. A maximum absorbance of 0.0290 was obtained for Peak 1 (***m*-Azo**). This indicates that 3.4% of the hybrid represents the azo component. For Peak 2 (**CND**), the FWHM was fixed at 59 nm, while the position was fixed at 357 nm in all cases. (B) Deconvoluted absorbance spectra of **CND-*p*-Azo** ($14 \text{ mg}\cdot\text{L}^{-1}$ in DMSO) with two Lorentzian-shaped functions. For Peak 1 (***p*-Azo**), the FWHM was fixed at 72 nm, while the position was fixed at 335 nm. A maximum absorbance of 0.0457 was obtained for Peak 1 (***p*-Azo**). This indicates that 4.5% of the hybrid represents the azo component. (C) Deconvoluted absorbance spectra of **CND-*m*-Gly-Azo** ($10 \text{ mg}\cdot\text{L}^{-1}$ in DMSO) with two Lorentzian-shaped functions. For Peak 1 (***m*-Gly-Azo**), the FWHM was fixed at 62 nm, while the position was fixed at 323 nm. A maximum absorbance of 0.0949 was obtained for Peak 1 (***m*-Gly-Azo**). This indicates that 24% of the hybrid represents the azo component.

Computational Analysis

Model of the CND

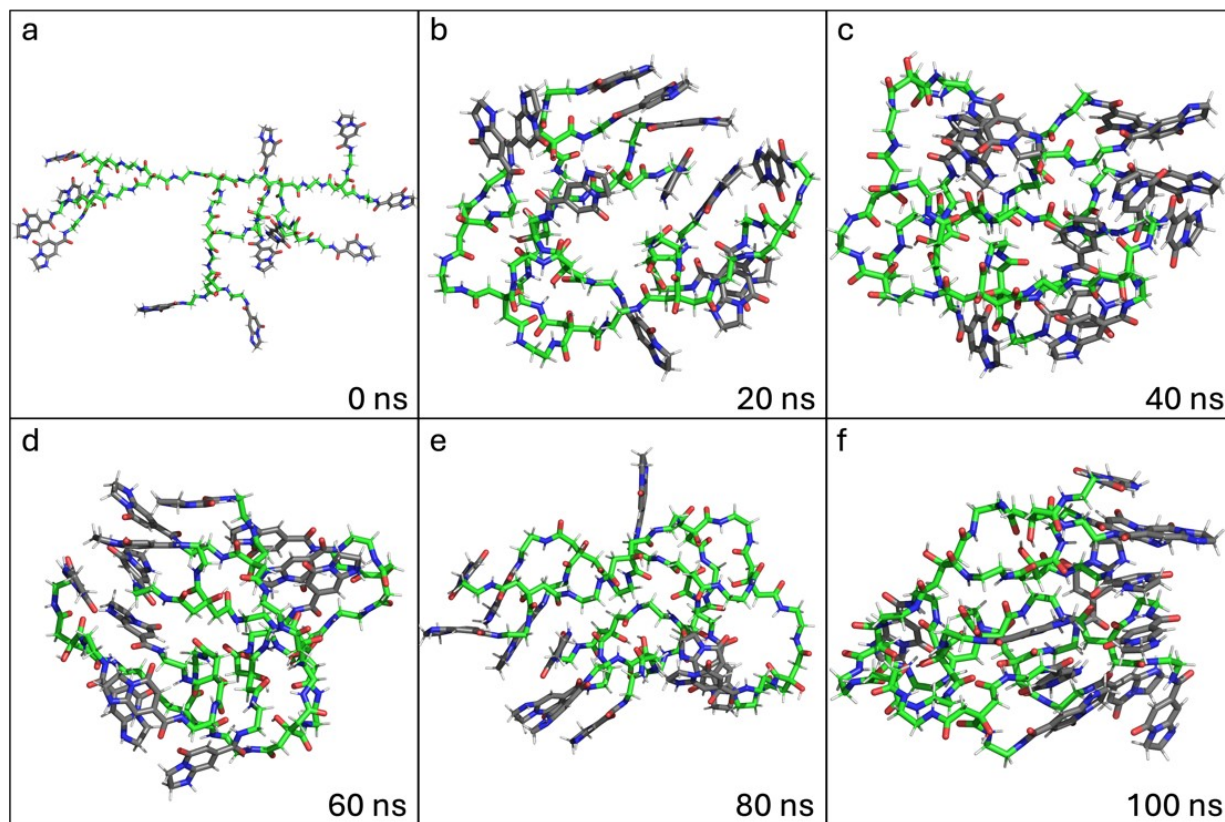


Figure S17. Evolution of polymeric **CND** model as modelled using MD simulations. Coloring scheme: green-carbon; red-oxygen; blue-nitrogen; white-hydrogens. Carbons of IPCA parts of the **CND** are displayed in grey. Water was omitted for clarity.

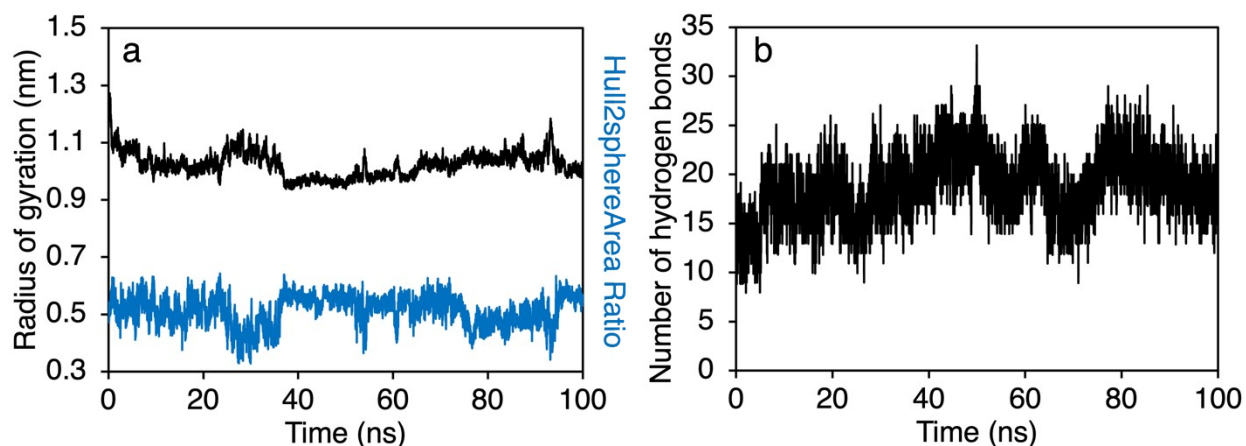


Figure S18. (a) Radius of gyration relaxed after 40 ns in stable self-assembly (black curve). (Please note that the gyration radius differs from the hydrodynamic radius by about 1.5 nm. The hydrodynamic radius reflects the apparent size of the solvated particle, while the gyration radius measures the average distance from the center of mass to the macromolecular surface); Hull2SphereArea ratio displays similar trend as radius of gyration, and it additionally suggests that **CND** is quasi-spherical. Hull2SphereArea³⁸ is the ratio between the surface area of an ideal sphere embedding the whole **CND** and the real **CND** surface area. (b) Evolution of the number of hydrogen bonds formed within **CND** model during the MD simulation.

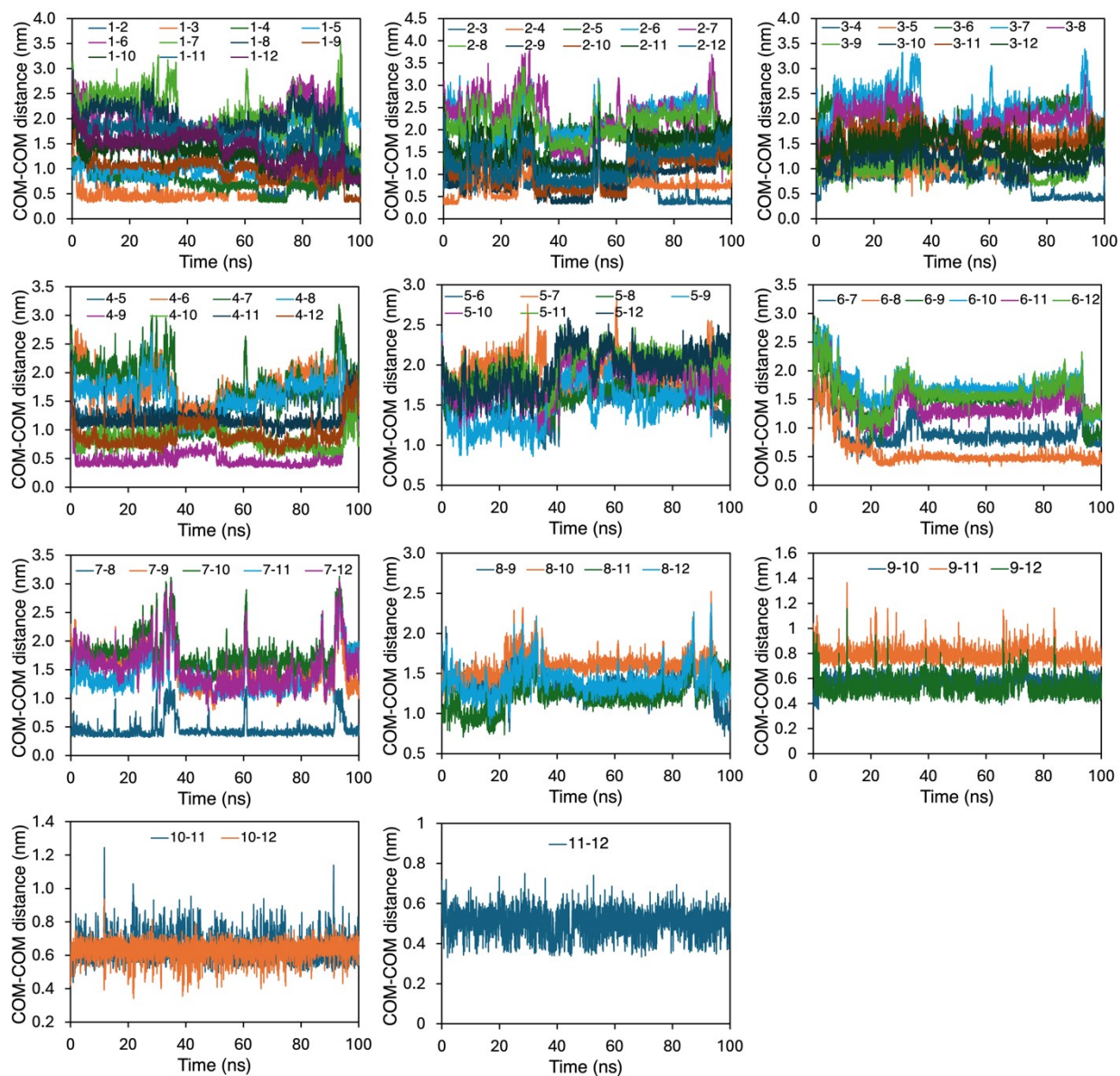


Figure S19. Time evolution of COM-COM distances of 12 IPCA parts of the **CND**, which were collected within 100 ns of the simulation time. Numbers in legends refer to the specific IPCA part of the **CND**.

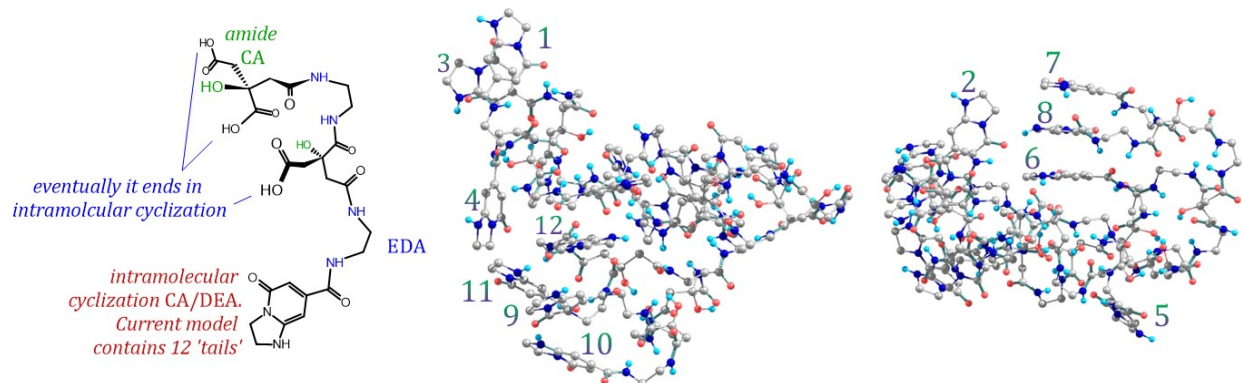
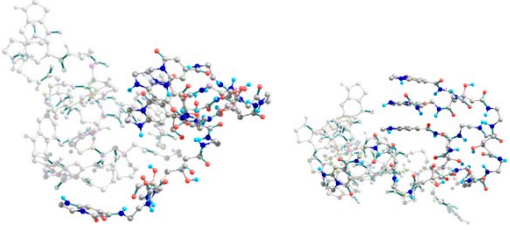
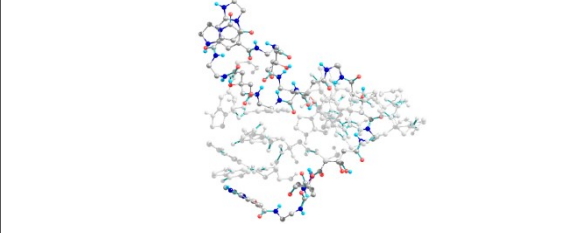
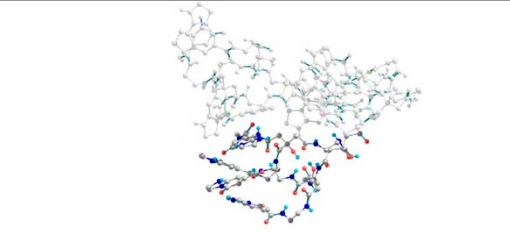
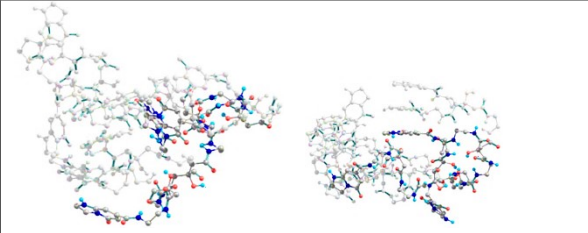
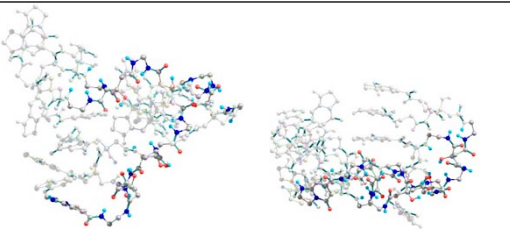
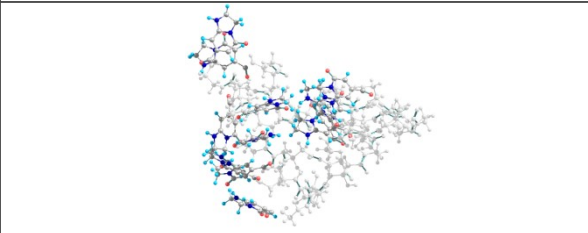


Figure S20. Profile views of the ad-hoc model of polymeric **CND** formed by condensation of citric acid (CA) and ethylene diamine (EDA) as thermally equilibrated via molecular dynamics simulations. Atoms C in grey, N in blue, O in red, and H in cyan.

The Truncated Model of the CND

The model of the **CND** (**Figure S20**) simulated via MD consists of 588 atoms and has the empirical formula $C_{198}N_{66}H_{260}O_{64}$. As a result, a series of truncated models (**trM**) was investigated to perform quantum-chemical calculations, which are reported in **Table S1**. Truncated structures **trM1** to **trM3** exhibit stacked IPCA heterocycles. In contrast, the ring stacking was eliminated in **trM4**, and a few heterocycles were replaced with amide terminals in **trM5**. The amide-alkyl chains were removed in **trM6**, thus preserving exclusively the heterocycles. Our preliminary investigations involved the complete removal of atoms not included in the **trM** models (represented as white-colored fragments in **Table S1**). The respective TDDFT spectra were subsequently calculated and are presented in **Figure S21**.

Table S1. Truncated models (**trM**) of the **CND**. White-colored atoms were either removed for TDDFT calculations or assigned to the medium layer of the ONIOM approach.

	
trM1 (260 atoms, <i>stacking</i>)	trM2 (232 atoms, <i>reduced stacking</i>)
	
trM3 (182 atoms, <i>displaced stacking</i>)	trM4 (206 atoms, <i>non-stacked rings</i>)
	
trM5 (200 atoms, <i>amide tails</i>)	trM6 (228 atoms, <i>only rings</i>)

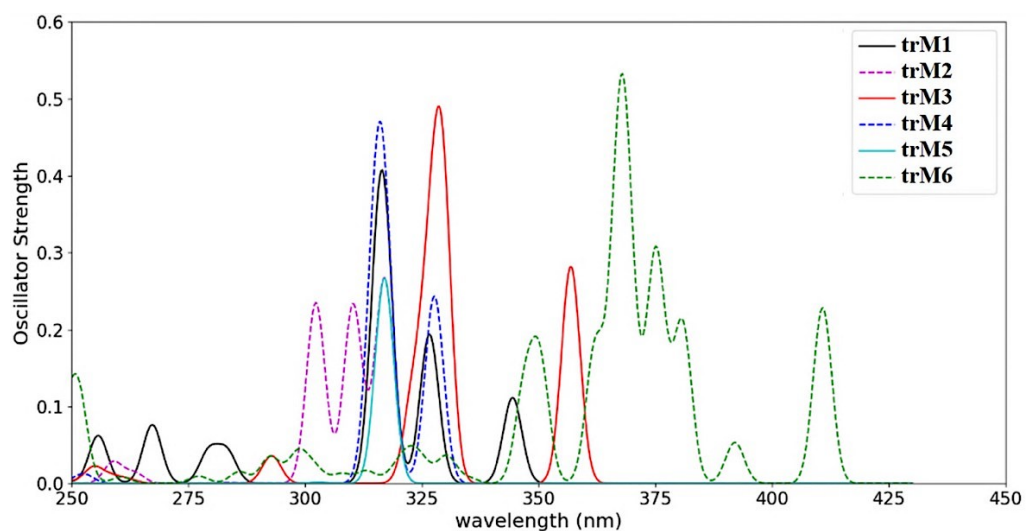


Figure S21. Calculated UV-Vis spectra for the truncated models of the **CND**.

The selection of the truncated model is primarily based on the comparison between calculated and experimental absorption maxima, with the latter observed at $\lambda_{\text{max}} = 357$ nm. The lowest-energy electronic transition (S_1) in model **trM3**, associated with $\lambda = 357$ nm ($f = 0.28$), accurately resembles the experimental λ_{max} . However, another calculated transition in **trM3** was noted as $\lambda_{\text{max}} = 329$ nm ($f = 0.40$). The absorption bands in models **trM1** to **trM5** are blue-shifted relative to those in **trM3**, with λ_{max} values below 325 nm. Model **trM6** exhibited a λ_{max} of 368 nm ($f = 0.20$) and several allowed transitions in the 340–425 nm range, which aligns with the experimental data. However, model **trM6** consists exclusively of IPCA heterocycles, as the amide-alkyl chains were removed. Therefore, we suggest that **trM3** serves as more accurate representation of the real system.

The UV-Vis spectra of model **trM3** were further examined by including the atomic background (represented by the white-colored fragment in **Table S1**) utilizing a lower level of theory. Specifically, TD- ω B97X-D/6-31G(d) was applied to the atoms in **trM3**, while the atomic background was described using either the 3-21G or STO-3G basis sets in the same TD calculation (see **Figure S22**). Additionally, ONIOM calculations were carried out for the system in both the gas phase and in DMSO solution. In these calculations, the atoms in **trM3** were treated as the high layer at the (PCM: DMSO) TD- ω B97X-D/6-31G(d) level, while the atomic background was modeled as the medium layer using the ground-state PM6 method. The absorptions at 357 nm and 329 nm were consistently reproduced across all approaches, with a blue shift and a decrease in intensity observed in the calculations considering the gas phase. The TD- ω B97X-D/6-31G(d)/3-21G method exhibited a greater number of peaks, which are attributed to the non-truncated IPCA heterocycles; although these are virtually missing when the basis set quality is reduced to STO-3G, or when these are excluded from the TDDFT calculation as in the ONIOM medium layer.

Nonetheless, since the main absorptions calculated using ONIOM align with those obtained using TD- ω B97X-D/6-31G(d)/3-21G, we conclude that ONIOM calculations incorporating a semiempirical method for the atomic background are as valid as those obtained via TDDFT.

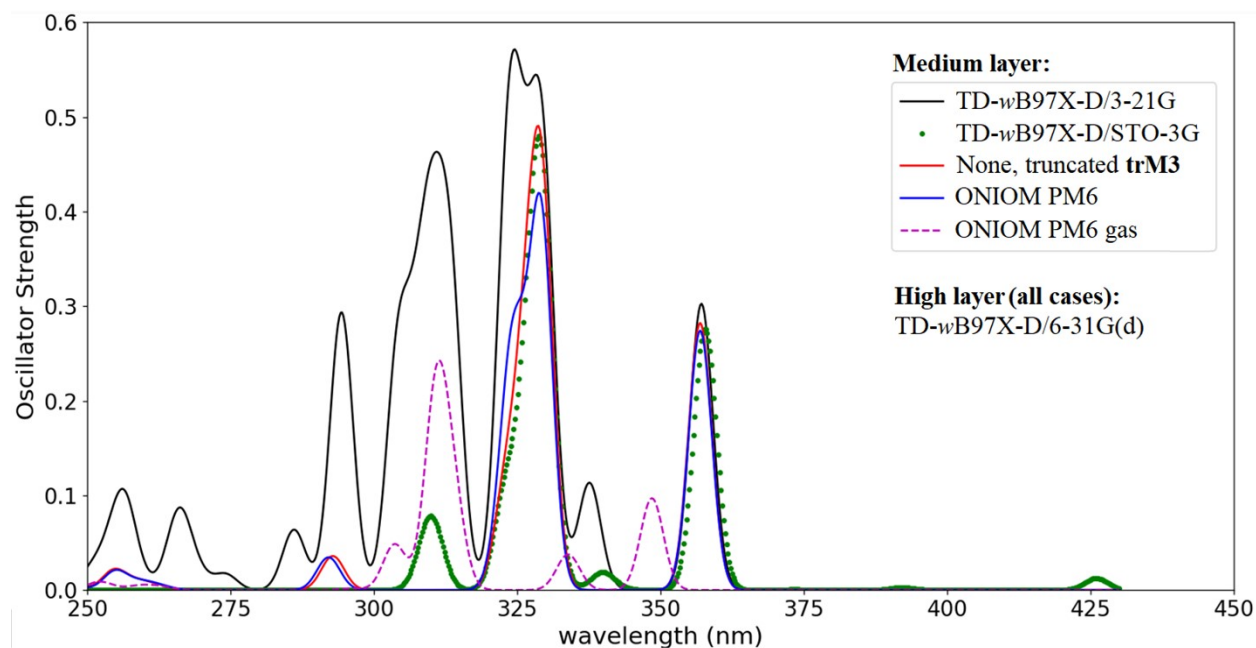


Figure S22. UV-Vis spectra for the truncated model **trM3** of the **CND** excluding and including atomic background calculated via different theoretical approaches. Implicit DMSO solvent was simulated via PCM, unless indicated otherwise.

CNDs Functionalized with Azobenzene

Electron transitions derived from the ONIOM approach are illustrated in **Figure S23** for the unmodified **CND**. We focus on electron transitions associated with excitation energies $\omega > 300$ nm. In addition, transitions are considered allowed when the oscillator strength criterion $f \geq 0.05$ is met (represented with a vertical arrow). Furthermore, a criterion of $\varphi_i \rightarrow \varphi_j > 35\%$ was selected to ensure that significant molecular orbital contributions were not omitted in each electron transition. The lowest-energy transitions S_1 and S_2 exhibited relatively large oscillator strengths.

A visual inspection indicates that S_1 and S_2 are primarily localized π - π^* transitions, although S_1 may be associated with partial charge-transfer (CT) character. These transitions were selected for comparison with azobenzene-modified hybrids, which are discussed in subsequent sections. Additionally, transition S_5 suggests that the system is prone to CT events.

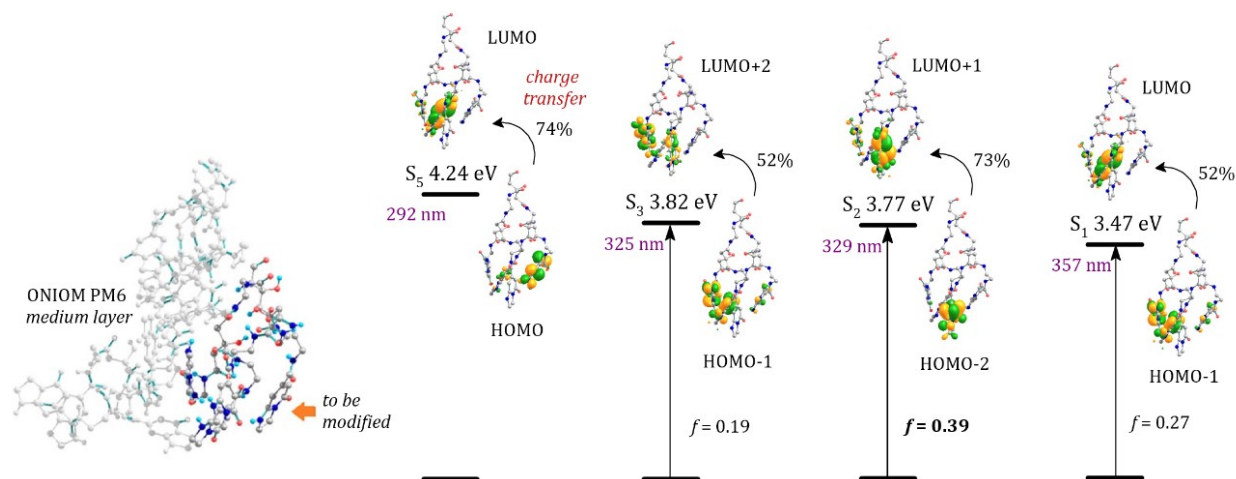


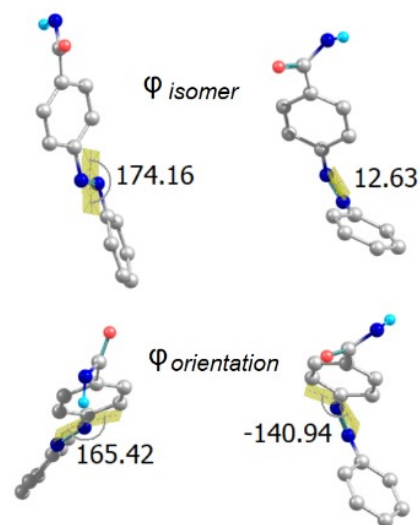
Figure S23. Structure of the **CND** exhibiting the ONIOM medium (in white) and high layers. The five lowest-energy electron transitions calculated in the high layer are also illustrated. (S_4 is omitted due to an artificial transition in the C=O fragment where the model is truncated).

The **CND** structure depicted in **Figure S20** contains 12 IPCA heterocycles. Initially, one heterocycle moiety was replaced with one equivalent of *para*-azobenzene, leading to 12 distinct conformers of **CND-*p*-Azo** (the labeling scheme was provided in **Figure S20**). Each structure was characterized by dihedral angles φ measured in the azo fragment. *Cis/trans* isomerism was reported by φ_{iso} , a dihedral angle defined by $\text{C}_{\text{ipso}}\text{-N}\equiv\text{N-C}_{\text{ipso}}$. Accordingly, the *cis* isomer was characterized as $\varphi_{\text{iso}} \rightarrow 0^\circ$, and the *trans* counterpart as $\varphi_{\text{iso}} > |120^\circ|$. The orientation of the terminal phenyl group of the azobenzene fragment was determined via φ_{ori} ($\text{C}_{\text{ortho}}\text{-C}_{\text{ipso}}\text{-N}\equiv\text{N}$), so that two *trans*-azo conformers were characterized, *trans*₀ when $\varphi_{\text{ori}} \rightarrow 0^\circ$ and *trans* for $\varphi_{\text{ori}} > |120^\circ|$. This dihedral

angle is less relevant for the *cis* counterpart. The relative thermodynamic stabilization of the **CND-*p*-Azo** conformers is reported in **Table S2**, with the replacement of heterocycle label 10 yielding the most stabilized functionalization (this ring is also indicated in **Figure S23**). Additionally, the other azobenzene derivatives were also incorporated at the position of heterocycle 10 of the **CND** (see **Figure S24**). In the case of isolated azobenzene derivatives (**Azo**), the initial structures were extracted from the equilibrated geometries of the **CND-Azo** hybrids, thus resulting in a root mean square deviation smaller than 0.6 Å after geometry optimization of **Azo**.

Table S2. Comparisons of electronic and Gibbs energies (in kcal/mol) for the conformers of **CND-*p*-Azo** calculated at the GFN2-xTB level. Dihedral angles φ (in degrees) are schematized for the most stabilized structure (highlighted in bold).

Replaced heterocycle	Azo isomer	φ_{iso}	φ_{ori}	ΔE_{rel}	ΔG_{rel}
1	<i>cis</i>	14.4	46.8	9.5	10.5
	<i>trans</i> ₀	-178.2	29.5	19.4	16.9
	<i>trans</i>	178.6	-151.7	16.8	16.0
2	<i>cis</i>	13.1	-42.8	10.4	10.2
	<i>trans'</i> ₀	171.5	-29.8	9.8	11.6
	<i>trans</i> ₀	176.1	-27.1	12.9	14.4
	<i>trans</i>	178.8	158.3	13.3	14.0
3	<i>cis</i>	15.6	-140.9	15.6	13.2
	<i>trans</i> ₀	177.5	-29.4	16.1	13.7
	<i>trans</i>	173.9	153.2	17.0	15.2
4	<i>cis</i>	13.1	53.0	13.3	12.0
	<i>trans</i> ₀	174.6	-40.1	13.6	12.4
	<i>trans</i>	175.5	149.9	13.6	13.2
5	<i>cis</i>	13.1	45.2	13.5	12.8
	<i>trans</i> ₀	172.3	-31.4	14.2	12.8
	<i>trans</i>	175.4	146.0	11.7	12.3
6	<i>cis</i>	-9.1	-50.3	14.2	15.1
	<i>trans</i>	-179.2	-156.8	14.1	14.0
7	<i>cis</i>	-13.5	138.2	14.7	13.3
	<i>trans</i> ₀	176.2	22.6	19.5	17.1
	<i>trans</i>	-172.9	-152.4	17.5	18.3



8†	<i>trans</i> ₀	170.2	-33.8	18.4	18.6
	<i>trans</i>	174.0	148.9	17.5	16.1
9	<i>cis</i>	12.9	-128.8	15.6	14.1
	<i>cis'</i>	13.4	48.7	14.4	15.3
	<i>trans</i> ₀	174.4	-29.4	16.8	16.4
	<i>trans</i>	-172.9	-151.9	16.8	15.9
10	<i>cis'</i>	13.2	-135.0	16.0	15.4
	<i>cis</i>	12.6	-140.9	0.0	0.0
	<i>trans</i> ₀	-177.1	-25.4	16.2	16.0
	<i>trans</i>	174.2	165.4	2.9	3.4
11	<i>cis</i>	12.1	-128.1	13.3	12.2
	<i>trans</i> ₀	-177.4	-26.2	17.5	15.6
	<i>trans</i>	172.2	153.7	17.7	17.5
12†	<i>trans</i> ₀	174.4	14.4	17.6	17.9
	<i>trans</i>	-179.8	-165.5	14.6	15.0

† Cis isomer is not possible due to structural restrictions.

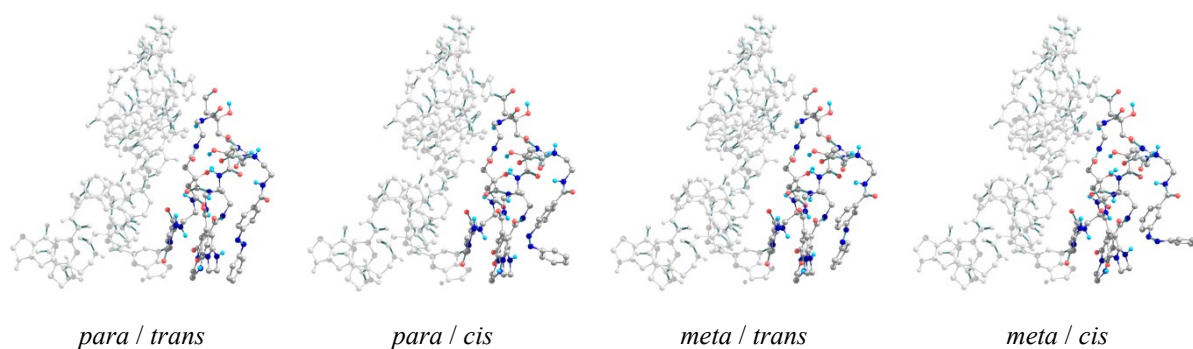


Figure S24. Structures of the CND functionalized with azo isomers, **CND-Azo**.

Isomer *Cis* of Azobenzene and Corresponding CND hybrids

The experimental spectra of the **CND**, *cis*-**Azo** and the respective **CND-Azo** hybrid are illustrated in **Figure S25**. In both *meta* and *para* azobenzene derivatives, it was observed that main peaks of *cis*-**Azo** and **CND-Azo** hybrids are shifted to smaller wavelengths ($\omega < 300$ nm). However, the experimental spectra exhibited nearly overlapped peaks of **CND**, *cis*-**Azo** and **CND-Azo** in the 300–400 nm range.

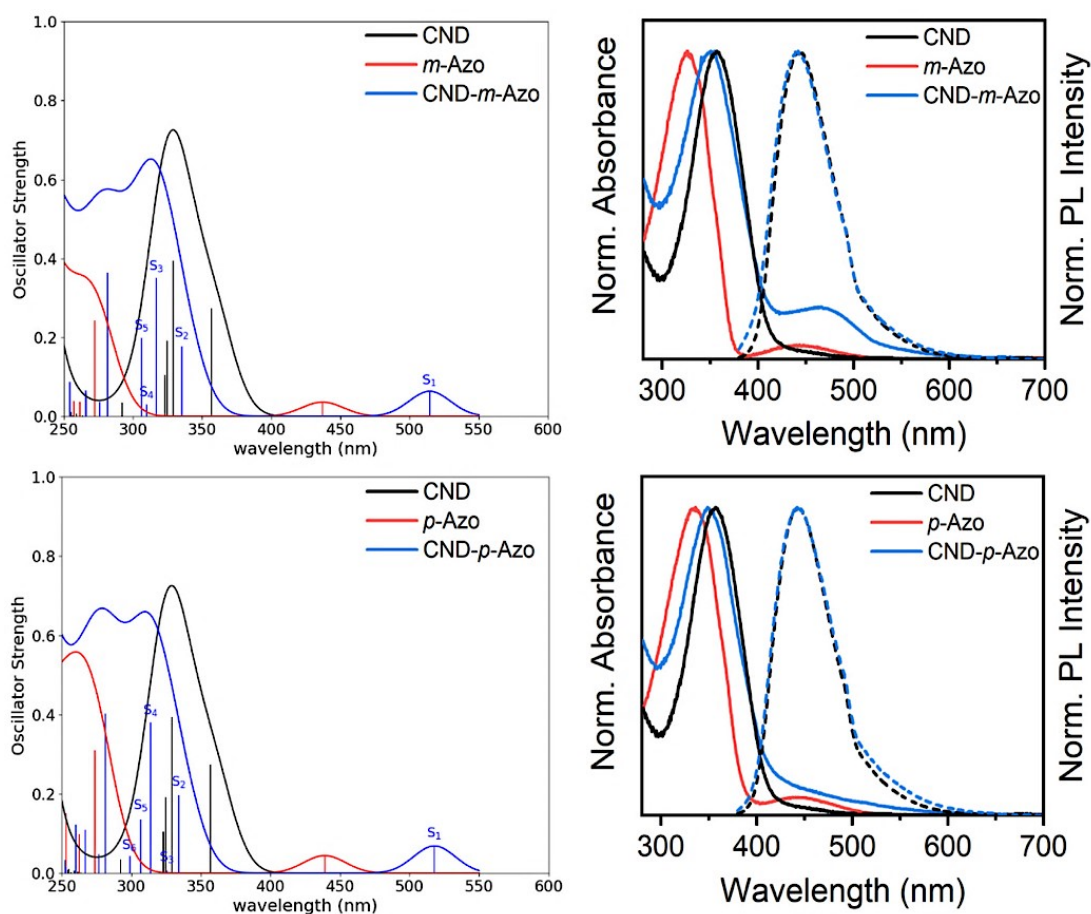


Figure S25. Comparisons between calculated and experimental spectra of the **CND**, the *cis* isomer of azobenzene, and the respective **CND-Azo** hybrids. For latter, the lowest-energy electron transitions S_n are also indicated.

The conversion of the isomer *cis* to *trans* was experimentally induced by light absorption utilizing a wavelength of 450 nm. The TDDFT results of *cis*-**Azo** exhibit a HOMO-LUMO transition at 439 nm for the *para* conformer and 437 nm for the *meta* counterpart, both weak due to $f = 0.04$ (see also **Figures S26** and **S27**). However, the equivalent transition in the **CND-Azo** hybrid (isomer *cis*) was calculated at 518 nm and 515 nm for the *para* and *meta* cases ($f = 0.07$), respectively. In this context, it was mentioned that the peaks for the isomer *cis* are displaced compared with the experimental evidence, therefore let us discuss the *trans* isomer in the next subsection.

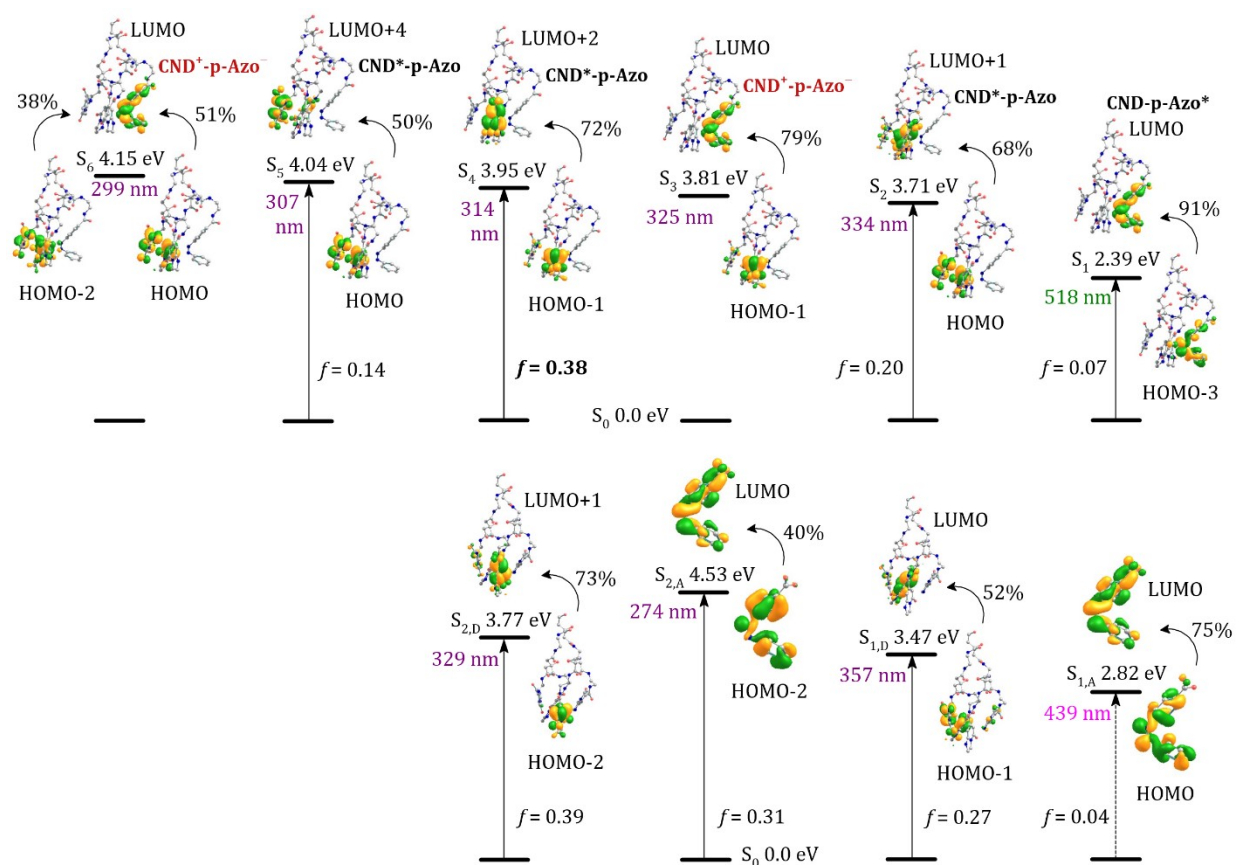


Figure S26. (Bottom) Lowest-energy electron transitions in the CND (S_{n,D}), in the isomer *cis* of *para*-azobenzene (S_{n,A}), (top) and in the **CND-p-Azo**. The transitions in the substrates (bottom) are aligned with those in the hybrid (top), if available.

Note: Henceforth, illustrations of transitions in the hybrid correspond to $\omega > 300$ nm, and those with $f \geq 0.05$ are represented with a vertical arrow. Orbital contributions are depicted under the criterion $\phi_i \rightarrow \phi_j > 35\%$. For **Azo** compounds, $S_{1,A}$ is depicted along with the transition with the largest f value ($S_{2,A}$ in most cases). For clarity, the ONIOM medium layer was omitted in all diagrams.

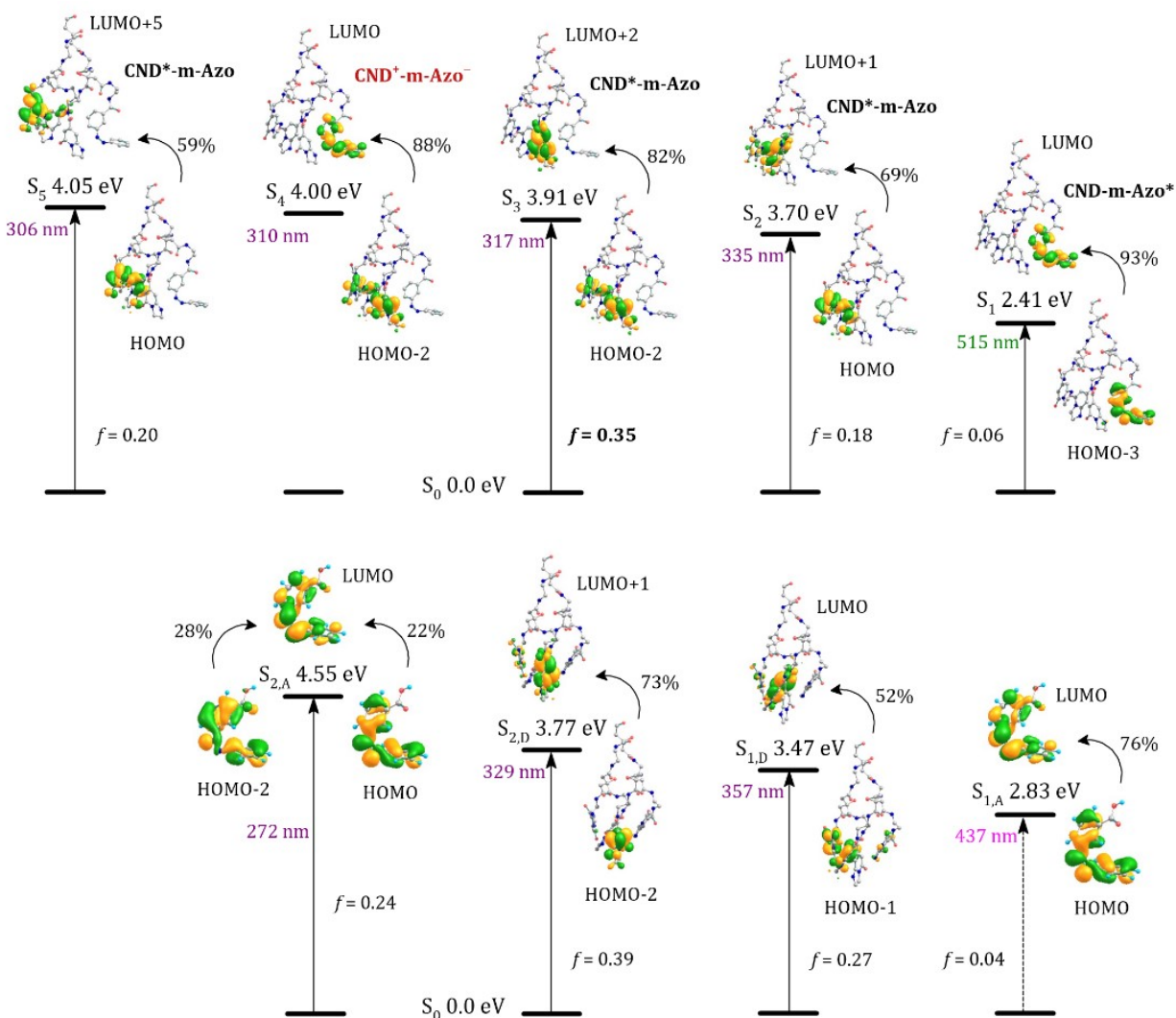


Figure S27. (Bottom) Lowest-energy electron transitions in the **CND** ($S_{n,D}$), in the isomer *cis* of *meta*-azobenzene ($S_{n,A}$), (top) and in the **CND-m-Azo**. The transitions in the substrates (bottom) are aligned with those in the hybrid (top), if available.

Isomer *Trans* of Azobenzene and Corresponding CND hybrids

In line with the description provided in the previous subsection, the calculated spectra for both the *para* and *meta* configurations of *trans*-Azo and their respective hybrids show a closer agreement with experimental data (see **Figure S28**). These findings suggest that the *trans* configuration of azobenzene in the **CND-Azo** hybrid is predominant in the electron transitions.

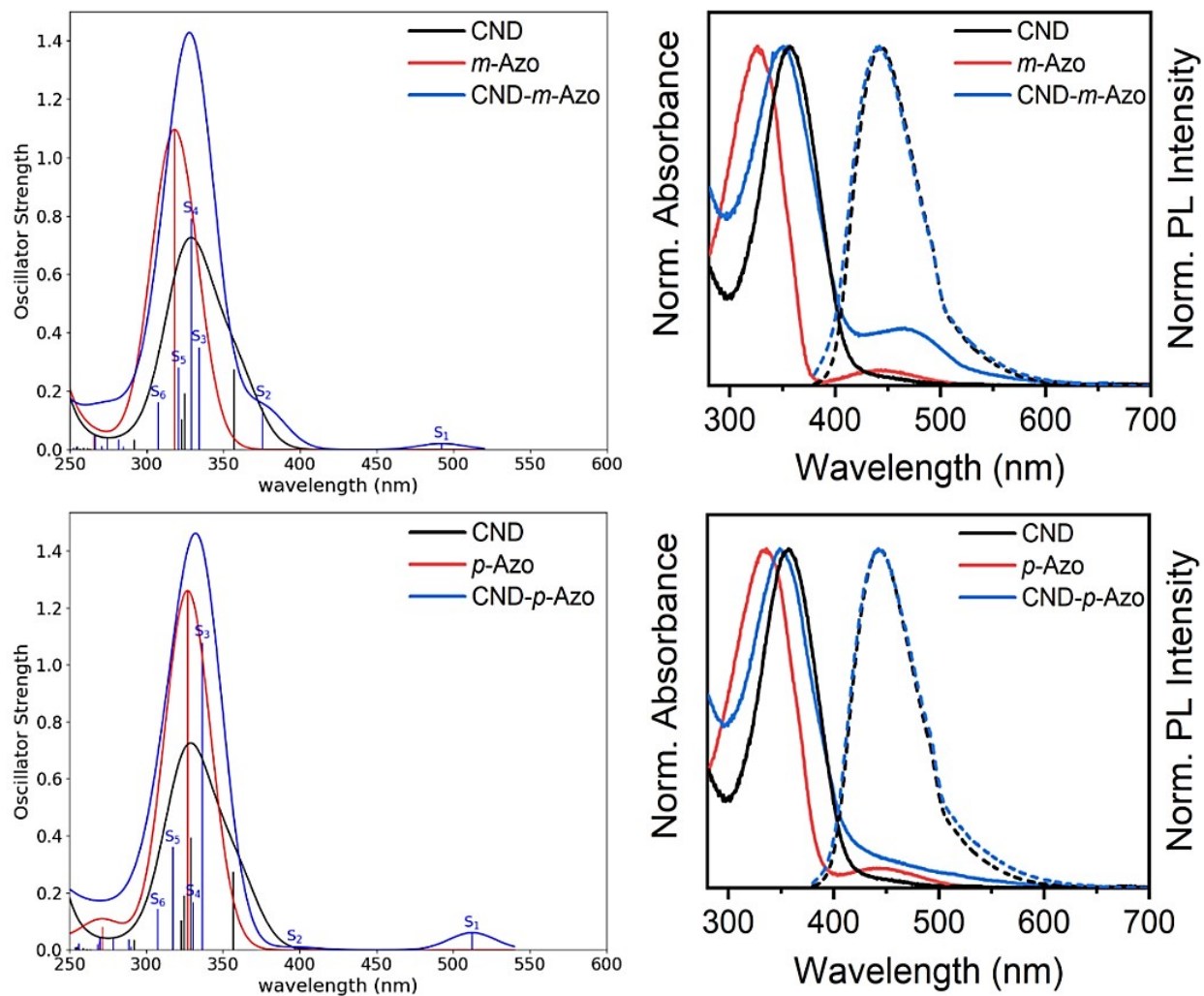


Figure S28. Comparisons between calculated and experimental spectra of the **CND**, the *trans* isomer of azobenzene, and the respective **CND-Azo** hybrids. For this latter, the lowest-energy electron transitions S_n are also indicated.

Experimental investigations determined that the conversion of the *trans* to *cis* isomer was achieved using light with a wavelength of 340 nm. TDDFT results for the *trans*-**Azo** isomer show a HOMO-1 to LUMO transition at 465 nm for the *para* conformer and at 453 nm for the *meta* conformer; these transitions are forbidden with an oscillator strength of $f=0.00$ (see also **Figures S29** and **S30**). This result confirms that the weak peak observed at 450 nm in the experimental spectrum of the **Azo** compound (red line) corresponds to the *cis* isomer in both the *para* and *meta* configurations. However, for the **CND-Azo** hybrid, we observed weak peaks in the visible region for all cases: 518 nm for *para/cis*, 515 nm for *meta/cis*, 513 nm for *para/trans*, and 492 nm for *meta/trans*. The blue line in the experimental spectra of the **CND-Azo** hybrid extends from 450 nm to 600 nm. We infer that the 450 nm irradiation used for converting the *cis*-**Azo** to the *trans* isomer in **CND-Azo** may overlap with electronic transitions occurring within the hybrid.

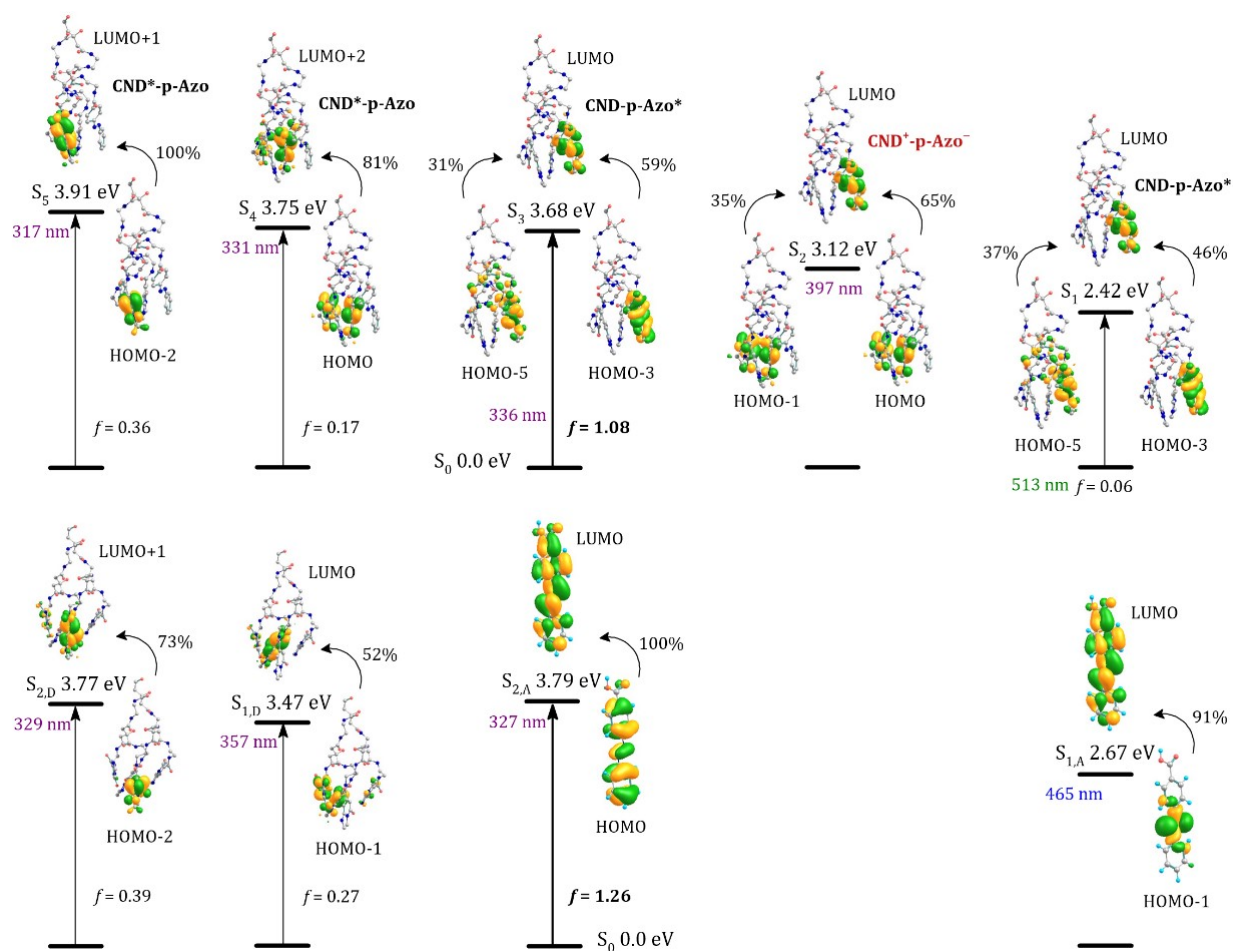


Figure S29. (Bottom) Lowest-energy electron transitions in the **CND** ($S_{n,D}$), in the isomer *trans* of *para*-azobenzene ($S_{n,A}$), (top) and in the **CND-*p*-Azo**. The transitions in the substrates (bottom) are aligned with those in the hybrid (top), if available.

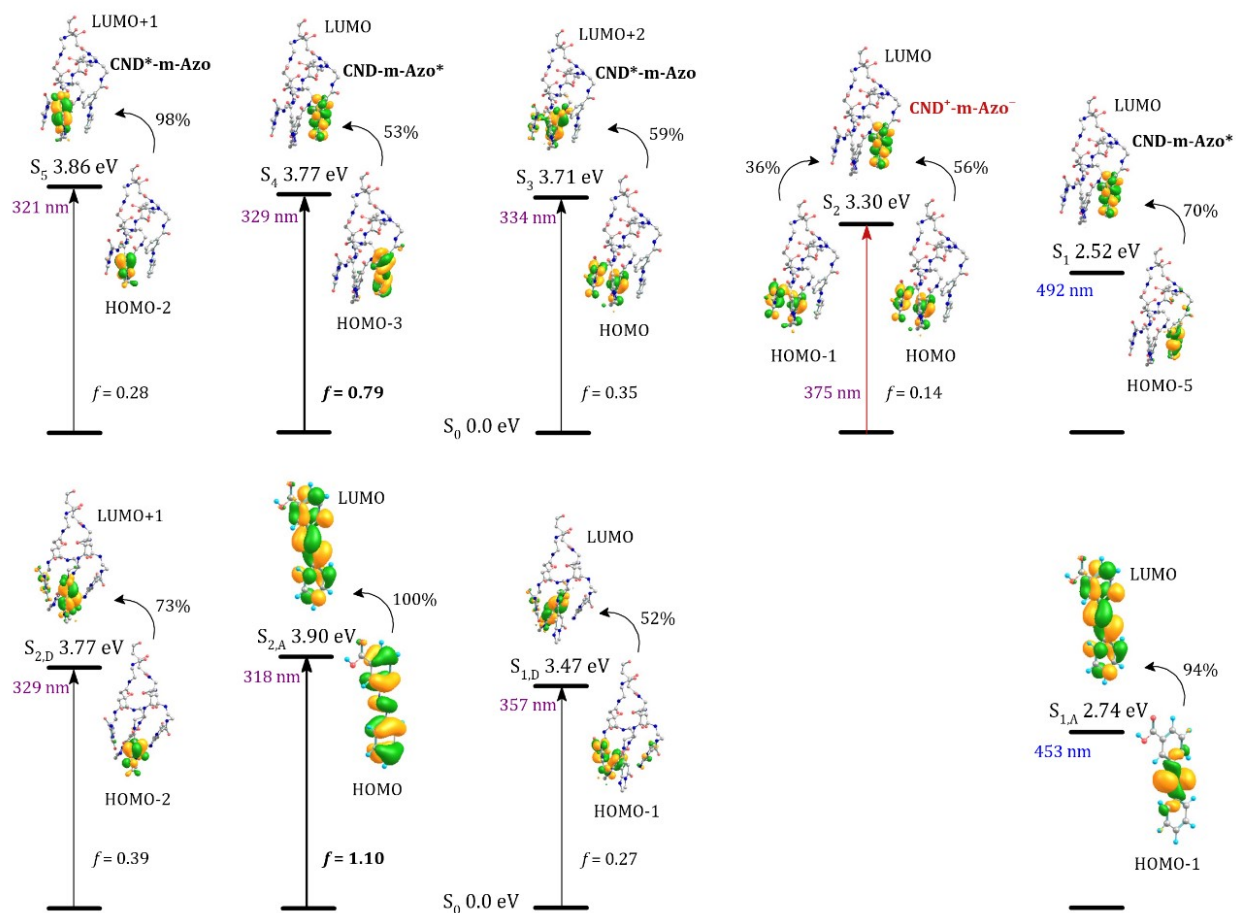


Figure S30. (Bottom) Lowest-energy electron transitions in the **CND** ($S_{n,D}$), in the isomer *trans* of *meta*-azobenzene ($S_{n,A}$), (top) and in the **CND-*m*-Azo**. The transitions in the substrates (bottom) are aligned with those in the hybrid (top), if available.

Meta-Glycine-Azobenzene and Corresponding CND hybrids

Azobenzene was additionally functionalized by incorporating a glycine unit at the *meta* position of the **Azo** moiety. The GFN2-xTB optimized structures are depicted in **Figure S31**. The HOMO and LUMO levels and energy gap E_g exhibited a similar trend to those reported in the previous subsection:

- The HOMO level remains unaltered (7.0 eV) through **CND** and hybrids. Therefore, E_g is primarily altered by the LUMO level.
- LUMO is more stabilized for the **CND-*m*-Gly-Azo** hybrids, as compared with the unmodified **CND**.
- LUMO is more stabilized for the *trans* isomers, as compared with the *cis* counterparts.

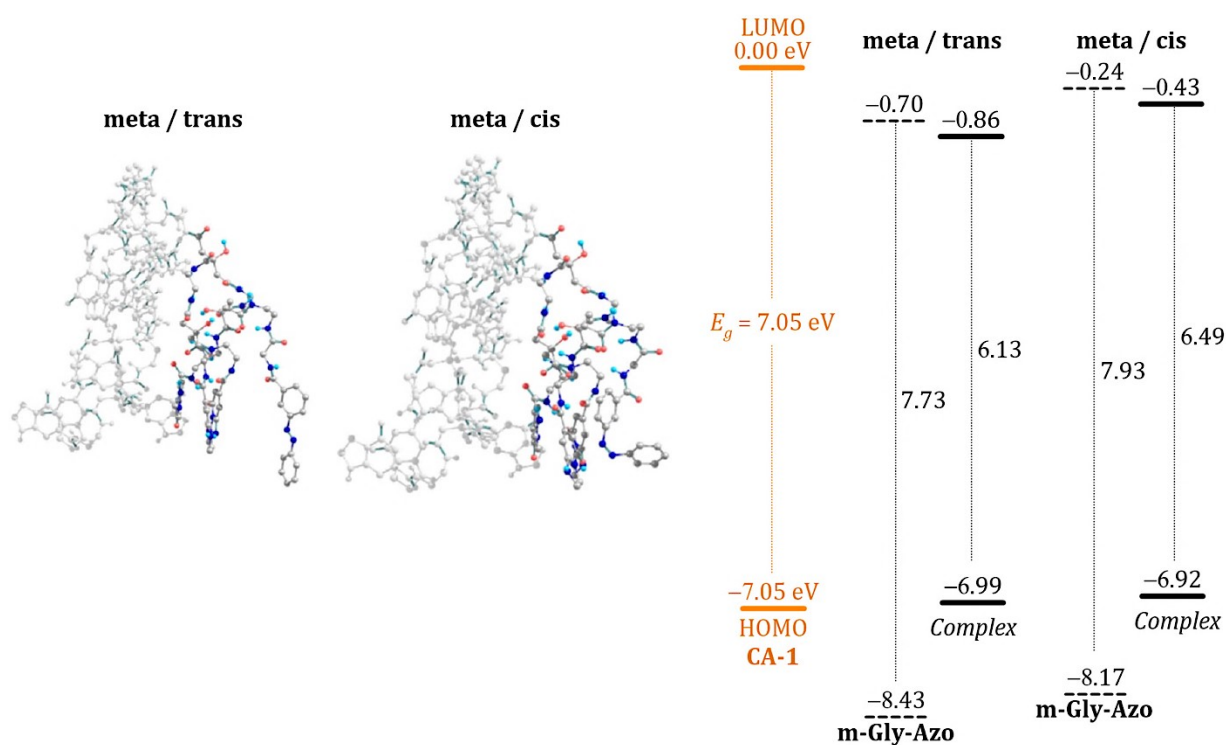


Figure S31. Structures of the **CND** functionalized with ***m*-Gly-Azo**. HOMO and LUMO levels and energy gaps in eV for the **CND** (in orange), ***m*-Gly-Azo** compounds, and the respective **CND-*m*-Gly-Azo**.

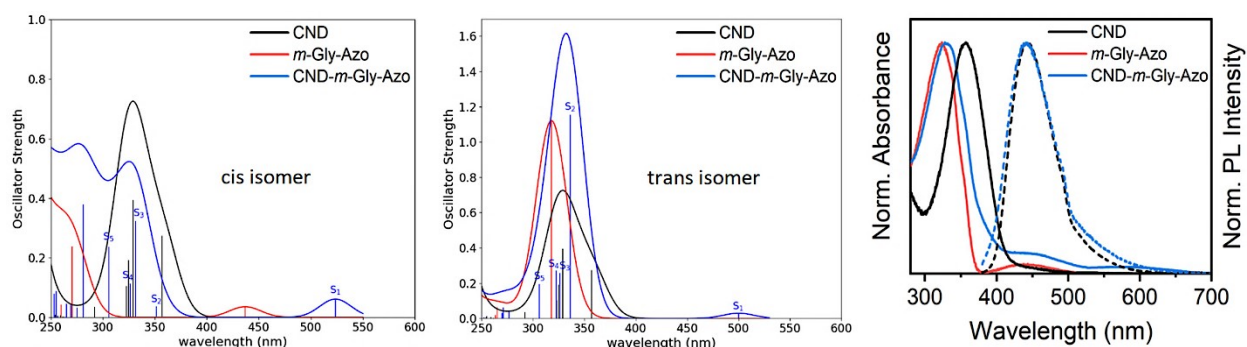


Figure S32. Comparisons between calculated and experimental spectra of the **CND**, the *meta* conformer of azobenzene attached to a glycine unit, and the respective **CND-*m*-Gly-Azo** hybrids. For this latter, the lowest-energy electron transitions S_n are also indicated.

The electronic spectra of the compound and hybrids incorporating glycine at the *meta* position exhibited a similar trend to those reported in previous subsections (see **Figure S32**). Specifically, the main peaks of the **CND-*m*-Gly-Azo** hybrid containing the cis isomer of the azobenzene fragment are shifted to shorter wavelengths (<300 nm). Therefore, the *trans* configuration is considered the predominant isomer of the azobenzene moiety, as evidenced by the nearly overlapping peaks, consistent with our previous conclusion.

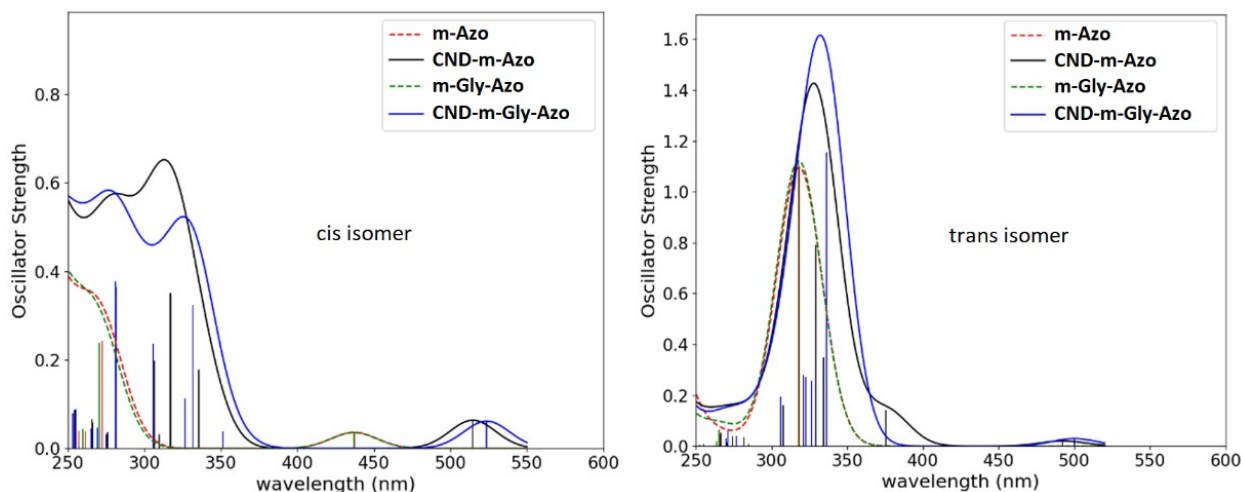


Figure S33. Calculated spectra of azobenzene and hybrids modified with a glycine spacer compared with non-modified counterparts.

Finally, in **Figure S33**, the calculated spectra for ***m*-Gly-Azo** and the **CND-*m*-Gly-Azo** hybrids are compared with those for ***m*-Azo** and **CND-*m*-Azo**. The spectra for the *cis* isomer of azobenzene exhibit similar features, with slight variations in oscillator strength values for certain peaks in the respective hybrids. This trend is also observed in the *trans* isomer, although the **CND-*m*-Azo** hybrid displays a shoulder around 375 nm. However, it should be noted that the *trans*-azo fragment in **CND-*m*-Gly-Azo** is located at $d = 7.95 \text{ \AA}$, where d stands for the molecular distance between **CND** structure and the azo fragment (see **Figure S34**, bottom section, for a graphical representation of parameter d). For the *trans*-azo fragment, the localized transitions in **CND*-*m*-Azo** (S_3 and S_5) and **CND-*m*-Azo*** (S_1 and S_4) are nearly identical to those in the hybrids with the molecular spacer (see dashed lines in **Figure S34**, bottom): $\Delta\omega < 10 \text{ nm}$, $\Delta f < 0.1$ (except for S_4 **CND-*m*-Azo***), same or similar major $\phi_i \rightarrow \phi_j$ orbital contributions. A similar trend was observed for the hybrids containing the *cis* conformation of the azobenzene moiety (e.g., see dashed lines for S_5 of **CND*-*m*-Azo** in **Figure S35**, from the middle to the bottom sections). However, when $d < 4 \text{ \AA}$, the *cis* **CND-*m*-Gly-Azo** hybrid exhibited a more stabilized charge-transfer excited state than the corresponding state in *cis* **CND-*m*-Azo** (see dashed lines in **Figure S35**, from the top to the middle sections). To explore this, we investigated the variation of the electronic transitions as a function of the distance between the azobenzene fragment and the main structure of **CND**. The overall results reported in **Figures S34** and **S35** suggest that the flexibility provided by the glycine spacer either induces (when $d < 4 \text{ \AA}$) or precludes (when $d > 6 \text{ \AA}$) the formation of charge-transfer states.

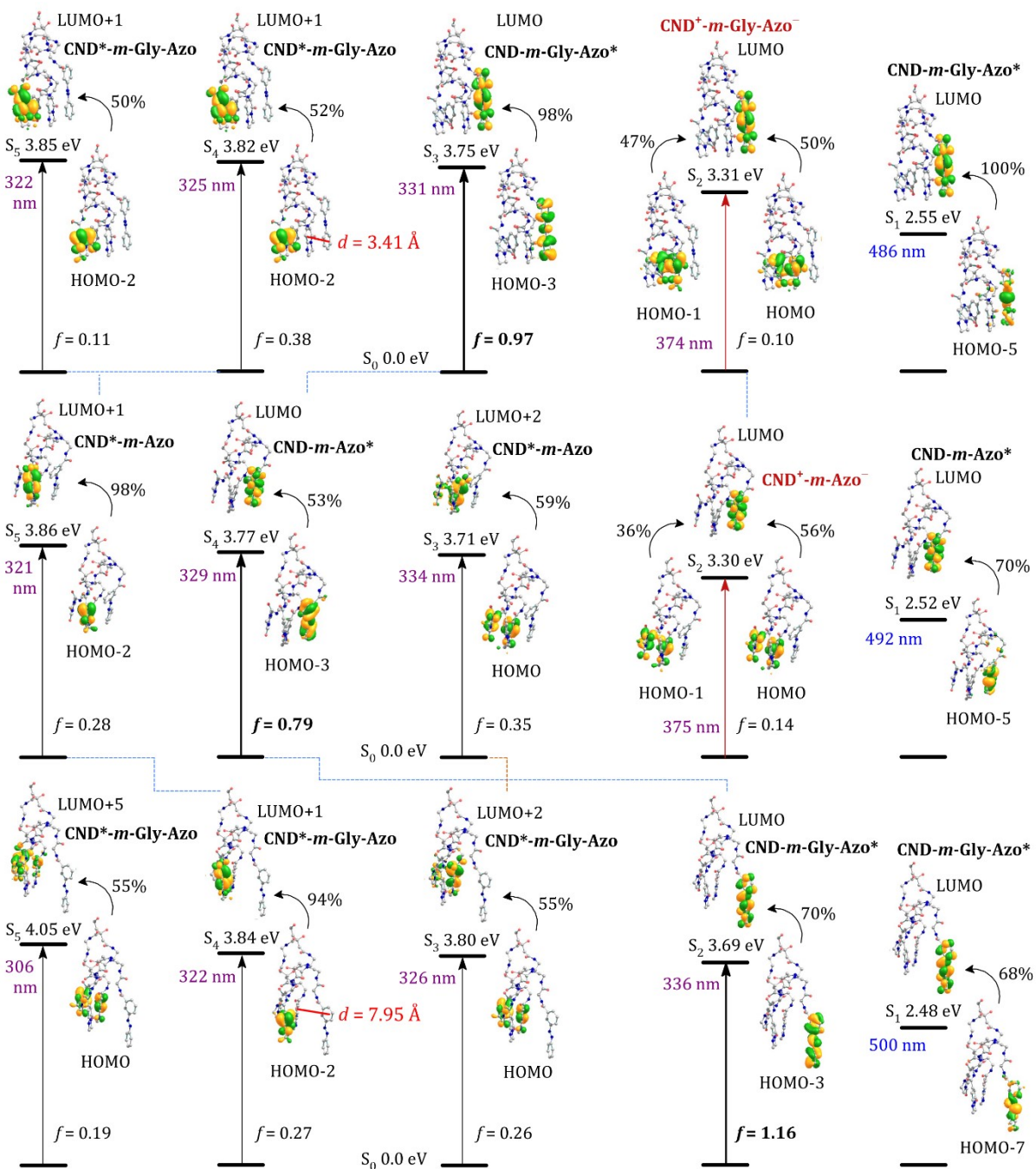


Figure S34. Lowest-energy electronic transitions in **CND-*m*-Azo** (*middle*) compared with **CND-*m*-Gly-Azo**. The hybrids incorporate the *trans* isomer of the azobenzene fragment, positioned either closer to (*top*) or farther from (*bottom*) the nearest IPCA centroid of the CND fragment.

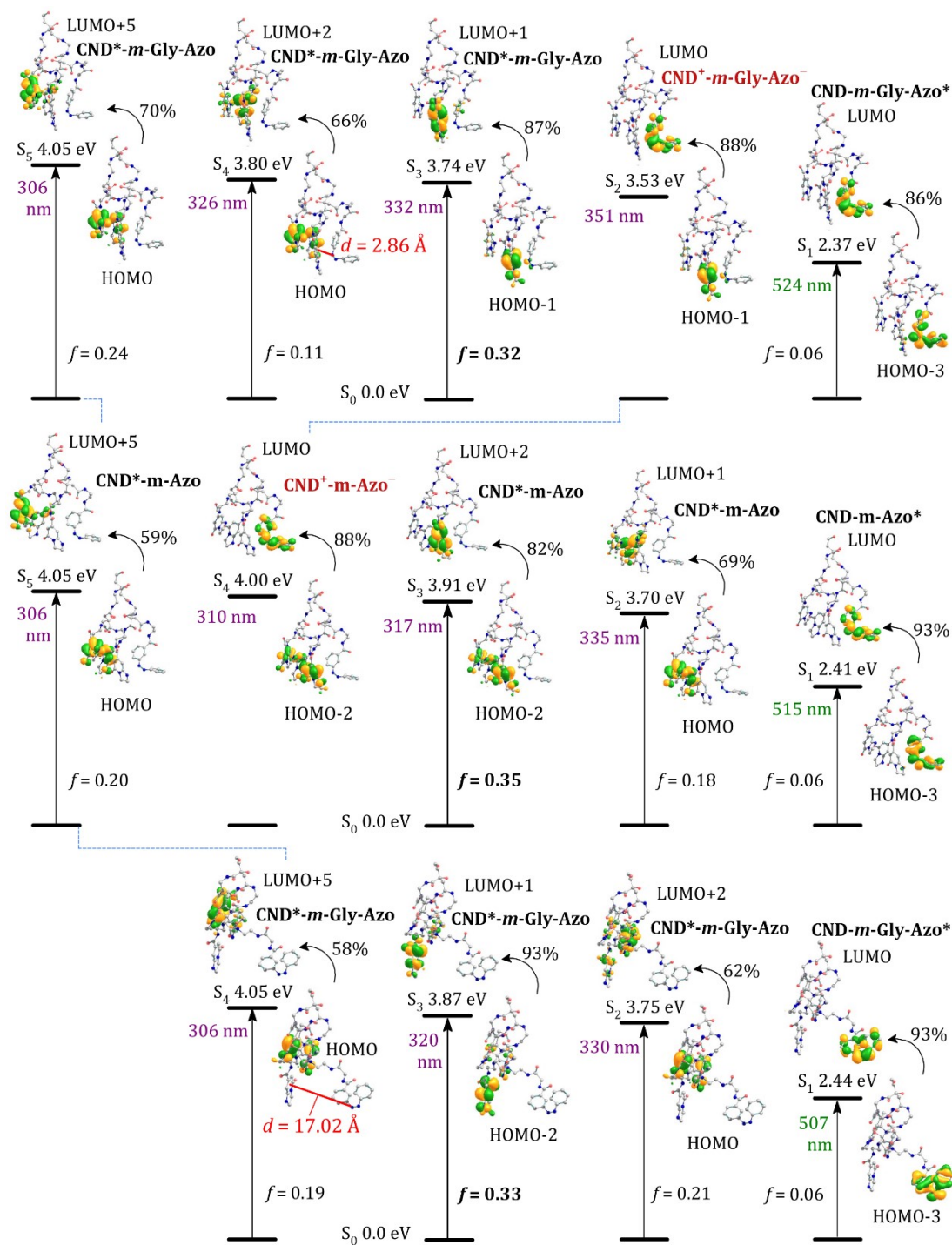


Figure S35. Lowest-energy electronic transitions in **CND-*m*-Azo** (*middle*) compared with **CND-*m*-Gly-Azo**. The hybrids incorporate the *cis* isomer of the azobenzene fragment, positioned either closer to (*top*) or farther from (*bottom*) the nearest IPCA centroid of the **CND** fragment.

Benchmarking Basis Sets and Functional

We performed a benchmarking considering different basis sets and different functional. For the basis set, we consider the wB97xD functional and apart from the original Pople's 6-31G(d), we consider a corresponsive cc-PVDZ and the more accurate cc-PVTZ basis sets. The absorption spectra are reported in **Figure S36**(left). From the spectra, we can conclude that there is little or no dependence on the used basis set. Next, we consider three different long-range corrected functionals (keeping the same cc-pVDZ basis set), which are essential to capture the van der Waals interactions present in the system. Apart from the wB97xD used throughout the study, we considered the HSE, CAM-B3LYP and HPBE functionals. As reported in **Figure S36**(right), there is a strong dependence of the absorption spectra on the used functional. While wB97xD and CAM-B3LYP leads to the same results, HSE tends to redshift the whole spectra, while HPBE blueshifts it. Comparing the obtained spectra with the experimental one (for the **CND-*p*-Azo**, reported in **Figure 4b** of the manuscript), we can exclude both HSE and HPBE, as their absorption is either too red or blue shifted compared to the experimental one. Thus, we can confirm that the wB97xD/6-31G(d) functional and basis set combination used is a good choice to reproduce the experimental spectra.

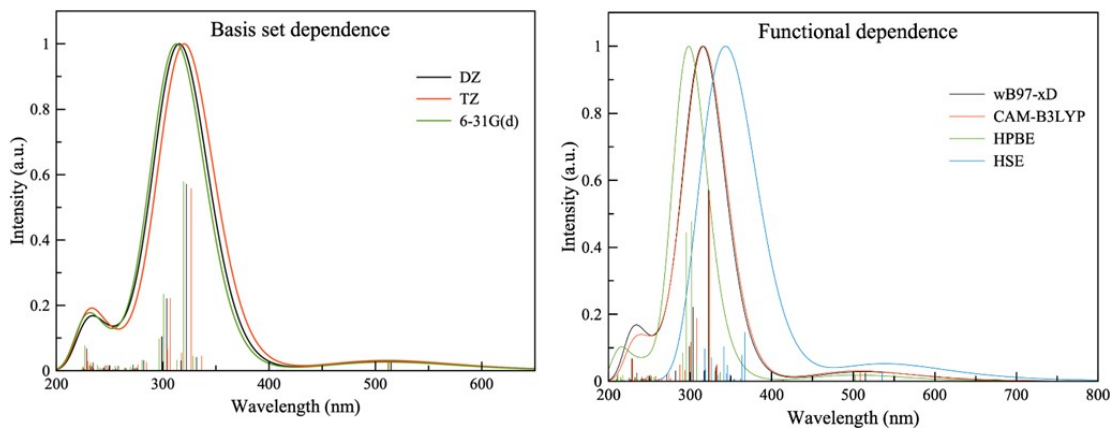


Figure S36. Absorption spectra of the CND-*p*-Azo obtained from computation while benchmarking different basis sets (left) and functionals (right).

Excitation-emission maps

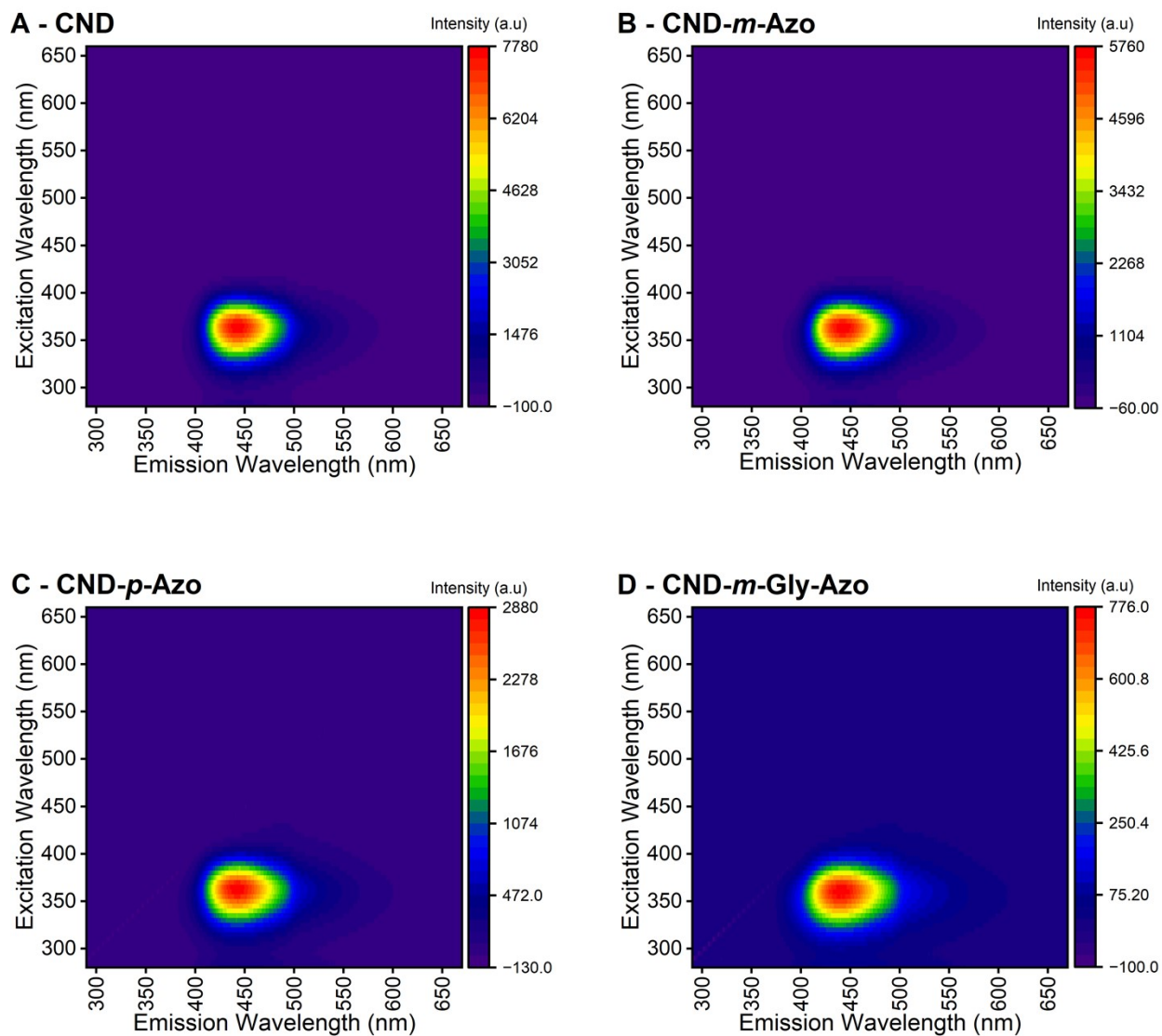


Figure S37. Excitation-emission maps recorded in an excitation wavelength range of 280 nm to 660 nm and an emission wavelength range of 290 nm to 670 nm. Concentration of $6 \text{ mg} \cdot \text{L}^{-1}$ in DMSO was used. (A) CND (B) CND-*m*-Azo (C) CND-*p*-Azo (D) CND-*m*-Gly-Azo.

Excitation Spectra

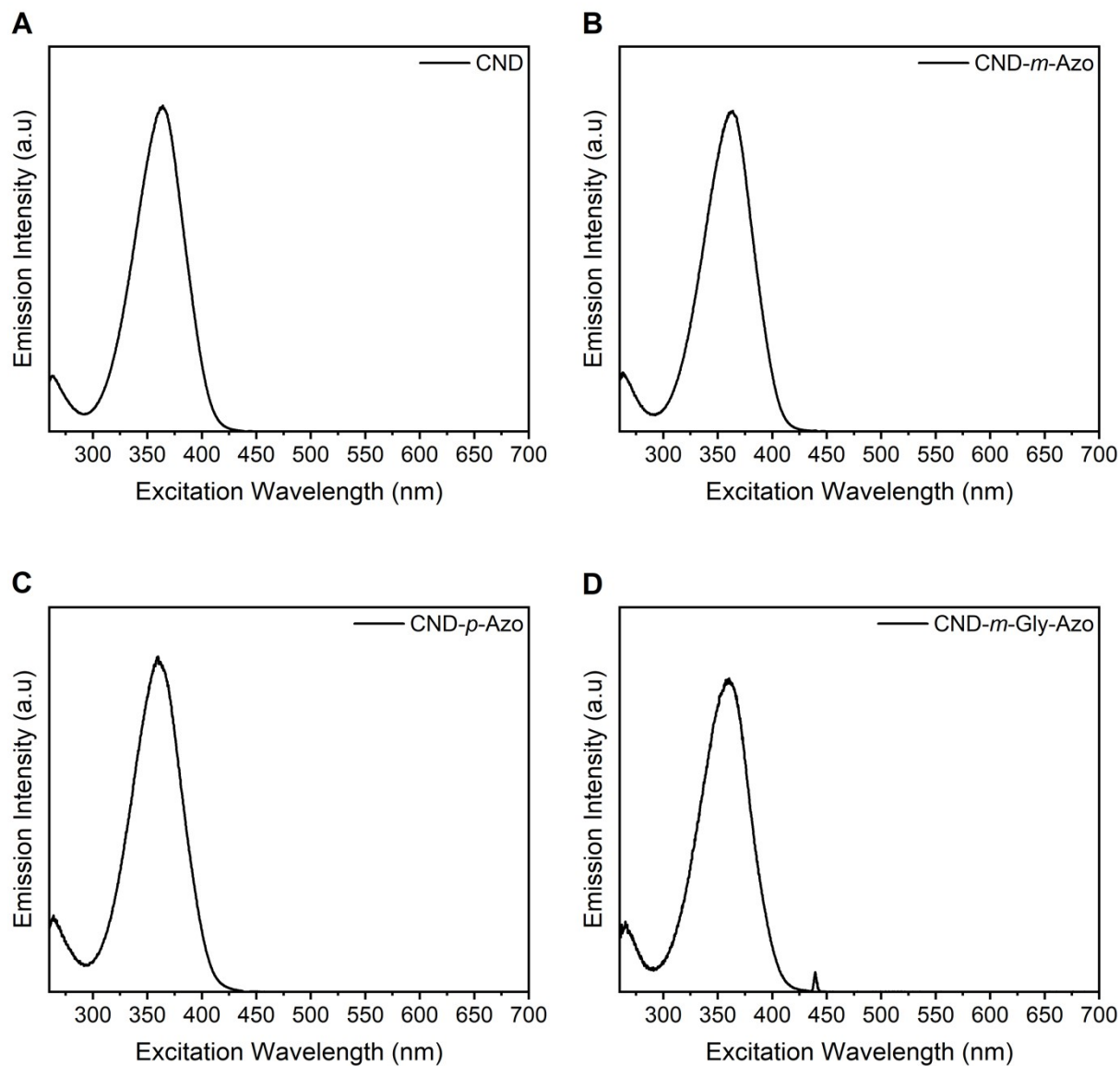


Figure S38. Excitation spectra recorded at an emission wavelength of 440 nm in the excitation wavelength range of 260 nm to 700 nm. Concentration of $6 \text{ mg} \cdot \text{L}^{-1}$ in DMSO was used. (A) CND (B) CND-*m*-Azo (C) CND-*p*-Azo (D) CND-*m*-Gly-Azo (the signal at 440 nm corresponds to the excitation wavelength which was not effectively subtracted from the background).

Time-Correlated Single Photon Counting (TCSPC)

For the determination of the fluorescence lifetimes, a homebuilt TCSPC setup was used. The excitation wavelength is generated with a tunable optical parametric amplifier (Orpheus-HP, Light Conversion) which is pumped by a 2 MHz carbide laser (CB3-40 W, Light Conversion). The excitation beam is tightly focused into the sample cuvette with a 75 mm lens and perpendicular to the excitation pathway, the fluorescence is collected by a second 75 mm lens. After separation from the excitation beam with a bandpass filter, the fluorescence was focused into a detector (PMA Hybrid 07, Picoquant) which is together with the laser's own trigger output connected to a time-tagging electronic (PicoHarp 330, Picoquant) for TCSPC measurements.

All samples were set to an optical density below 0.1 OD to prevent reabsorption effects. Since we were interested in the quenching efficiencies, an excitation wavelength of 385 nm was chosen, where predominantly the CND absorbs in the case of the hybrid systems. The obtained decay curves (see **Figure 6**) were analyzed using gaussian deconvolution in a commercial program (Fluofit, Picoquant). Each transient curve was fitted with three lifetimes (see **Table S3**).

Table S3. Obtained lifetimes τ and their respective amplitudes A from the fits of the TCSPC transients for the pure CND and the different hybrid systems. The average lifetime τ_{av} was used to calculate the quenching efficiencies and X^2 describes the goodness of the fit.

Sample	τ_1 [ns]	A_1 [counts]	τ_2 [ns]	A_2 [counts]	τ_3 [ns]	A_3 [counts]	τ_{av} [ns]	X^2 (red)
CND	0.52	28160	4.75	17596	11.25	28972	5.70	1.255
CND- <i>p</i> -Azo	0.37	41900	4.10	19085	10.92	16888	3.45	1.843
CND- <i>m</i> -Azo	0.40	43300	3.76	18453	10.53	17936	3.60	1.236
CND- <i>m</i> -Gly-Azo	0.37	50990	3.05	17545	10.70	9193	2.24	2.976

Determination of Transfer Rates and Emission Quenching Efficiencies

The three lifetimes were used to determine an amplitude-weighted average lifetime τ_{av} . This average lifetime was used to calculate the total emission quenching efficiencies according to following formula,

$$E_T(\tau) = 1 - \frac{\tau_{AzoCND}}{\tau_{CND}}$$

where τ_{AzoCND} and τ_{CND} are the average fluorescence lifetimes of the hybrid systems and pure CND, respectively.

Additionally, with the same formula, the total emission quenching efficiencies were calculated using the photoluminescence quantum yields (from **Table 2** of the main manuscript) instead of the fluorescence lifetimes. The results from both calculations are presented in the following **Table S4**.

Table S4. The energy transfer efficiencies $E_T(F)$ and $E_T(\tau)$ calculated by the photoluminescence quantum yield and fluorescence lifetimes, respectively. The radiative k_r and non-radiative k_{nr}

Construct	ϕ_F	$E_T(F)$ [%]	τ_{av} [ns]	$E_T(\tau)$ [%]	k_r [10^8 s^{-1}]	k_{nr} [10^8 s^{-1}]
CND	0.37	---	5.70	---	0.65	1.11
CND-<i>m</i>-Azo	0.18	51	3.60	39	0.50	2.27
CND-<i>p</i>-Azo	0.11	70	3.45	36	0.32	2.58
CND-<i>m</i>-Gly-Azo	0.01	97	2.24	61	0.045	4.42

constants are also provided.

Interestingly, the emission quenching efficiencies derived from fluorescence lifetimes, $E_T(\tau)$, are significantly lower than those obtained from fluorescence quantum yields, $E_T(F)$. This discrepancy arises from fundamental differences between the measurement methods. In TCSPC measurements, only the emissive state is detected, meaning that emitted photons are counted while non-emissive (dark) states remain hidden. As a result, this creates a bias, making the emissive state appear more dominant than it actually is.

Furthermore, we determined FRET parameters according to the program³⁹ and publication⁴⁰ by Peter Nagy, which are based on the commonly used FRET equations such as the one for the overlap integral J :

$$J = \int F_D(\lambda) \cdot \varepsilon_A(\lambda) \cdot \lambda^4 d\lambda$$

where $F_D(\lambda)$ represents the fluorescence spectrum of the donor, normalized to an area of 1, $\varepsilon_A(\lambda)$ is the extinction coefficient of the acceptor and λ^4 serves as a wavelength correction factor.

Using the calculated overlap integral J , along with the orientation factor κ^2 , the photoluminescence quantum yield of the donor ϕ_D and the refractive index n , we determined the Förster radius R_0 .

$$R_0 = \text{const.} \cdot \sqrt[6]{J \cdot \kappa^2 \cdot \phi_D \cdot n^{-4}}$$

It should be noted that no clear value could be determined for κ^2 due to the unknown distribution of the azo moieties on the CND surface. Thus, an average value of 2/3 was assumed for the orientation factor. With R_0 , the transfer efficiency E_{FRET} can be estimated for the actual distances R (given in **Table 3** of the main manuscript) between the CND and the azo moieties:

$$E_{\text{FRET}} = \frac{R_0^6}{R_0^6 + R^6}$$

Additionally, if the excited-state lifetime of the donor τ_D is known, the transfer rate k_T can be determined using following relationship.

$$k_T = \frac{1}{\tau_D} \cdot \left(\frac{R_0}{r}\right)^6$$

Table S5. Calculated FRET parameters including the overlap integrals J , the Förster radii R_0 , the FRET efficiencies E_{FRET} , the transfer rates k_T and the transfer lifetimes τ_T .

Construct	J	R_0 [nm]	E_{FRET} [%]	k_T [s ⁻¹]	τ_T [fs]
CND-p-Azo	2.96*10 ¹³	2.25	99.9	1.76*10 ¹³	56
CND-m-Azo	1.88*10 ¹³	2.09	99.9	9.47*10 ¹²	105
CND-Gly-m-Azo	1.28*10 ¹³	1.96	99.9	6.44*10 ¹²	155

As discussed in the main manuscript, these high efficiencies are not representative of all three hybrids. Only **CND-m-Gly-Azo** exhibits such a high emission quenching efficiency based on photoluminescence quantum yield measurements. The primary reason for this discrepancy is that the calculated distances and the averaged orientation factor may not be uniformly valid across the entire **CND** surface. The variations in the azo moiety distribution on the surface are not accounted for in the calculations, which could likely contribute to the observed differences.

Photo-Switching

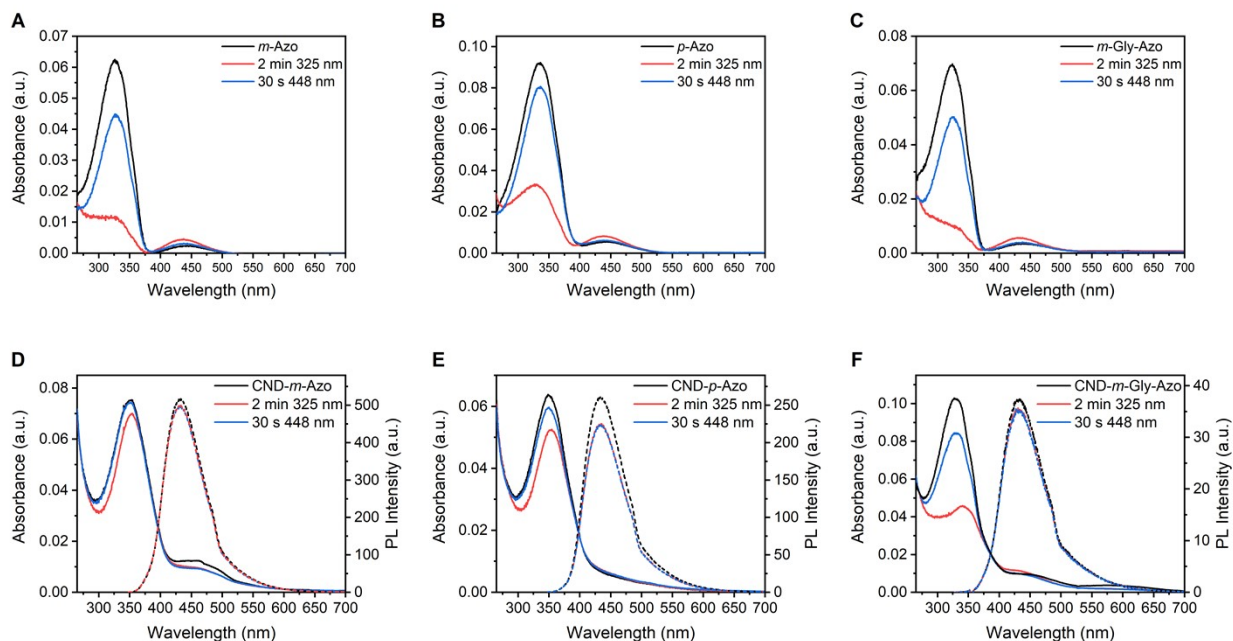


Figure S39. Absorption spectra of the (A) *m*-Azo, (B) *p*-Azo, and (C) *m*-Gly-Azo, as well as the absorption and emission spectra of the (D) CND-*m*-Azo, (E) CND-*p*-Azo, and (F) CND-*m*-Gly-Azo, were measured before and after light irradiation. The initial state (black, black dotted) was measured prior to illumination. The first illumination was conducted with a 325 nm LED for a duration of two minutes (red, red dotted). The second illumination was conducted with a 448 nm LED for a duration of 30 seconds. The measurements were performed with $5 \mu\text{mol L}^{-1}$ solutions of the respective azo in DMSO at 25 °C. The measurements were performed with 10 mg L^{-1} dispersions of the respective hybrid in DMSO at 25 °C.

Fatigue Resistance

To ensure that the photostationary state (PSS) was reached during the fatigue resistance measurements, different times were tested with the 340 nm and 450 nm LEDs (see **Figure S40**). Based on this, five minutes was chosen. This was to ensure that the hybrids would also have enough time to reach the PSS.

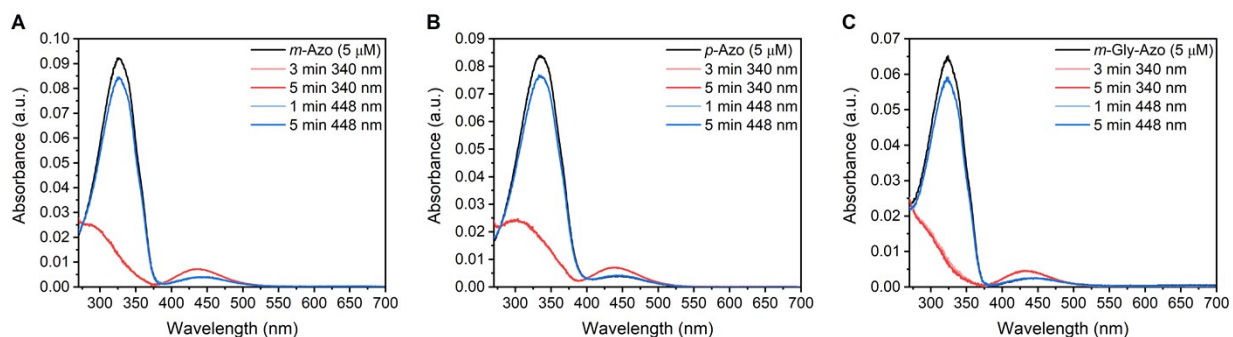


Figure S40. First, the non-irradiated samples were irradiated at 340 nm for three minutes and then for a further two minutes to check whether the PSS of the *Z* isomer had been reached. The samples were then irradiated at 450 nm for one minute and then for a further four minutes to check whether the PSS for the *E* isomer had also been reached. For the three pristine azos: (A) *m*-Azo (B) *p*-Azo (C) *m*-Gly-Azo. The measurements were performed with 5 $\mu\text{mol L}^{-1}$ solutions of the respective azo in DMSO at 25 $^{\circ}\text{C}$.

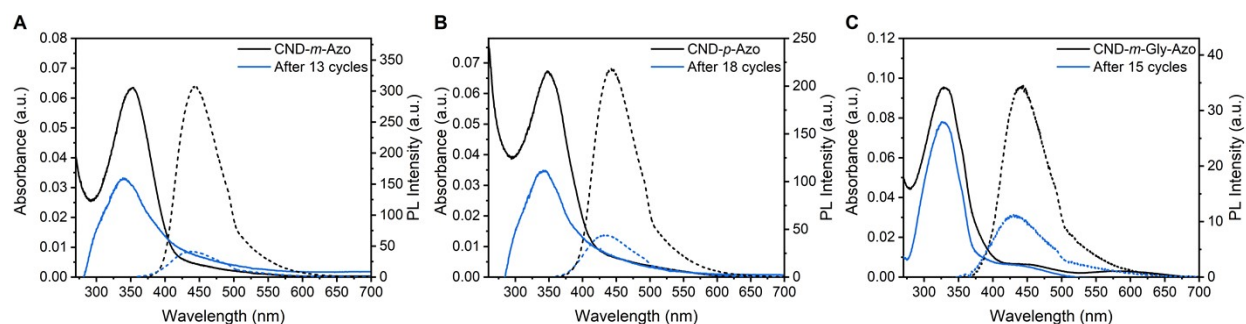


Figure S41. Absorbance and emission of the (A) CND-*m*-Azo (B) CND-*p*-Azo and (C) CND-*m*-Gly-Azo before and after several cycles of light irradiation. One cycle consisted of five minutes of illumination with a 340 nm LED and five minutes of illumination with a 448 nm LED. The measurements were performed with 10 mg L⁻¹ dispersions of the respective hybrid in DMSO at 25 °C.

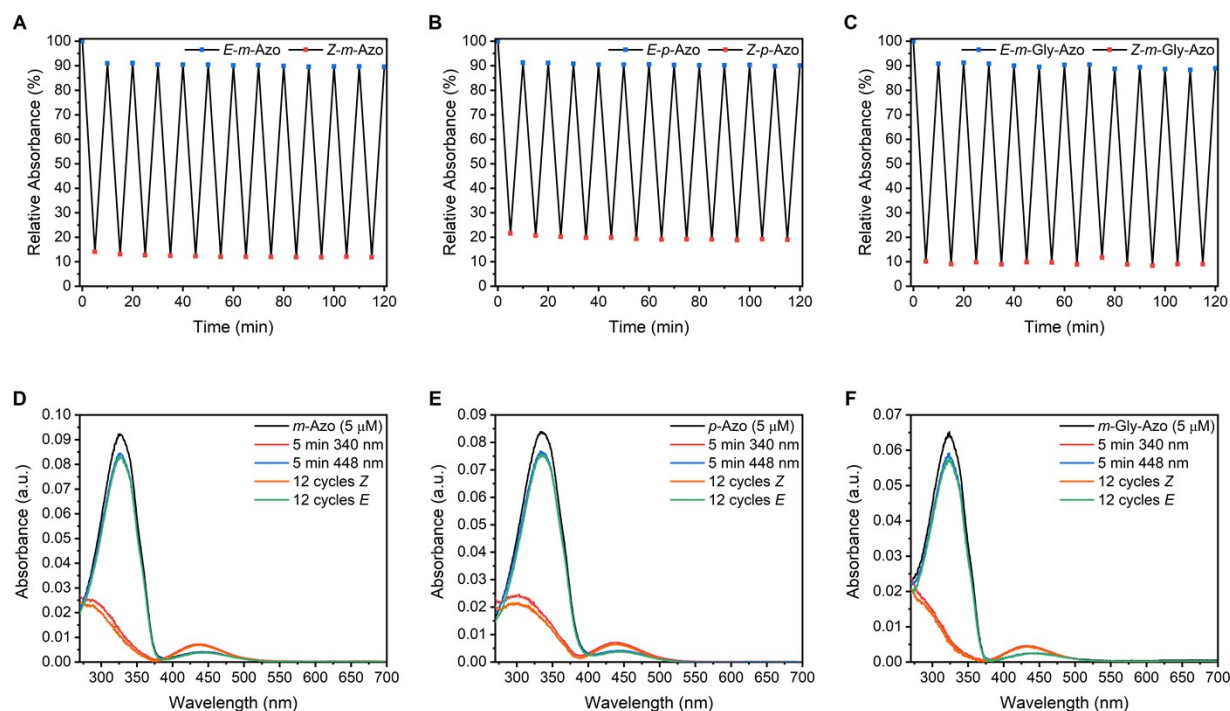


Figure S42. (A) The relative absorption intensity of *m*-Azo at 326 nm was not found to decrease significantly over time. (B) The relative absorption intensity of *p*-Azo at 335 nm was not found to

decrease significantly over time. (C) The relative absorption intensity of ***m*-Gly-Azo** at 323 nm was not found to decrease significantly over time. Absorbance of the (D) ***m*-Azo** (E) ***p*-Azo** and (F) ***m*-Gly-Azo** before and after 12 cycles of light irradiation for each isomer. One cycle consisted of five minutes of illumination with a 340 nm LED and five minutes of illumination with a 448 nm LED. The measurements were performed with 5 $\mu\text{mol L}^{-1}$ solutions of the respective azo in DMSO at 25 °C.

Kinetic Measurements

Kinetic experiments were done following an already published approach.⁴¹

For the kinetic measurements of the *cis* (*Z*) to *trans* (*E*) isomerization, samples were irradiated with an appropriate wavelength at 40 °C. A spectrum was recorded for each sample every 30 min from 290 nm to 700 nm. Due to scattering likely caused by agglomeration of the hybrids, **CND-*m*-Azo** and **CND-*p*-Azo** were normalized to their isosbestic points at 363 nm and 397 nm respectively. The azo loading on **CND-*m*-Gly-Azo** was high enough to abstain from this spectra processing. We want to highlight here that the obtained half-lives are flawed due to agglomeration, spectra processing and the handling of a multi-switch particle as a first order kinetic system. Nevertheless, it demonstrates the photoswitch properties and displays the general trend of the thermal properties. **Figures S46-S47** show spectra of **CND-*m*-Azo** and **CND-*p*-Azo** normalized to the isosbestic point for as accurate of an analysis as possible, while **Figures S49** show the raw spectra. **Figures S48** presents the unprocessed spectra of **CND-*m*-Gly-Azo** and the respective analysis. A low concentration was intentionally used to minimize aggregation effects. Three samples of each compound were measured.

All half-lives and rate constant were determined by a triple determination. Their calculation was conducted with OriginPro® by the OriginLab Corporation. For this procedure, the absorption at a certain wavelength was plotted against the time elapsed after irradiation. The measured points were fitted with the following exponential decay function 1 in Origin (Equation 5).

$$y = y_0 + A_1 e^{-x/t_1} \quad (5)$$

The exponential time constant t_1 obtained by this fitting was further used to calculate the kinetic constant k by Equation 6 and the half-life $t_{1/2}$ by Equation 7.

$$k = 1/t_1 \quad (6)$$

$$t_{1/2} = t_1 \times \ln\left(\frac{I_0}{I}\right) (2) \quad (7)$$

As the hybrid materials contain more than a single azobenzene, we measured their t_{obs} following the same procedure as for the pristine azobenzenes.

Table S6. Half-lives at 40 °C for the pristine azos, as well as for the azo-hybrids.

Compound	$t_{1/2}$ or t_{obs} in h / Exp 1	$t_{1/2}$ or t_{obs} in h / Exp 2	$t_{1/2}$ or t_{obs} in h / Exp 3	Ø $t_{1/2}$ or t_{obs} in h	Standard deviation / h
<i>m</i>-Azo	31.3	30.9	31.3	31.2	0.2
CND-<i>m</i>-Azo	33	34	26	31	3
<i>p</i>-Azo	13.4	13.3	13.4	13.4	0.1
CND-<i>p</i>-Azo	15	15	16	15	1
<i>m</i>-Gly-Azo	34.7	35.2	34.6	34.8	0.3
CND-<i>m</i>-Gly-Azo	28	26	26	27	1

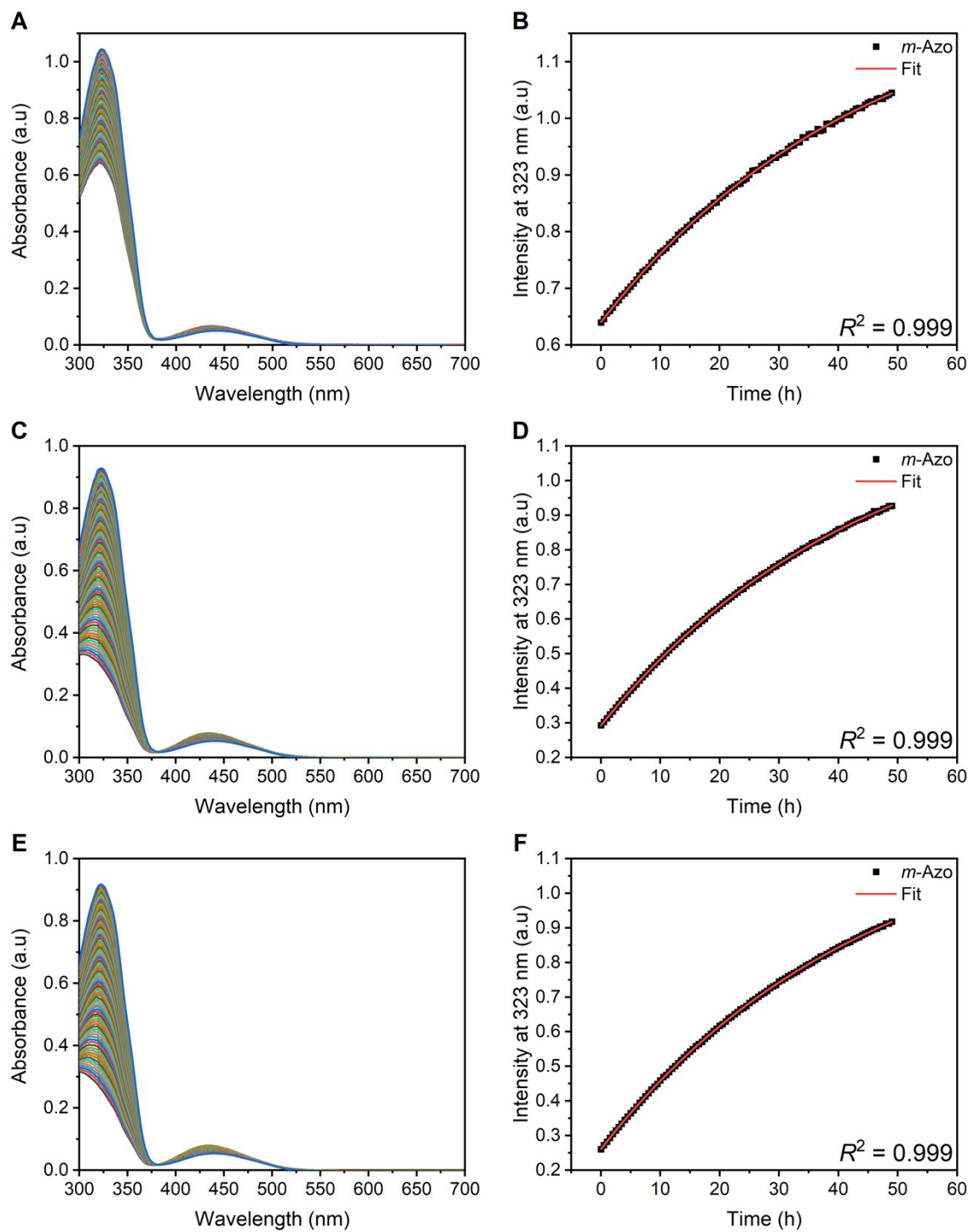


Figure S43. UV-vis spectra of thermal *Z*- to *E*-isomerization of *m*-Azo (A) first, (C) second, and (E) third measured in DMSO at 40 °C. (B), (D), and (F) single absorption wavelength at 323 nm plotted against time, with a single exponential fit to determine half-life.

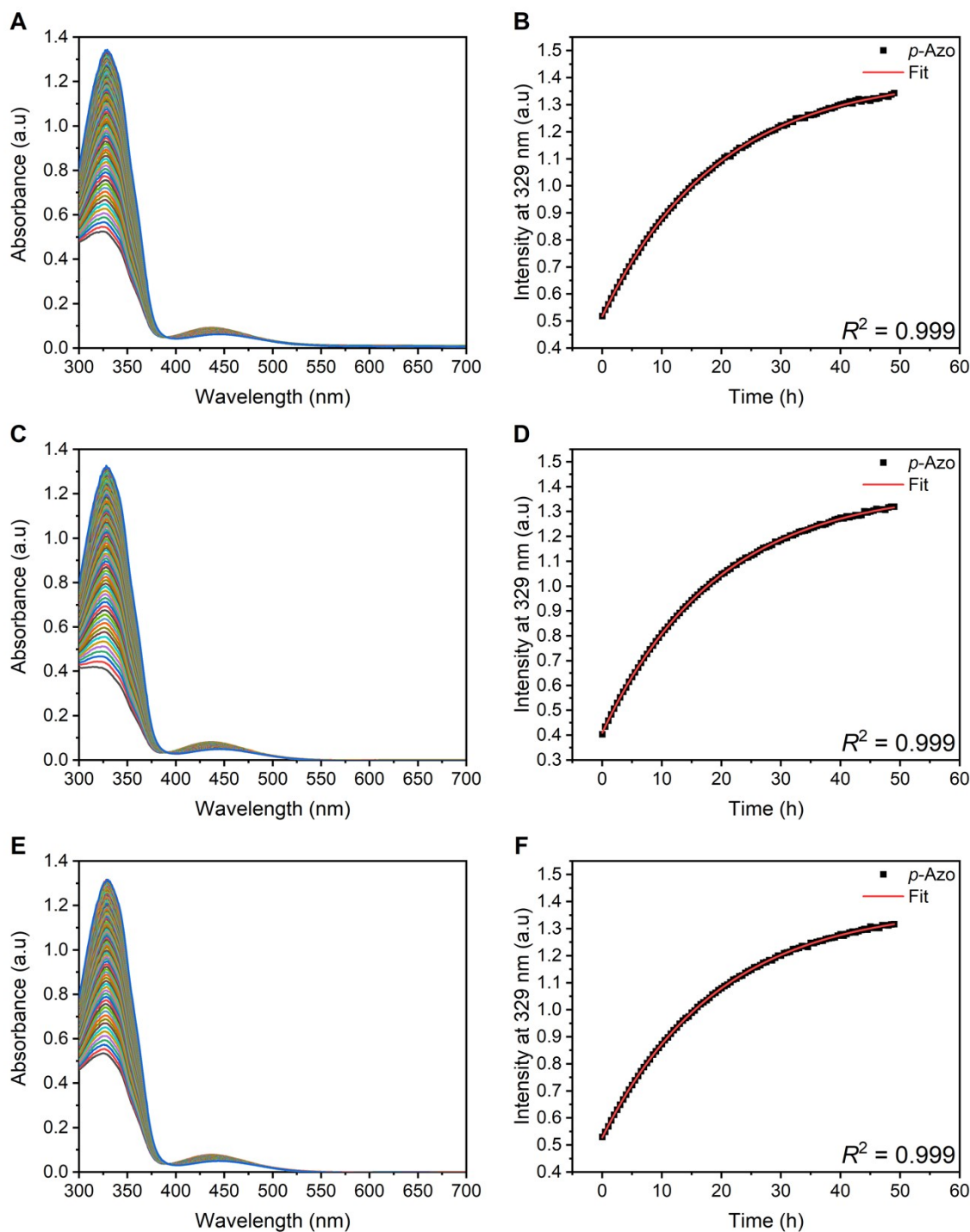


Figure S44. UV-vis spectra of thermal Z- to E-isomerization of *p*-Azo (A) first, (C) second, and (E) third measured in DMSO at 40 °C. (B), (D), and (F) single absorption wavelength at 329 nm plotted against time, with a single exponential fit to determine half-life.

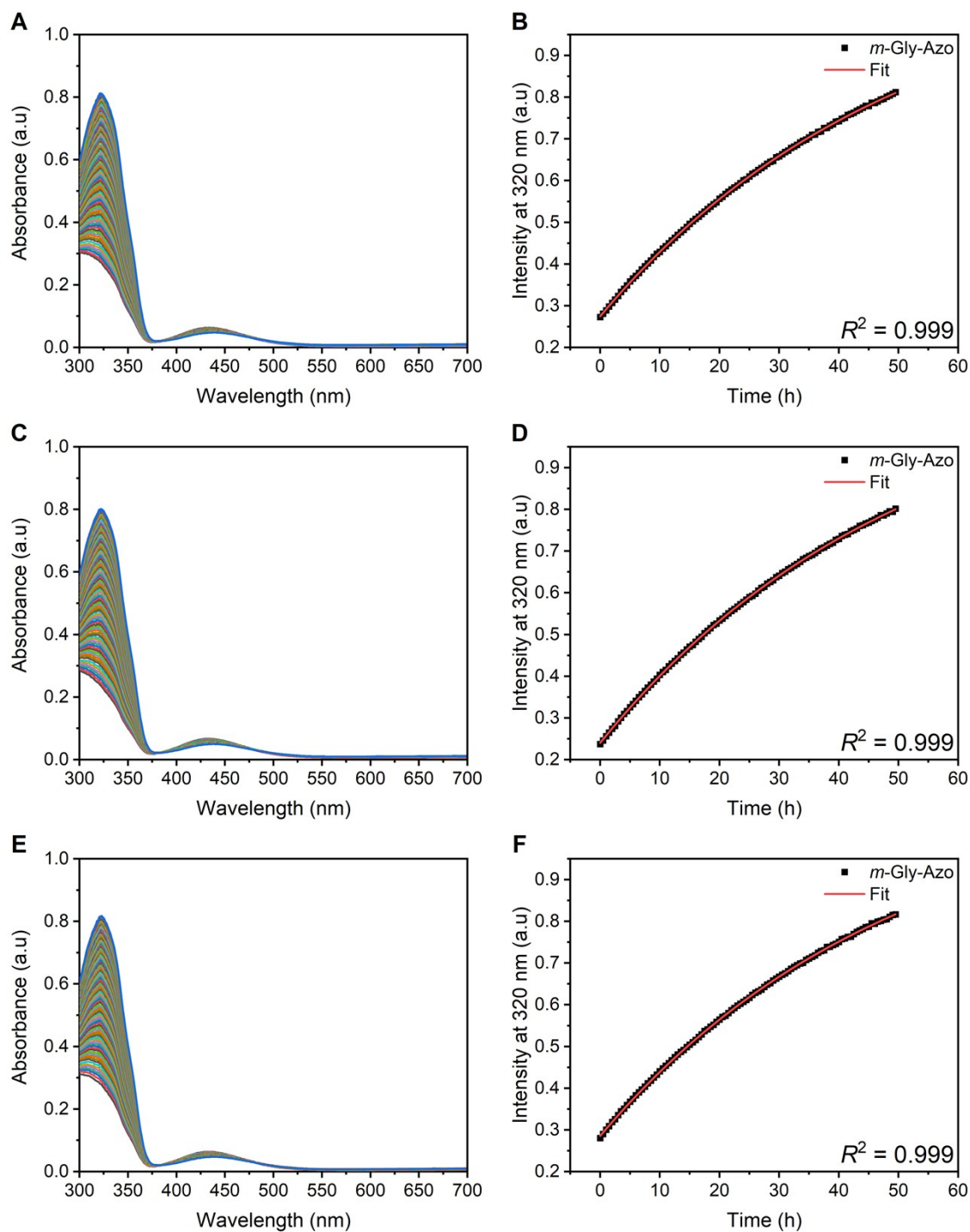


Figure S45. UV-vis spectra of thermal Z- to E-isomerization of *m*-Gly-Azo (A) first, (C) second, and (E) third measured in DMSO at 40 °C. (B), (D), and (F) single absorption wavelength at 320 nm plotted against time, with a single exponential fit to determine half-life.

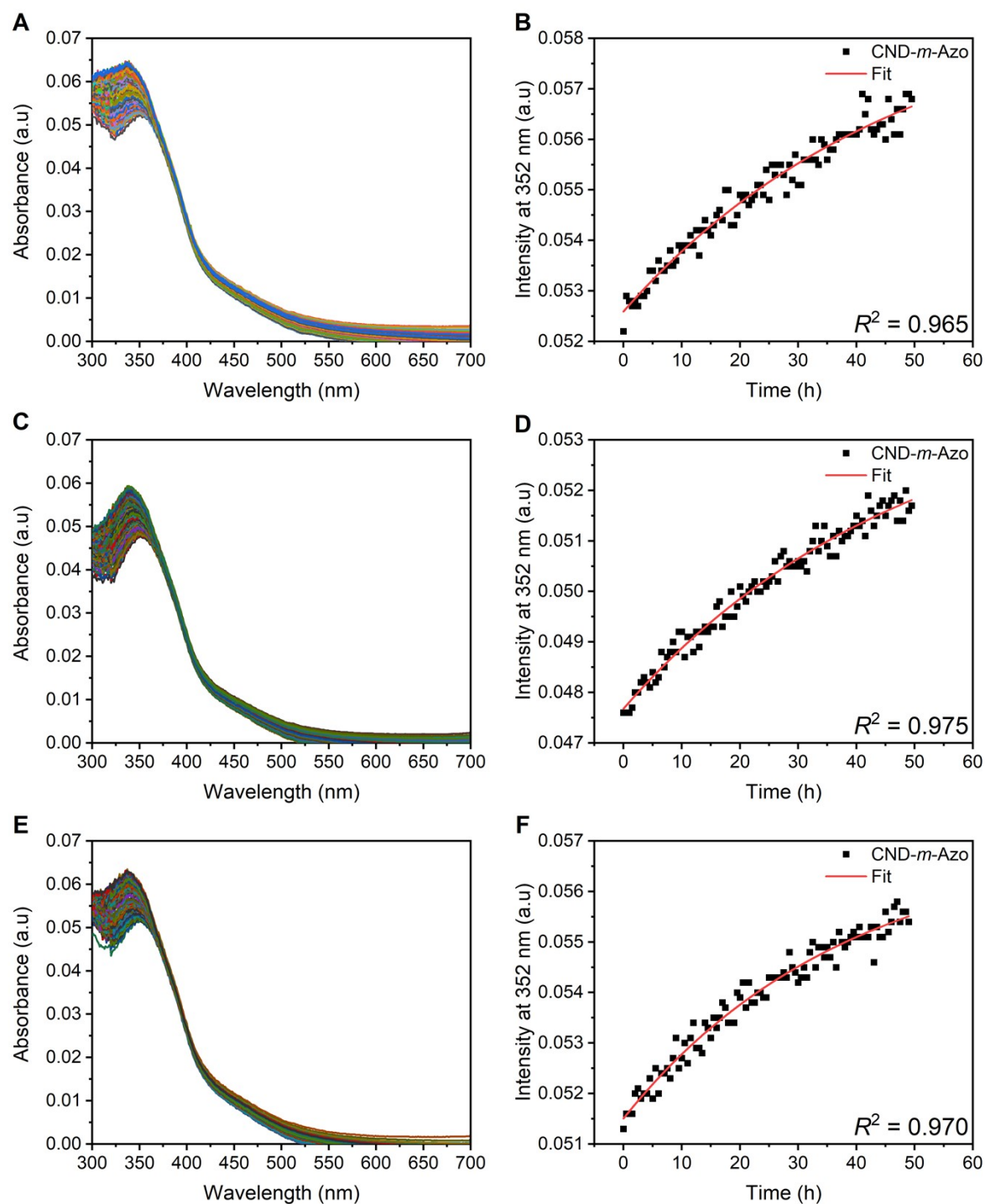


Figure S46. Normalized UV-vis spectra of thermal Z- to E-isomerization of CND-*m*-Azo (A) first, (C) second, and (E) third measured in DMSO at 40 °C. (B), (D), and (F) single absorption wavelength at 352 nm plotted against time, with a single exponential fit to determine half-life.

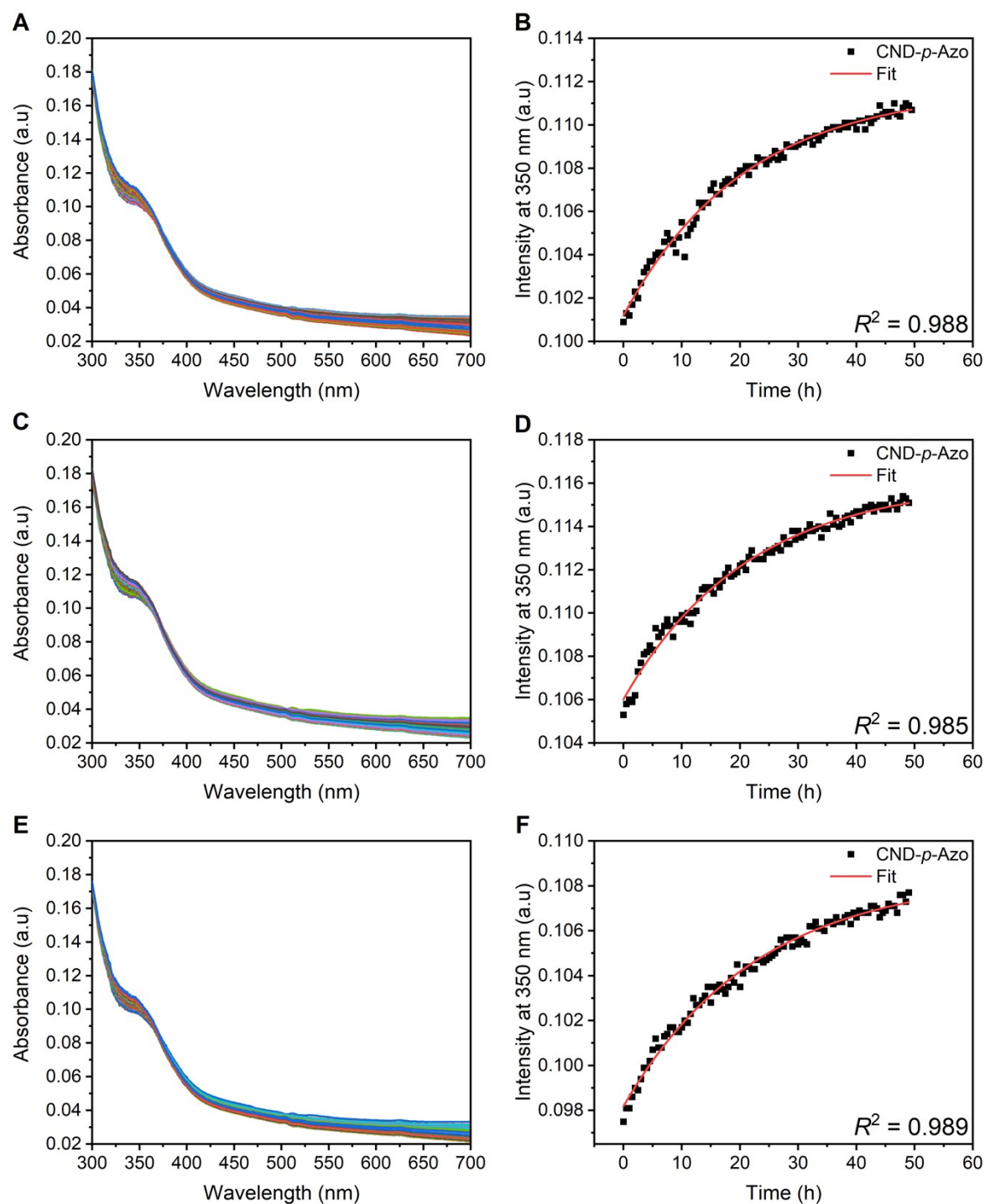


Figure S47. Normalized UV-vis spectra of thermal Z- to E-isomerization of CND-*p*-Azo (A) first, (C) second, and (E) third measured in DMSO at 40 °C. (B), (D), and (F) single absorption wavelength at 350 nm plotted against time, with a single exponential fit to determine half-life.

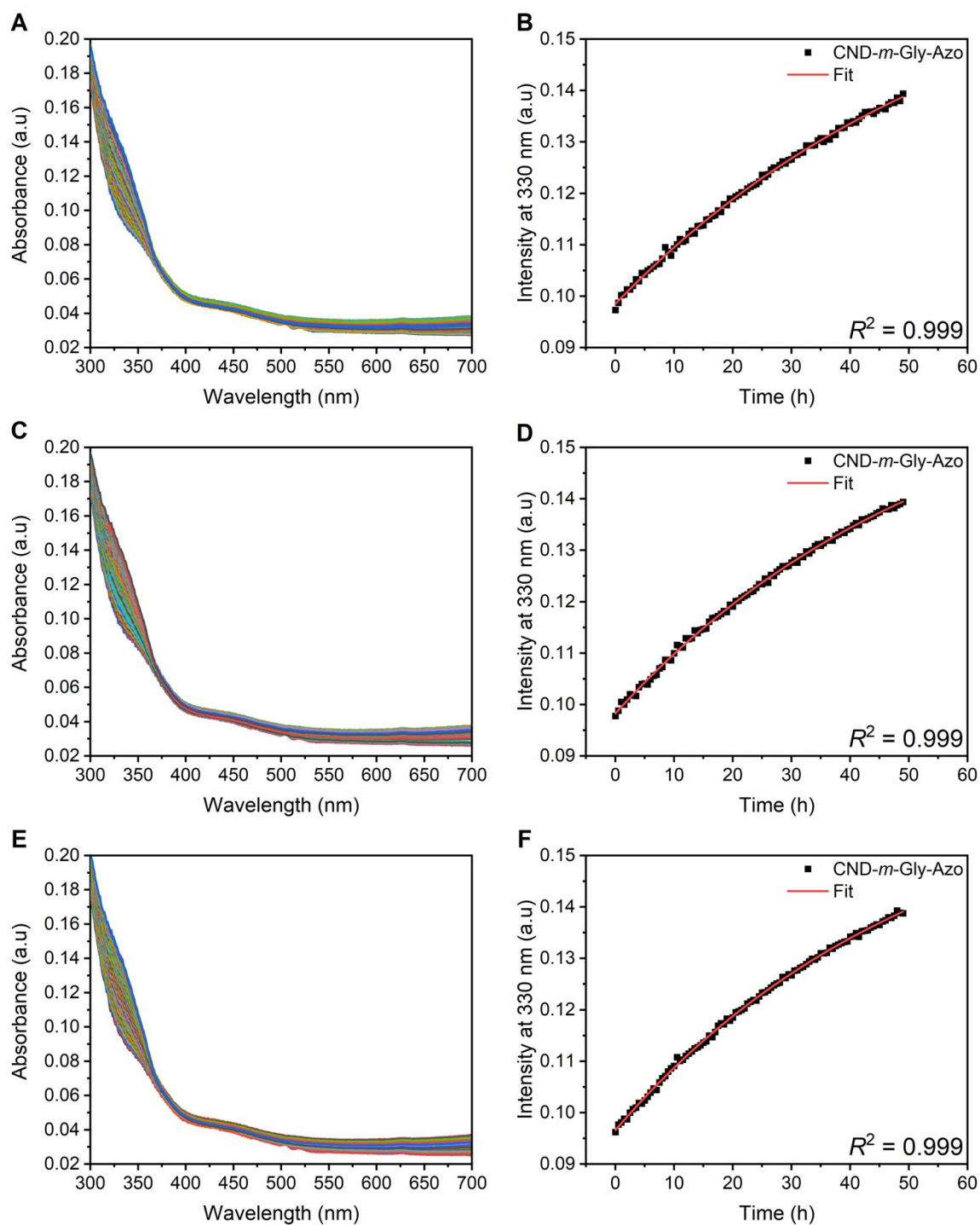


Figure S48. UV-vis spectra of thermal *Z*- to *E*-isomerization of CND-*m*-Gly-Azo (A) first, (C) second, and (E) third measured in DMSO at 40 °C. (B), (D), and (F) single absorption wavelength at 323 nm plotted against time, with a single exponential fit to determine half-life.

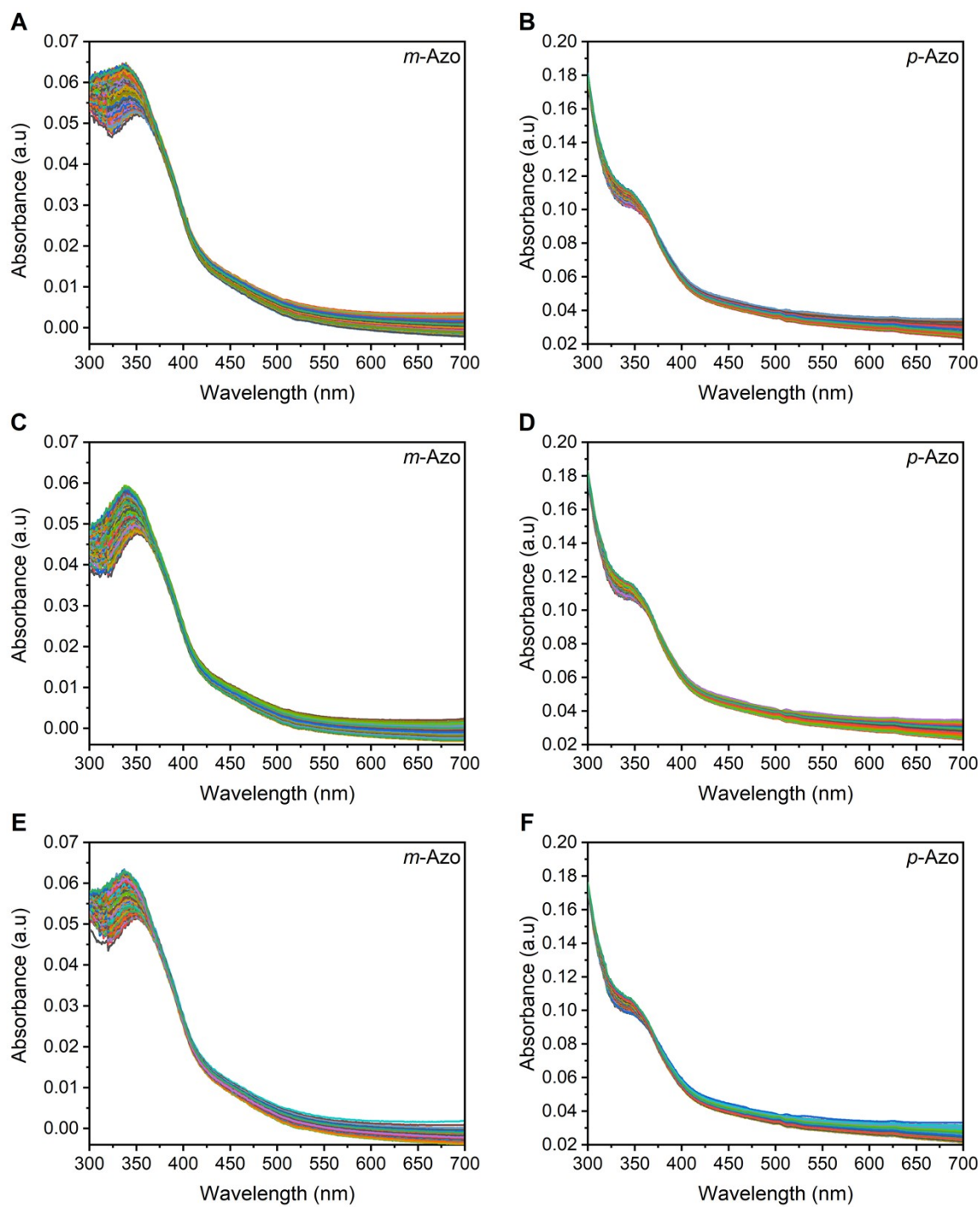


Figure S49. Non processed UV-vis spectra of thermal Z- to E-isomerization of **CND-*m*-Azo** (A) first, (C) second, and (E) third, and **CND-*p*-Azo** (B) first, (D) second, and (F) third were measured in DMSO at 40 °C.

NMR Spectra

CND

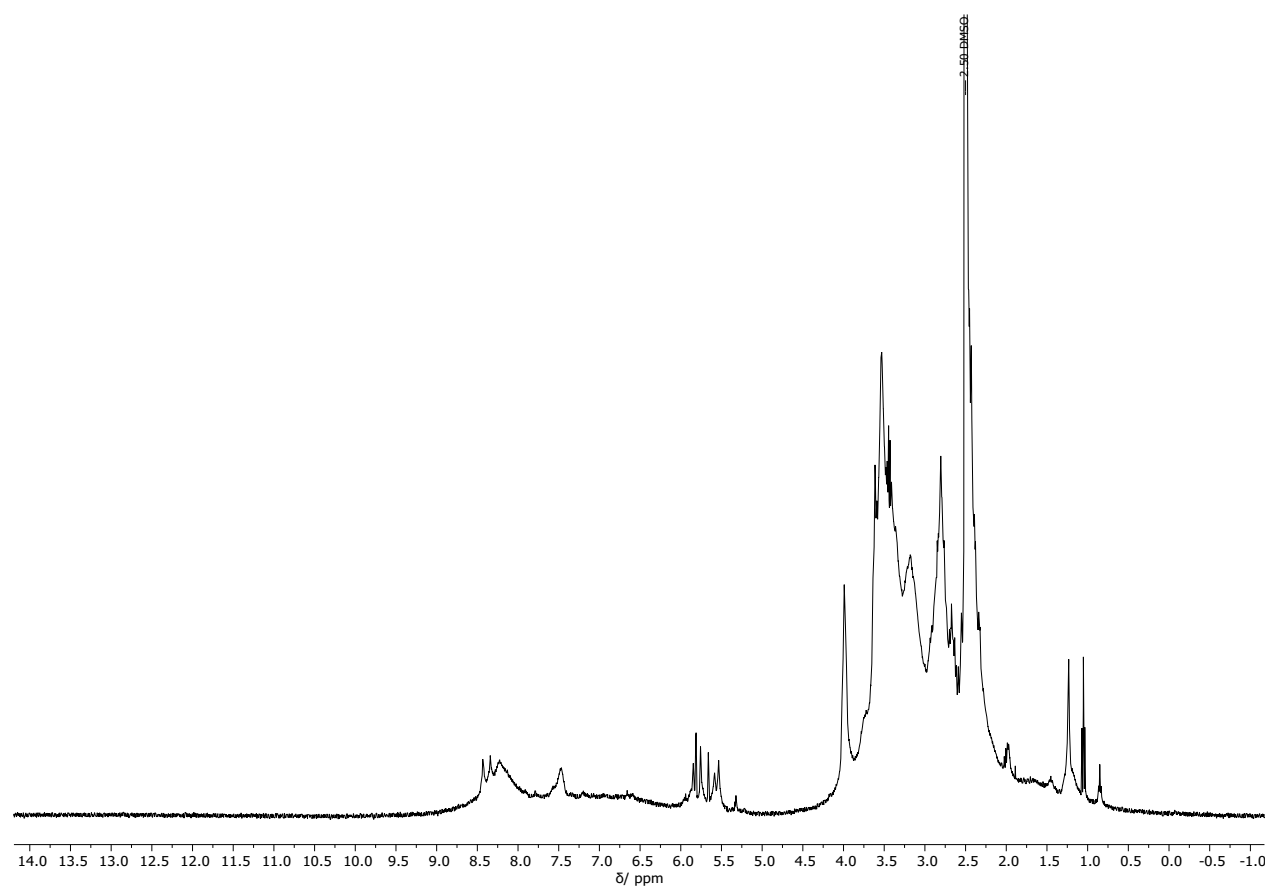


Figure S50. ^1H -NMR spectra of **CND** measured in DMSO- d_6 .

3-(Phenylazo)benzoic acid (*m*-Azo)

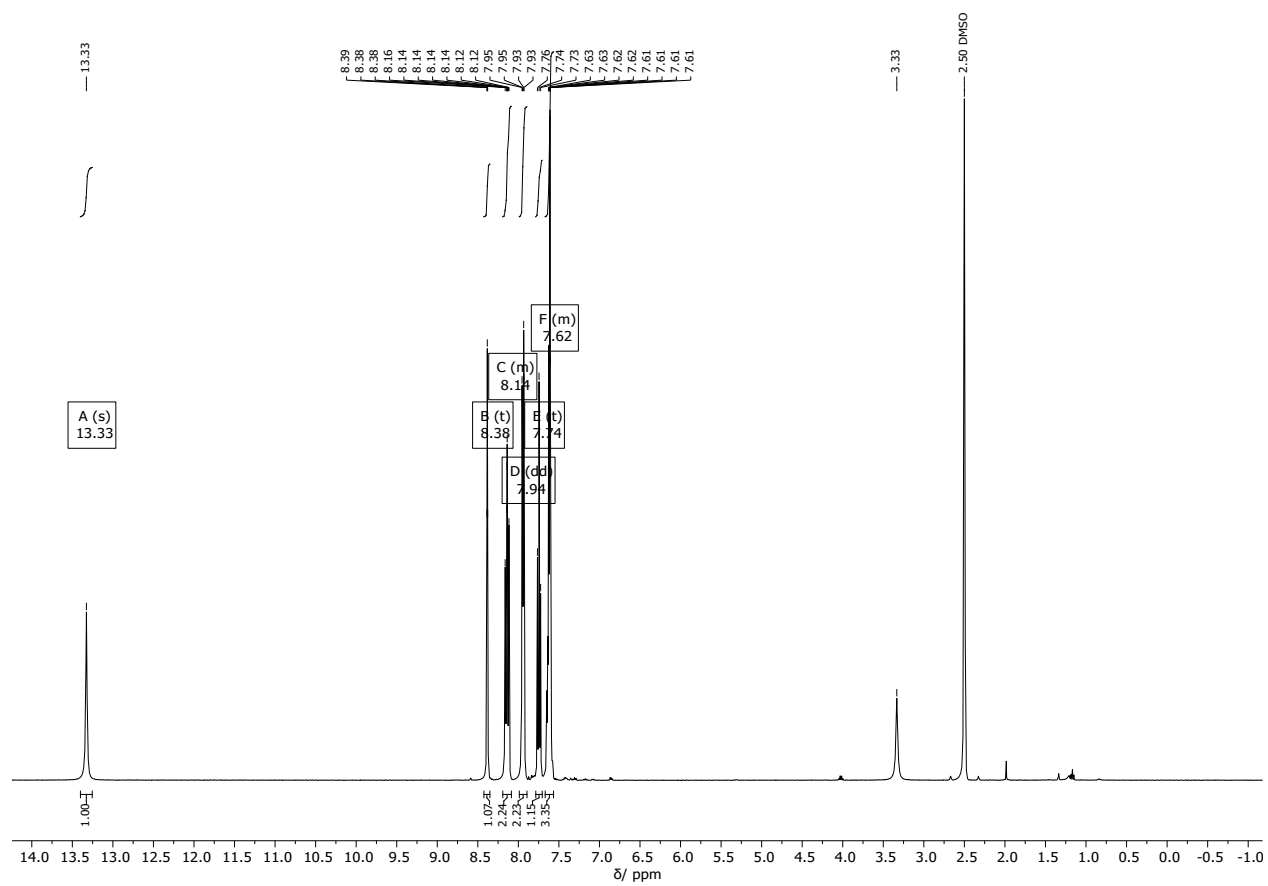


Figure S51. ^1H -NMR spectra of 3-(Phenylazo)benzoic acid (*m*-Azo) measured in DMSO- d_6 .

4-(Phenylazo)benzoic acid (*p*-Azo)

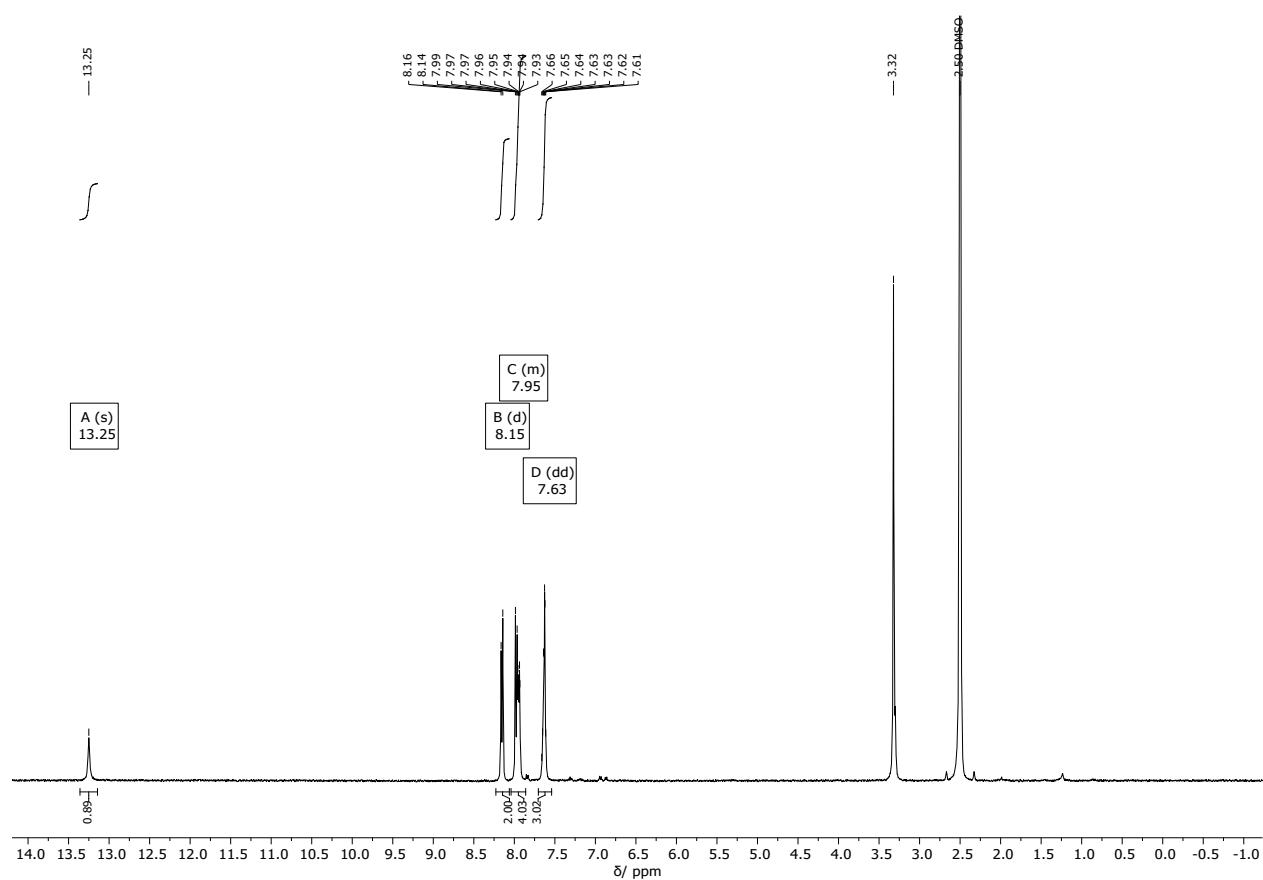


Figure S52. ¹H-NMR spectra of 4-(Phenylazo)benzoic acid (*p*-Azo) measured in DMSO-d₆.

***N*-[3-(phenylazo)benzoyl]glycine methyl ester**

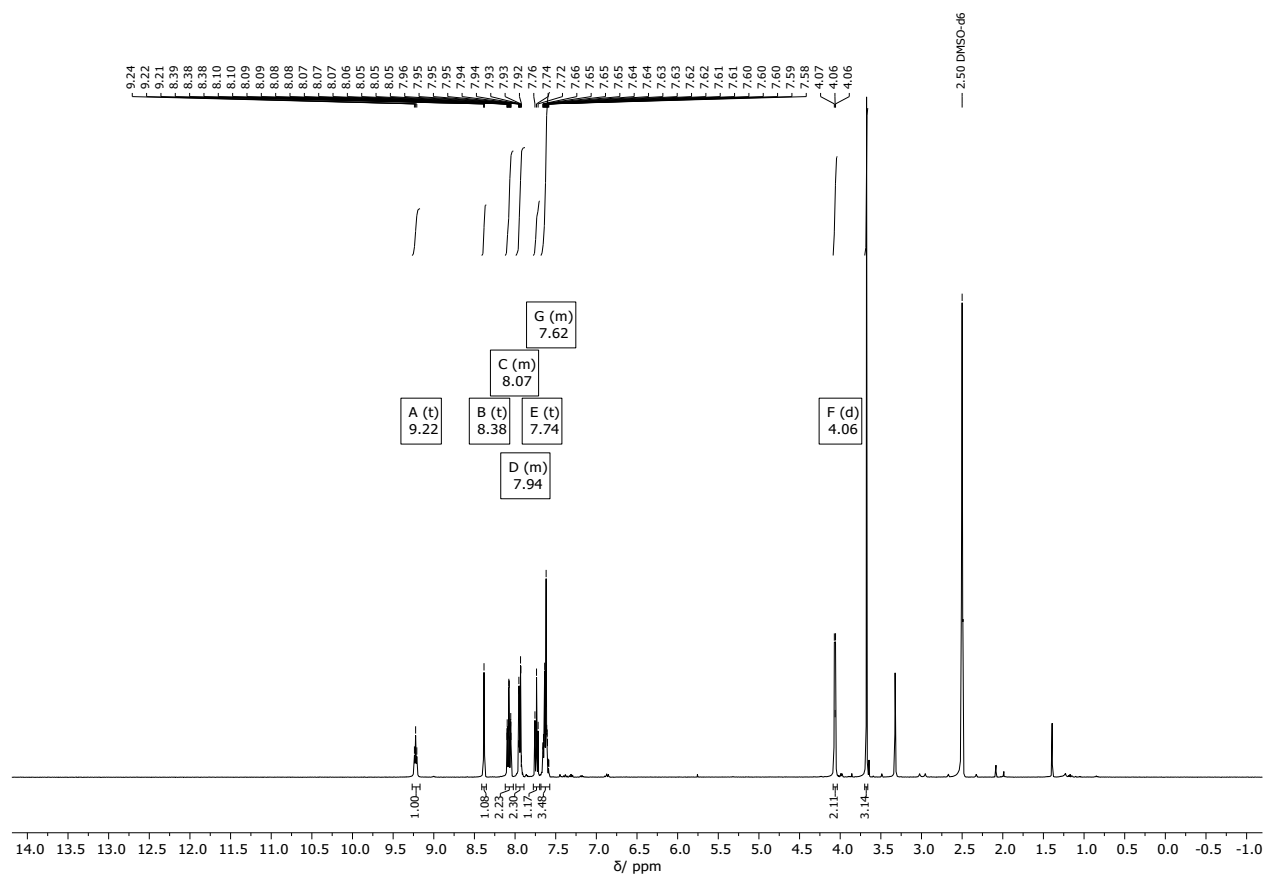


Figure S53. ^1H -NMR spectra of *N*-[3-(phenylazo)benzoyl]glycine methyl ester measured in DMSO- d_6 .

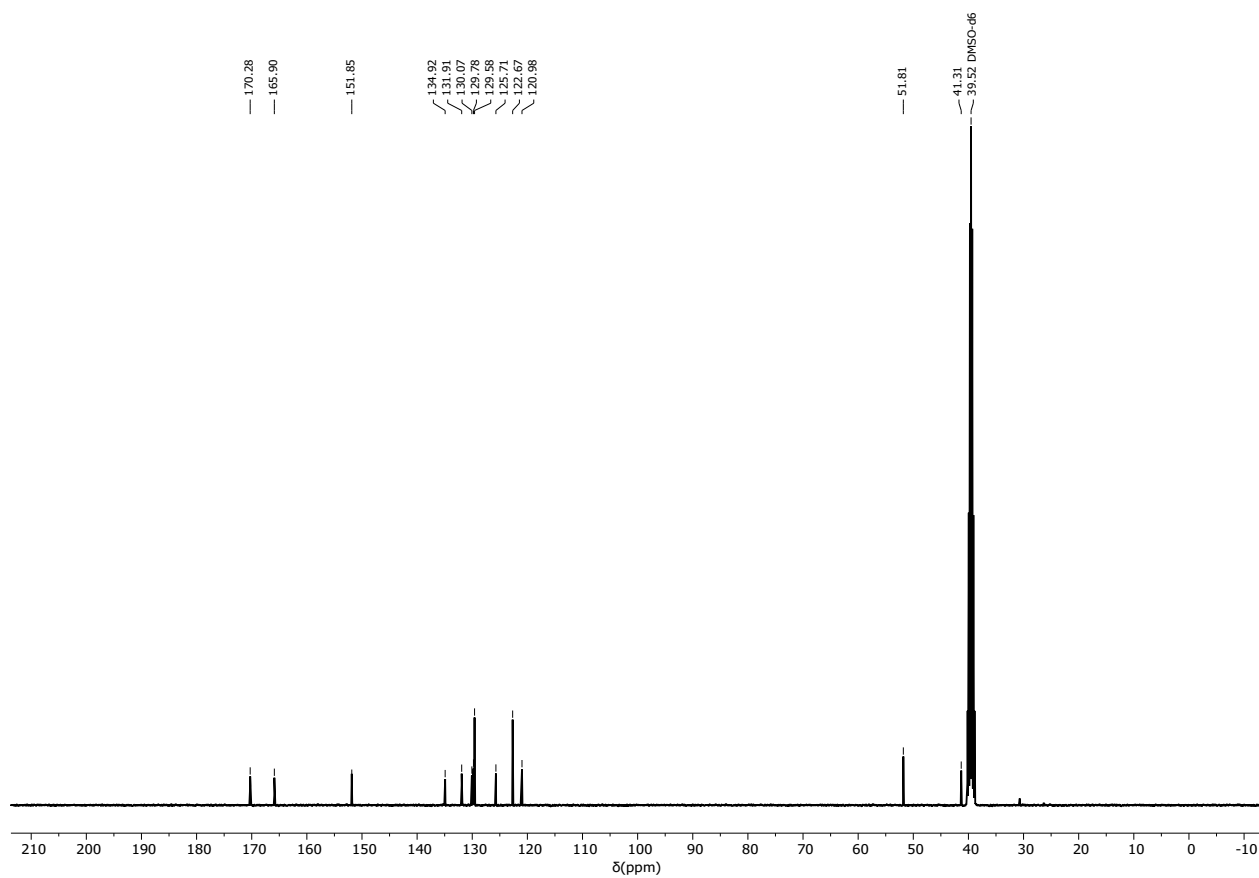


Figure S54. ¹³C-NMR spectra of *N*-[3-(phenylazo)benzoyl]glycine methyl ester measured in DMSO-d₆.

***N*-[3-(phenylazo)benzoyl]glycine (*m*-Gly-Azo)**

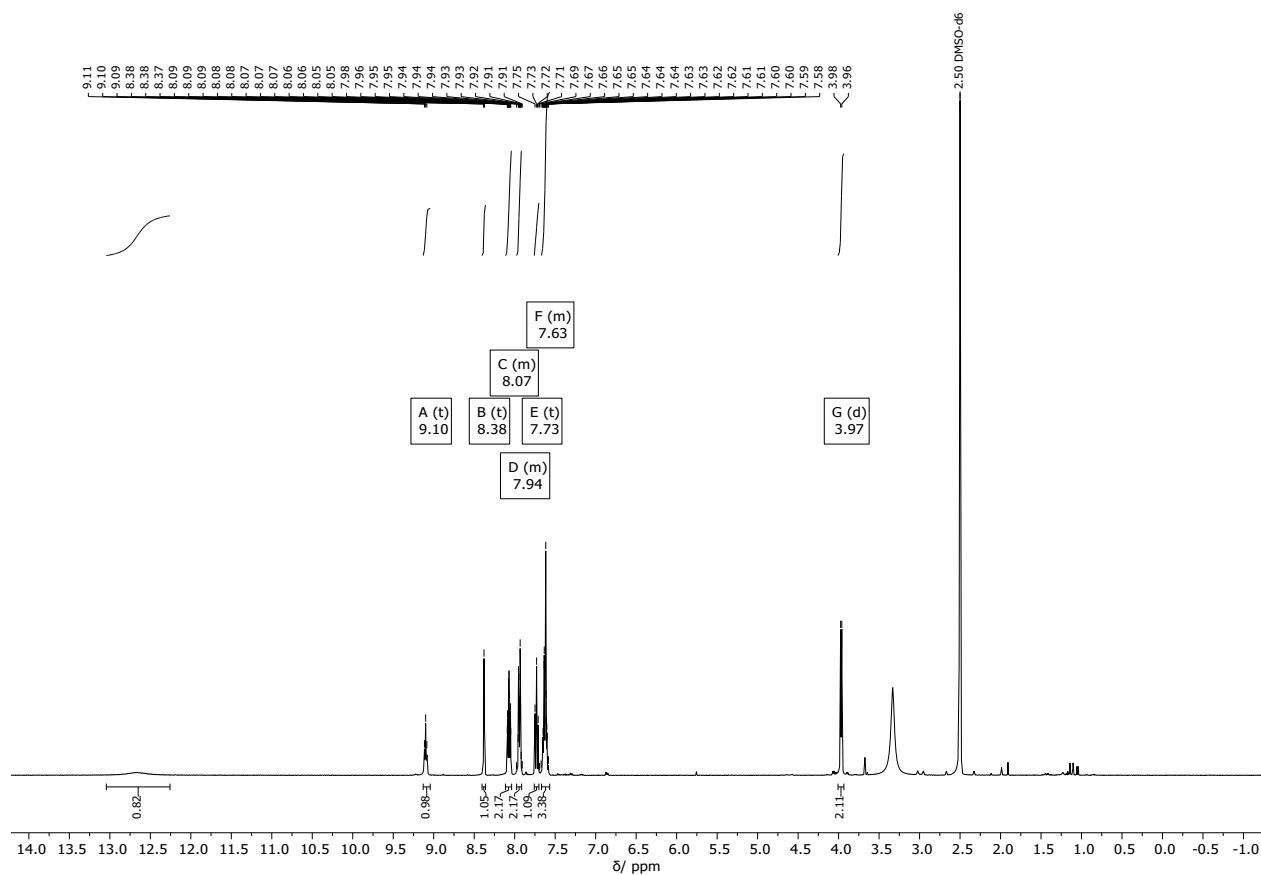


Figure S55. ¹H-NMR spectra of *N*-[3-(phenylazo)benzoyl]glycine (*m*-Gly-Azo) measured in DMSO-d₆.

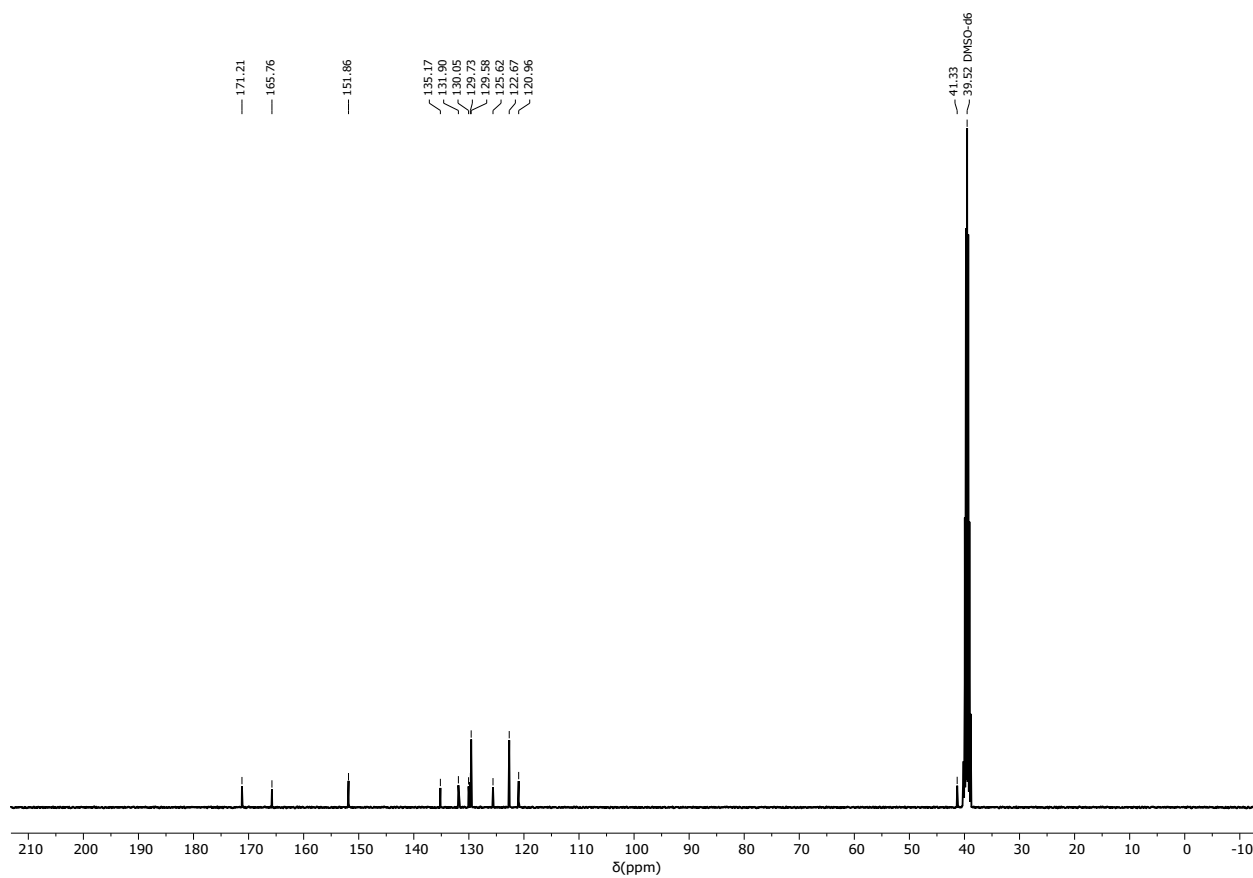


Figure S56. ^{13}C -NMR spectra of *N*-[3-(phenylazo)benzoyl]glycine (*m*-Gly-Azo) measured in DMSO- d_6 .

CND-*m*-Azo

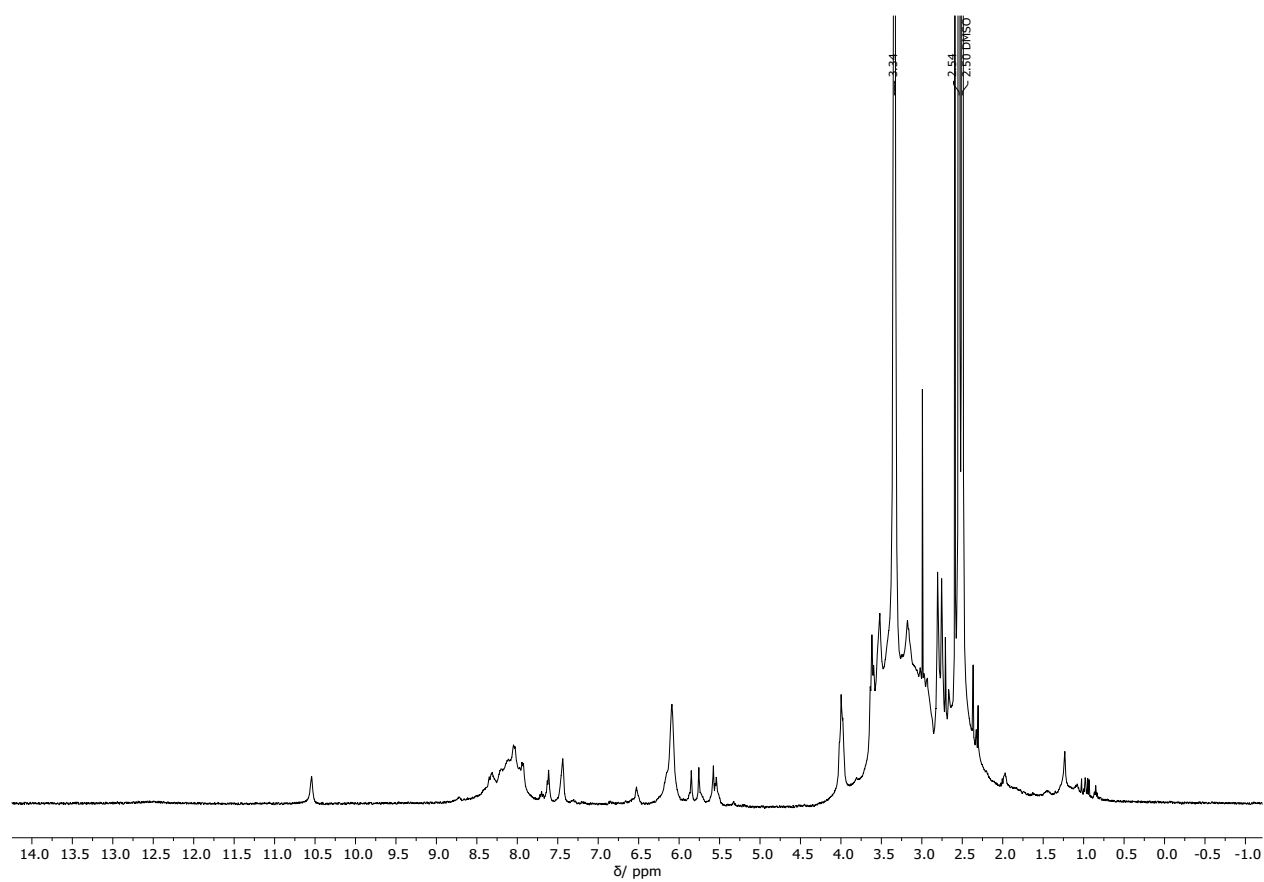


Figure S57. ^1H -NMR spectra of **CND-*m*-Azo** hybrid measured in DMSO- d_6 .

CND-*p*-Azo

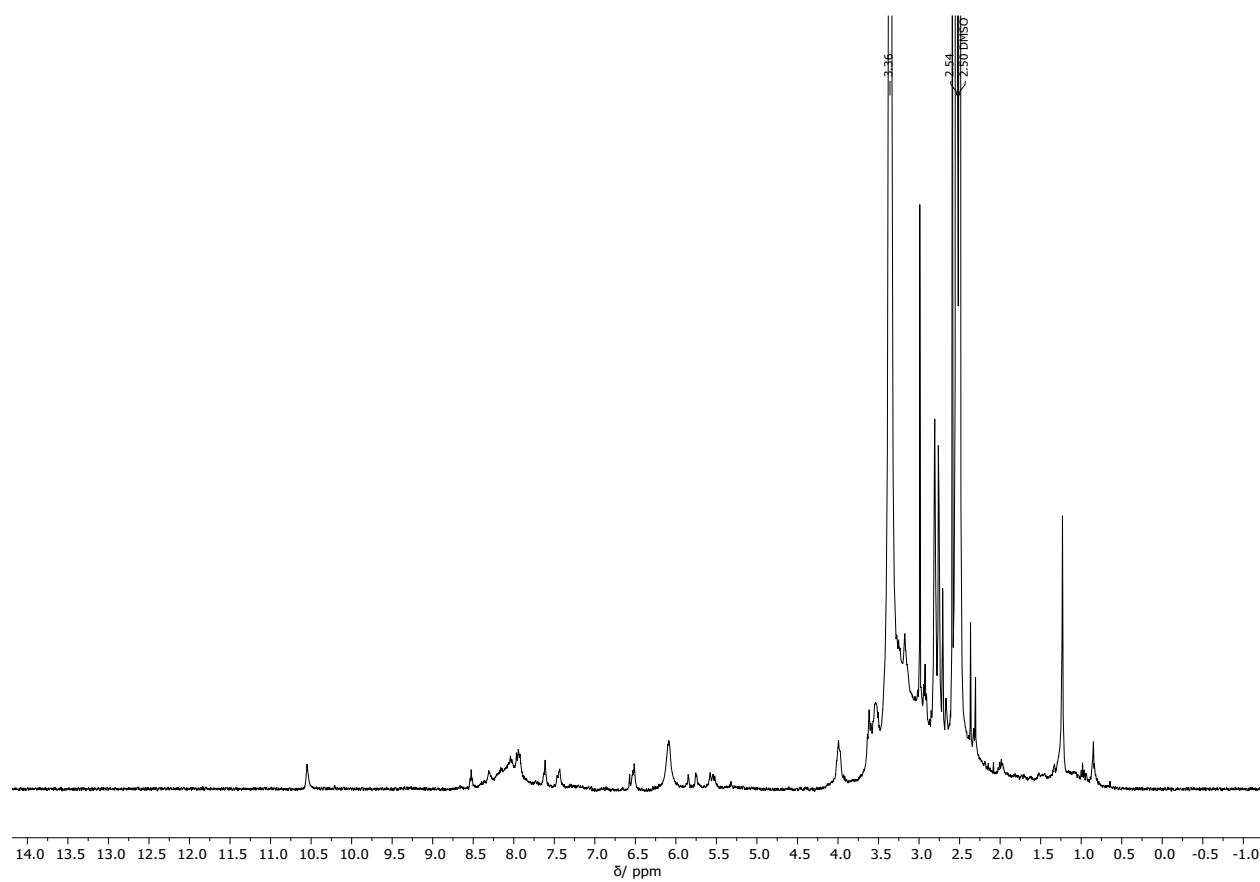


Figure S58. ¹H-NMR spectra of **CND-*p*-Azo** hybrid measured in DMSO-d₆.

CND-*m*-Gly-Azo

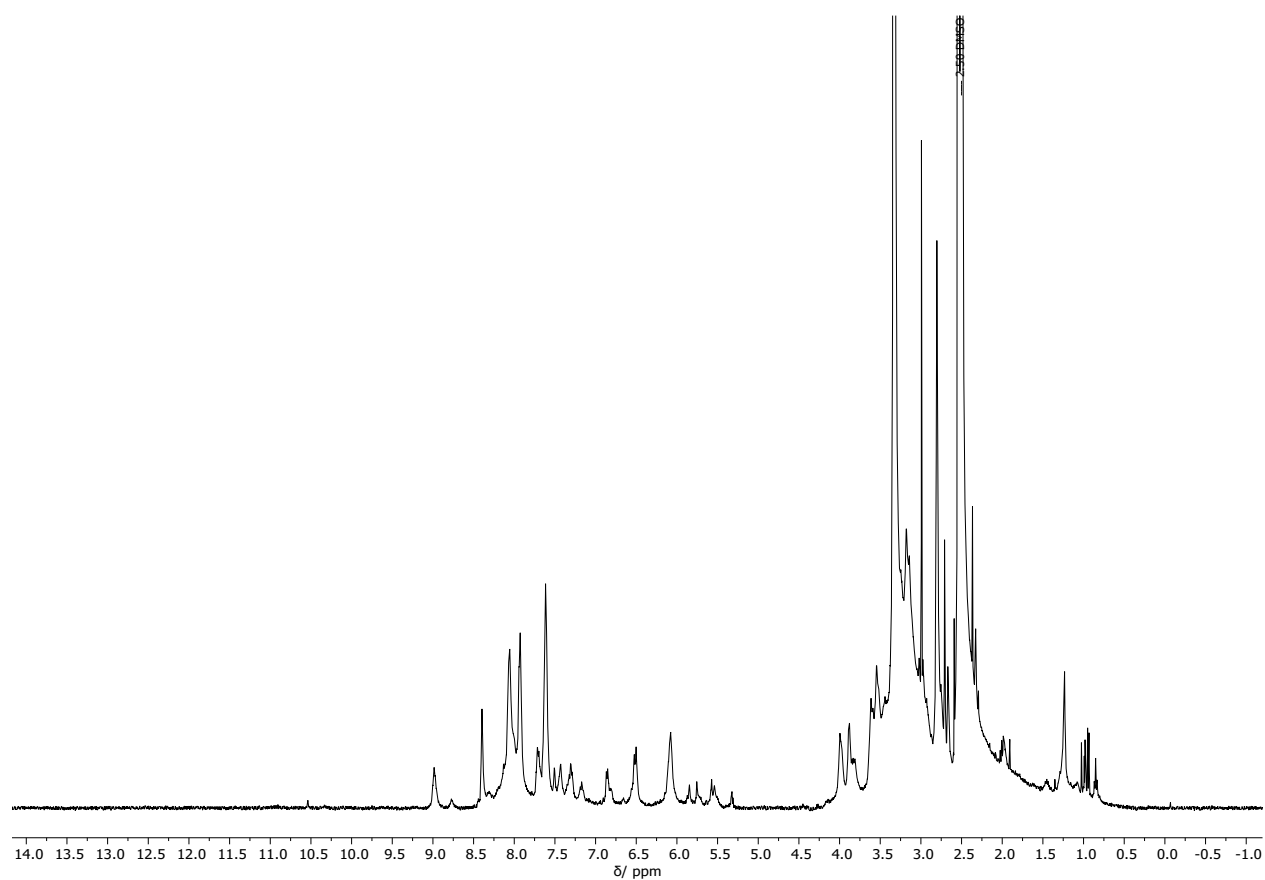


Figure S59. ¹H-NMR spectra of CND-*m*-Gly-Azo hybrid measured in DMSO-d₆.

References

- 1 S. N. Pham, J. E. Kuether, M. J. Gallagher, R. T. Hernandez, D. N. Williams, B. Zhi, A. C. Mensch, R. J. Hamers, Z. Rosenzweig, H. Fairbrother, M. O. P. Krause, Z. V. Feng and C. L. Haynes, *J. Chem. Educ.*, 2017, **94**, 1143–1149.
- 2 B. Bartolomei, A. Bogo, F. Amato, G. Ragazzon and M. Prato, *Angew. Chem. Int. Ed.*, 2022, **61**, e202200038.
- 3 P. Fatás, E. Longo, F. Rastrelli, M. Crisma, C. Toniolo, A. I. Jiménez, C. Cativiela and A. Moretto, *Chem. – Eur. J.*, 2011, **17**, 12606–12611.
- 4 J. Wang, P. Cieplak and P. A. Kollman, *J. Comput. Chem.*, 2000, **21**, 1049–1074.
- 5 J. Wang, W. Wang, P. A. Kollman and D. A. Case, *J. Mol. Graph. Model.*, 2006, **25**, 247–260.
- 6 D. A. Case, H. M. Aktulga, K. Belfon, I. Y. Ben-Shalom, J. T. Berryman, S. R. Brozell, D. S. Cerutti, T. E. Cheatham, G. A. Cisneros, V. W. D. Cruzeiro, T. A. Darden, N. Forouzesh, G. Giambasu, T. Giese, M. K. Gilson, H. Gohlke, A. W. Goetz, J. Harris, S. Izadi, S. A. Izmailov, K. Kasavajhala, M. C. Kaymak, E. King, A. Kovalenko, T. Kurtzman, T. S. Lee, P. Li, C. Lin, J. Liu, T. Luchko, R. Luo, M. Machado, V. Man, M. Manathunga, K. M. Merz, Y. Miao, O. Mikhailovskii, G. Monard, H. Nguyen, K. A. O'Hearn, A. Onufriev, F. Pan, S. Pantano, R. Qi, A. Rahnamoun, D. R. Roe, A. Roitberg, C. Sagui, S. Schott-Verdugo, A. Shajan, J. Shen, C. L. Simmerling, N. R. Skrynnikov, J. Smith, J. Swails, R. C. Walker, J. Wang, J. Wang, H. Wei, X. Wu, Y. Wu, Y. Xiong, Y. Xue, D. M. York, S. Zhao, Q. Zhu and P. A. Kollman, AMBER 12 University of California, San Francisco 2012.
- 7 W. L. Jorgensen, J. Chandrasekhar, J. D. Madura, R. W. Impey and M. L. Klein, *J. Chem. Phys.*, 1983, **79**, 926–935.
- 8 G. Bussi, D. Donadio and M. Parrinello, *J. Chem. Phys.*, 2007, **126**, 14101.
- 9 H. J. C. Berendsen, J. P. M. Postma, W. F. van Gunsteren, A. DiNola and J. R. Haak, *J. Chem. Phys.*, 1984, **81**, 3684–3690.
- 10 B. Hess, H. Bekker, H. J. C. Berendsen and J. G. E. M. Fraaije, *J. Comput. Chem.*, 1997, **18**, 1463–1472.
- 11 M. Parrinello and A. Rahman, *J. Appl. Phys.*, 1981, **52**, 7182–7190.
- 12 T. Darden, D. York and L. Pedersen, *J. Chem. Phys.*, 1993, **98**, 10089–10092.
- 13 D. Van Der Spoel, E. Lindahl, B. Hess, G. Groenhof, A. E. Mark and H. J. C. Berendsen, *J. Comput. Chem.*, 2005, **26**, 1701–1718.
- 14 C. Bannwarth, S. Ehlert and S. Grimme, *J. Chem. Theory Comput.*, 2019, **15**, 1652–1671.
- 15 C. Bannwarth, E. Caldeweyher, S. Ehlert, A. Hansen, P. Pracht, J. Seibert, S. Spicher and S. Grimme, *WIREs Comput. Mol. Sci.*, 2021, **11**, e1493.
- 16 S. Dapprich, I. Komáromi, K. S. Byun, K. Morokuma and M. J. Frisch, *J. Mol. Struct. THEOCHEM*, 1999, **461–462**, 1–21.
- 17 F. Maseras and K. Morokuma, *J. Comput. Chem.*, 1995, **16**, 1170–1179.
- 18 Q. Wu and W. Yang, *J. Chem. Phys.*, 2002, **116**, 515–524.
- 19 A. D. Becke, *J. Chem. Phys.*, 1997, **107**, 8554–8560.
- 20 S. Grimme, *J. Comput. Chem.*, 2006, **27**, 1787–1799.
- 21 J. D. Chai and M. Head-Gordon, *Phys. Chem. Chem. Phys.*, 2008, **10**, 6615–6620.
- 22 V. A. Rassolov, J. A. Pople, M. A. Ratner and T. L. Windus, *J. Chem. Phys.*, 1998, **109**, 1223–1229.
- 23 M. Cossi, V. Barone, B. Mennucci and J. Tomasi, *Chem. Phys. Lett.*, 1998, **286**, 253–260.
- 24 J. Tomasi and M. Persico, *Chem. Rev.*, 1994, **94**, 2027–2094.

- 25 J. Tomasi, B. Mennucci and R. Cammi, *Chem. Rev.*, 2005, **105**, 2999–3094.
- 26 J. J. P. Stewart, *J. Mol. Model.*, 2007, **13**, 1173–1213.
- 27 T. Vreven, B. Mennucci, C. O. da Silva, K. Morokuma and J. Tomasi, *J. Chem. Phys.*, 2001, **115**, 62–72.
- 28 S. J. Mo, T. Vreven, B. Mennucci, K. Morokuma and J. Tomasi, *Theor. Chem. Acc.*, 2004, **111**, 154–161.
- 29 M. J. Frisch, G. W. Trucks, H. B. Schlegel, G. E. Scuseria, M. A. Robb, J. R. Cheeseman, G. Scalmani, V. Barone, G. A. Petersson, H. Nakatsuji, X. Li, M. Caricato, A. V. Marenich, J. Bloino, B. G. Janesko, R. Gomperts, B. Mennucci, H. P. Hratchian, J. V. Ortiz, A. F. Izmaylov, J. L. Sonnenberg, D. Williams-Young, F. Ding, F. Lipparini, F. Egidi, J. Goings, B. Peng, A. Petrone, T. Henderson, D. Ranasinghe, V. G. Zakrzewski, J. Gao, N. Rega, G. Zheng, W. Liang, M. Hada, M. Ehara, K. Toyota, R. Fukuda, J. Hasegawa, M. Ishida, T. Nakajima, Y. Honda, O. Kitao, H. Nakai, T. Vreven, K. Throssell, J. A. Montgomery Jr., J. E. Peralta, F. Ogliaro, M. J. Bearpark, J. J. Heyd, E. N. Brothers, K. N. Kudin, V. N. Staroverov, T. A. Keith, R. Kobayashi, J. Normand, K. Raghavachari, A. P. Rendell, J. C. Burant, S. S. Iyengar, J. Tomasi, M. Cossi, J. M. Millam, M. Klene, C. Adamo, R. Cammi, J. W. Ochterski, R. L. Martin, K. Morokuma, O. Farkas, J. B. Foresman and D. J. Fox, 2016.
- 30 D. Nečas and P. Klapetek, Gwyddion: an open-source software for SPM data analysis Versita, co-published with Springer-Verlag GmbH 2012.
- 31 S. Sarkar, S. Dinda, P. Choudhury and P. K. Das, *Soft Matter*, 2019, **15**, 2863–2875.
- 32 W. S. Price, *NMR Studies of Translational Motion: Principles and Applications*, Cambridge University Press, Cambridge, 2009.
- 33 A. Lenoč, M. Schumacher, A. H. Gröschel, C. Cramer and M. Schönhoff, *Macromol. Chem. Phys.*, 2023, **224**, 2300286.
- 34 A. Sacco and E. Matteoli, *J. Solut. Chem.*, 1997, **26**, 527–535.
- 35 T. L. Nguyen and M. A. Saleh, *Results Chem.*, 2020, **2**, 100085.
- 36 M. Levitus, *Methods Appl. Fluoresc.*, 2020, **8**, 033001.
- 37 R. Luther and A. Nikolopoulos, *Z. Für Phys. Chem.*, 1913, **82U**, 361–384.
- 38 M. Palonciová, M. Šrejber, P. Čechová, P. Kührová, F. Zaoral and M. Otyepka, *J. Phys. Chem. B*, 2023, **127**, 1158–1166.
- 39 P. Nagy, FRET, <https://peternagyweb.hu/FRET.html>, (accessed March 10, 2025).
- 40 Á. Szabó, J. Szöllösi and P. Nagy, *Curr. Protoc.*, 2022, **2**, e625.
- 41 L. Schweighauser, M. A. Strauss, S. Bellotto and H. A. Wegner, *Angew. Chem. Int. Ed.*, 2015, **54**, 13436–13439.